Facoltà di Scienze Matematiche, Fisiche e Naturali
Dottorato di Ricerca in Scienze Chimiche
XXXI Ciclo

Design of Li-O_2 cells and study of the electrodes reactivity by means of a multi-technique approach

Anno Accademico 2017/2018

Candidato: Daniela Giacco

Relatore: Dott. Andrea Giacomo Marrani

Coordinatore: Prof. Osvaldo Lanzalunga

Index

CHAPTER 1

Introduction

1.1. Li-air cells - an emerging technology

Lithium-air cells are a promising system for energy storage thanks to their high theoretical energy density (i.e. about 3500 Wh kg^{-1}).[1–3] If some operating issues were overcome, they would be applied in various sectors where other common batteries show at the present time limited performance. Particularly, lithium-air is one of the most promising technology to replace the lithium-ion one, whose energy storage is limited (i.e. 2000 Wh kg^{-1}) by the thermodynamics of its characteristic reactions.[1,4]
Besides the electronic devices, lithium-air batteries could also find application in the electric transportation making possible the assembly and diffusion of full electric vehicles with high round trip efficiency and long time interval between a recharge and the next one.

The structure of a lithium-air cell usually includes a lithium anode, a porous cathode and a liquid, semi-solid or solid state electrolyte solution. On discharge, oxygen gas from the air is the active material, whose reduction leads to products that are different on the basis of the cell structure and used components.
A careful choice of the materials enables to realize an eco-friendly technology with lower costs respect to other storage devices.
At present, despite the theoretical good electrochemical response, lithium-air cells are quite far from being really operative because they cannot work in an "open" configuration due to some unwanted reactions at the electrodes/electrolyte interface mediated by the air gases different from oxygen such as carbon dioxide, nitrogen and moisture. Cell components degradation and the accumulation of by-products on the electrodes surfaces caused a fast loss of reversibility and the cell death after few cycles of discharge and charge.[1,2,5–8]
Therefore, two lines of research actually exist concerning the lithium-air technology.
On one hand, scientific efforts are aimed at making possible the exposition of the battery to air. This field of research is "engineering-related" and focus on the construction of protective membranes with a selective permeability to oxygen for both the anode and the cathode.[2,5,9]
On the other hand, the optimization of the "inner" electrochemistry and chemistry is mandatory to overcome the limits in the reversibility, the high overpotentials on discharge and charge, the energy loss and the low

long-term life. This research is realized on model devices in a closed configuration, filled with pure oxygen, called Li-O_2 cells. The goal is the evaluation of a good combination of electrode materials and electrolyte solutions demonstrating a limited degradation upon cycling. In a Li-O_2 cell, protected from the action of gas different from oxygen, the accumulation of insulating by-products derives from the chemical decomposition of the used electrode materials and electrolyte and has to be considered the major factor for the rise of the overpotentials and the cell death after few cycles.

1.2. Aprotic Li-O_2 cell – structure and reactions

The **anode** of a Li-O_2 battery is usually made of metallic lithium. Despite various operational issues related to its use, its unmatched lightness ensures high discharge capacity and energy density. Although an increase in the total weight of the anodic compartment must be taken into account, to protect lithium and prevent dendrites growth on its surface, various strategies have been proposed.[4,10,11]

Referring to the **electrolyte** solution, Li-O_2 cells can be identified as aqueous, non-aqueous or aprotic, mixed and solid-state. The solvent (i.e. water, organic, a mixture of them or a polymer-based material) influences the cell reactions and causes different working issues. Aqueous devices performance is limited by the incompatibility between the lithium anode and the aqueous medium. Mixed and solid-state batteries have a complicated and heavy structure. So, in the last years the research has focused almost totally on the non-aqueous Li-O_2 cells, whose aprotic electrolyte solution is composed by a lithium salt dissolved in an organic solvent.

The **discharge electrochemistry** of an aprotic Li-O_2 battery involves the oxygen reduction and combination with Li^+ cations to form lithium oxides (Oxygen Reduction Reaction - ORR). Lithium peroxide (Li_2O_2) is the major discharge product. Instead, lithium oxide (Li_2O) is quite undesired because its formation is only partially reversible. By means of various experimental and theoretical studies the reactions mechanisms have been investigated.[12–14] It is generally accepted that the ORR involves the following processes:

$$Li^+ + O_2 + e^- \rightarrow LiO_2 \quad (1)$$
$$LiO_2 + 3Li^+ + O_2 + 3e^- \rightarrow 2Li_2O_2 \quad (2)$$
$$2LiO_2 \rightarrow Li_2O_2 + O_2 \quad (3)$$
$$2Li^+ + O_2 + 2e^- \rightarrow Li_2O_2 \quad (4)$$

After a first oxygen monoelectronic reduction (1), a lithium superoxide (LiO_2) intermediate converts in Li_2O_2 by means of a second fast monoelectronic reduction (2) or a slow chemical disproportionation (3). However, a direct oxygen two-electrons reduction is also possible (4). Li_2O growth is more difficult because of the hardness of the O-O bond breaking in the O_2 molecule. This process becomes thermodynamically favored

only at high overvoltage, so it could be limited stopping the discharge process limiting the discharge capacity and/or the working potential to certain values.

Lithium oxides are insoluble in the organic electrolyte, so they accumulate on the cathode. The cell open circuit voltage (OCV) is similar to the Li_2O_2 formation theoretical E° (i.e. about 3.10 V, see the dashed blue line in Figure 1, U_o is the cell OCV)[1]. On discharge the voltage usually shows a sudden decrease becoming lower respect to the E° due to the partial or total lithium oxides insulating character. The unavoidable rise of the discharge overvoltage implies that the cathodic part of a typical Li-O_2 cell galvanostatic curve has the shape shown in Figure 1 (see the dashed black line, U_{dis} is the ORR operative potential).[1]

Theoretically, on **charge** the reverse reactions of (1), (2) and (4) take place (Oxygen Evolution Reaction - OER). However, it has been demonstrated that the reverse process of (1) and (2) can be viewed as reactions at the upper and the inner parts of Li_2O_2 particles, being their external layers oxygen-enriched (i.e. with Li^+ vacancies) respect to their bulk.[14,15] On charge overpotential is also usually registered. So, the anodic part of the galvanostatic curve fast rises respect to the OCV, as shown in Figure 1 (U_{chg} is the charge operative potential).

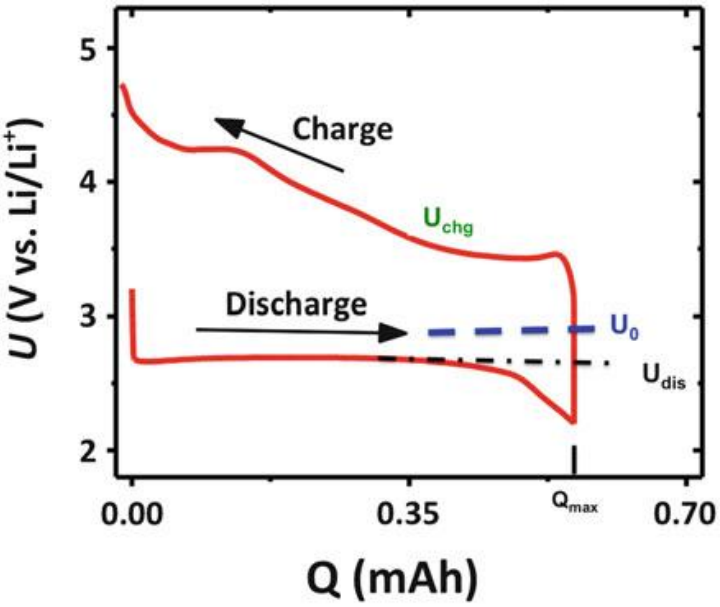

Figure 1. Typical shape of a Li-O_2 cell galvanostatic curve for one cycle of discharge and charge. In this case, the galvanostatic discharge–charge cycle was performed at a current density of 200 mA g^{-1}, adopting a solution of LiTFSI/DME as electrolyte and a Vulcan XC72 carbon black material as cathode (see Ref. [1]).

On summary, as portrayed in Figure 2,[16] in an aprotic Li-O_2 cell the ORR and OER take place at the cathode/electrolyte interface and are three-phase reactions because they involve Li^+ cations from the liquid electrolyte, the oxygen gas and the electrons flow moving through the cathode.

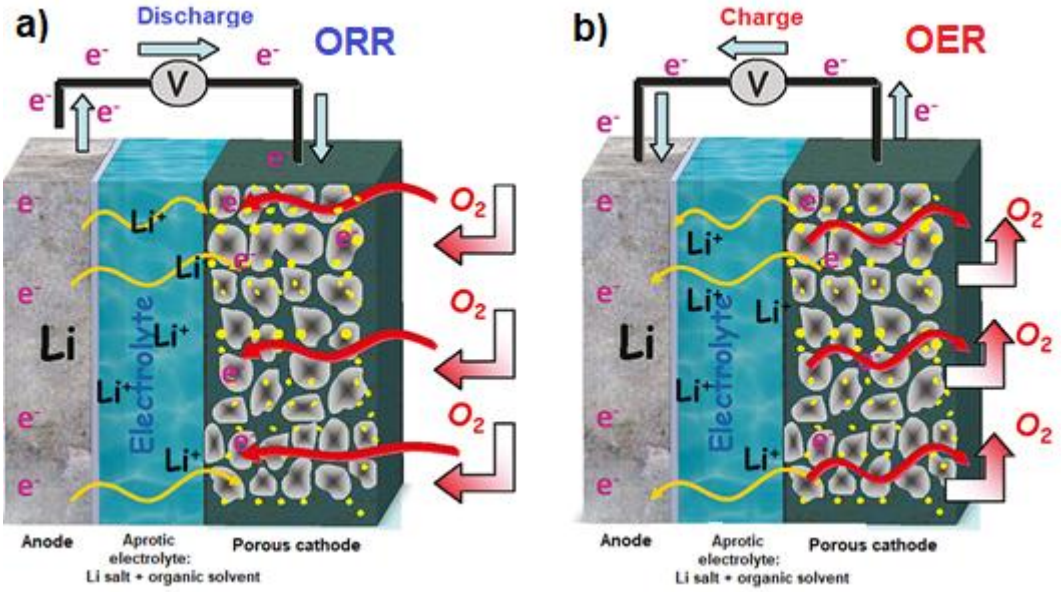

Figure 2. Schemes of the structure and a) the discharge (ORR) and b) the charge (OER) process in an aprotic Li-O_2 cell (see Ref. [16]).

Various research efforts have been devoted to test different combinations of inorganic lithium salts and organic solvents for Li-O_2 cells. Despite the overall effect has to be influenced by the interaction with other cell components, lithium triflate (LiTFO) or lithium bis(trifluoromethanesulfonyl)imide (LiTFSI) dissolved in a polyether such as tetraethyleneglycol dimethyl ether (TEGDME) have been reported to ensure good performance. This is due to the stability of the salt anion[17–19] and to an appreciable resistance to oxidative attacks of the solvent.[20]

The use of high donor number (DN) species to prepare the electrolyte, small discharge rates and cathode materials with low binding energy (BE) respect to LiO_2, facilitates the growth of lithium peroxide in large particles by means of a solution-based process (i.e. slow disproportionation (3) favored respect to fast second electron reduction (2)). Instead, low DN species, high rates and cathode materials with an high binding energy respect to the superoxide, cause the fast nucleation of Li_2O_2 layers by means of a surface-mediated mechanism (i.e. second electron reduction prevails upon disproportionation). In the first case, higher discharge capacity can be registered. Nevertheless, in the second case, the OER is favored thanks to an higher Li_2O_2 surface exposition.[3,20–28] So, the choice of both a lithium salt and a solvent with an intermediate DN (e.g. $TFSI^-$ and TEGDME) could be a good compromise in terms of degradation grade of the organic solvent, Li_2O_2 growth mechanism and related electrochemical response.

Due to its central role in the Li-O_2 electrochemical process, the **cathode** material has to respond to some desired characteristics. During the ORR, its conductivity enables the electron flow, its porosity allows the

accommodation of lithium oxides particles and the maintenance of an adequate oxygen flow and its lightness ensures the registration of high discharge capacity and energy density. Another possible key-factor should be its catalytic activity towards both the ORR and the OER. Low cost and environmental impact are also desirable. Finally, both the organic solvent and the positive electrode material have to resist to oxidative chemical attacks mediated by highly reactive reduced oxygen species (O_2^-, O_2^{2-}, $^1O_2$, LiO_2, Li_2O_2).[29–32]

1.3. A focus on cathode materials for aprotic Li-O_2 cells

In the most common configuration, an aprotic Li-O_2 cell was usually assembled with a **carbon-based** material as positive electrode. Various forms of carbon matched some of the desired characteristics (i.e. lightness, porosity, low cost and environmental impact). Moreover, carbon surface defects act as catalytic centers for both the ORR and the OER.[1,2,9,30,33,34,35] Unfortunately, carbon-based materials and polymer binders used as supports demonstrated low inertness to oxidative chemical attacks.[1,9,19,36–39] Upon cycling, their degradation by-products and those from the organic solvent accumulate on the cathode surface and its pores blocking the positive electrode. Moreover, their insulating character causes the rise of the overvoltage both on discharge and charge. Upon cycling, the increase of the voltage hysteresis stress the cell materials and shortens the battery life-time.
Therefore, the search of conductive, light, porous, low cost carbon-free material as cathode for Li-O_2 cell has become an emerging issue in the view of the assembly of an optimized configuration.[40] Moreover, this new material has to show equal or higher catalytic activity towards the cell reactions respect to carbon.

Good electrochemical performance have been reported for Li-O_2 cell assembled with **transition metal oxides** (TMOs) as positive inert carbon-free electrodes in combination with ether-based electrolytes. Due to their higher weight respect to the carbon-based ones, Li-O_2 cells assembled with TMOs such as WO_3,[40] TiO_2,[30,40] RuO_2, MnO_2,[30,41] Fe_2O_3, Fe_3O_4, NiO and CuO[42] in various crystallographic and morphological structures, have demonstrated lower specific discharge capacities. However, improved performance have been registered in terms of reversibility and extended cycle life because of the overpotential decrease, particularly on charge. In some cases, this effect has been related to the presence of defects on the material active surfaces such as oxygen vacancies, acting as catalytic sites for the OER.[30]
Among the TMOs, a particular case of study is the cobalt oxide Co_3O_4. This material, grown in various nano-structures, not only has remarkable effect in reducing the charge overpotential but also the potential gap between discharge and charge. Its catalytic activity towards both the ORR and the OER has been confirmed by the registration of enhanced discharge capacities and cycle stability.[30,40,43,44,45]
Some research groups related these phenomena to the high porosity and active surface of this nanostructured material and to a major exposition of catalytic sites to the electrolyte solution.[40,43,44,45] However, this explanation sounds somewhat inadequate as similar effects have not been registered using other TMOs. So, a possible influence of the Co_3O_4 electronic structure has to be supposed.

The toxicity and low eco-compatibility of Co(II), have made necessary its partial substitution with other cations.[42,46] This explains the enhancement of the scientific interest for **mixed transition metal oxides** such as **cobaltites,** with a general formula MCo_2O_4 where M represents a metal replacing some amount of cobalt. These materials have a spinel structure with a cubic unit cell cF56 with centered faces in which 56 atoms can be found: 16 cobalt atoms, 32 oxygen atoms and 8 M atoms different from cobalt (Figure 3).[47] Particularly, Co(II) occupies tetrahedral sites while Co(III) can be found both in tetrahedral and octahedral sites. Generally speaking, on the base of their valence, M^{n+} cations can substitute both Co(II) in tetrahedral sites and Co(III) in octahedral sites.[42,47]

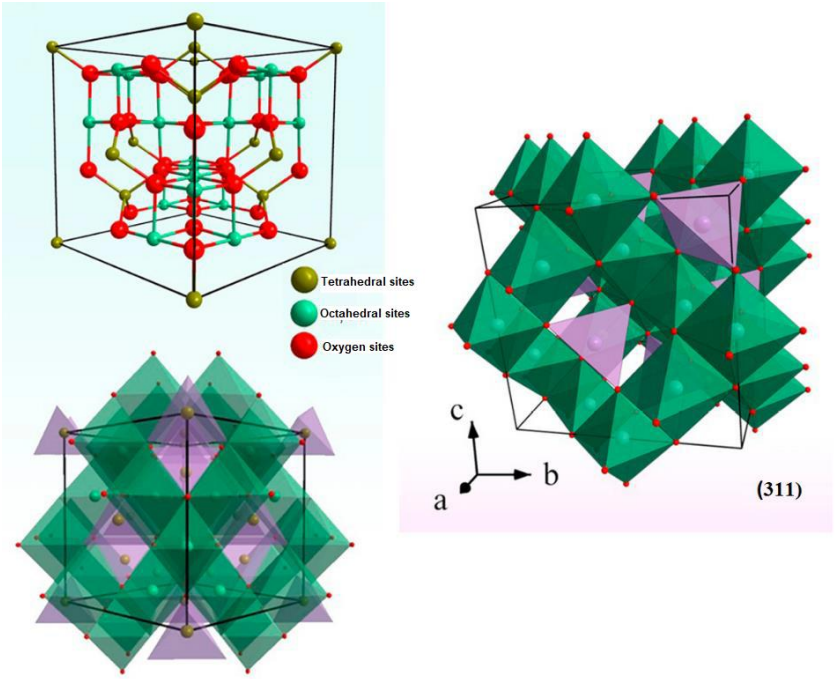

Figure 3. Spinel crystallographic structure (see Ref. [47]).

Among the cobaltites family, **nickel cobaltite ($NiCo_2O_4$)** has been reported as a good catalyst for the ORR and the OER, enabling remarkable electrochemical performance as cathode material for Li-O_2 cell.[48,49,50]
This compound is cheap, non-toxic and it can be synthesized by simple methods.[48,50,51,52] Moreover, $NiCo_2O_4$ demonstrates higher conductivity than the single oxides Co_3O_4 and NiO. So, on discharge and charge, it can facilitate the electron transfer.[46,53,54,55] However, as in the case of Co_3O_4, the nickel cobaltite electrochemical response cannot be explained in such a simple way. A general opinion is that its high catalytic activity has to be related to the co-presence of two redox couples in the crystallographic structure (i.e. Ni^{3+}/Ni^{2+} and Co^{3+}/Co^{2+}).[50] These sites, particularly at the surface of the cathode, possibly take part to multiple redox reactions.[51,53] However, their role and the modification of their relative abundance upon cycling (i.e. changes in the $NiCo_2O_4$ electronic structure) have not been clearly understood yet.
Another possibility, as reported for an iso-structured $CoMn_2O_4$, is to relate the catalytic effect to the presence of oxygen vacancy in the crystallographic lattice, acting as strong adsorption sites for O_2 and enabling the lowering of the kinetic barriers both for the ORR and the OER.[56]

In Figure 4 is shown the unit cell of the spinel $NiCo_2O_4$ crystallographic structure in which Ni atoms substitute Co^{3+} ions in octahedral sites. The synthesis procedure and its evolution could influence the substitution grade. Therefore, a more general formula for the nickel cobaltite is $Co^{2+}_{1-x}Co^{3+}_{x}[Co^{3+}Ni^{2+}_{x}Ni^{3+}_{1-x}]O_4$ with $0 < x > 1$.[53,57,58] Nevertheless, at the surface of the material, also a Ni substitution to Co^{2+} ions in tetrahedral sites has been proposed.[59]

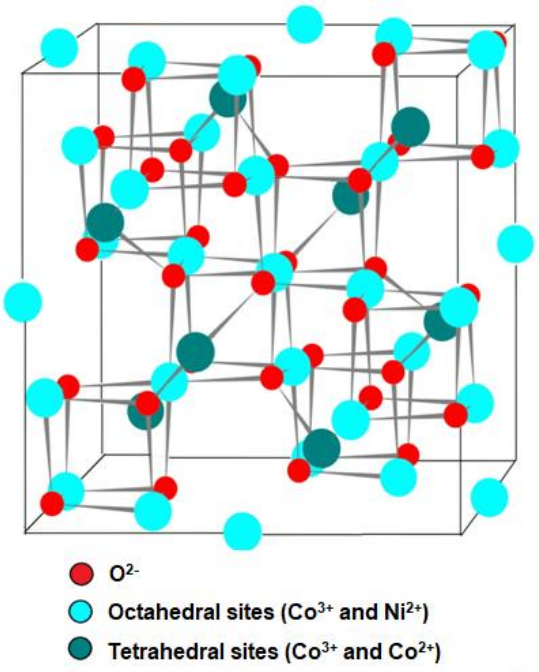

Figure 4. Unit cell of the spinel $NiCo_2O_4$ crystallographic structure.

The method of synthesis and its even minor modifications could influence the material nanomorphology. Thus, $NiCo_2O_4$ can be grown in the form of nanoparticles, nanoflakes, nanoflowers, nanowires, nanotubes, nanoroads, nanosheets etc.[60,61,62,63,64] The addition of a template agent in the synthesis solution has been reported to successfully enhance the porosity.[65,66]

Nanostructured $NiCo_2O_4$ cannot be used directly in electrochemical devices because is not a free-standing material. In some cases, it has been mixed with carbon and polymer binders and pressed onto a current collector.[61,62,65,66] In other experiments, its solution has been dropped on a carbon-based support.[63] For application in chemical oxidative environment, where the use of carbon-based material has to be avoided, another possibility is the deposition on an inert base that has to be introduced in the $NiCo_2O_4$ synthesis solution. In this last case, the nickel cobaltite usually grows in the form of nanowires whose diameter, length and porosity could be influenced by the support itself and other parameters such as the calcination temperature.[52,54,67] Moreover, a shape evolution from nanowires to nanoplates has been demonstrated if the amount of the precursors is modified increasing the Ni/Co ratio.[68]

As regards the application of nanostructured $NiCo_2O_4$ as active cathode material for Li-O_2 cells, some reports exist about the suitable use of a Ni foam support[50,69] with an "empty" structure, high surface area and macroporosity. Due to these features, Ni foam is able to ensure the deposition of large amount of cobaltite

and to maintain an abundant oxygen flow through the positive electrode. Thanks to its conductivity, it can act as current collector. Moreover, it demonstrates catalytic activity towards both the ORR and the OER.[70]

1.4. The possible use of a co-catalyst

A strategy to further enhance the electrochemical performance of a Li-O_2 cell is referring to a synergistic effect of a co-catalyst and the active material used as positive electrode. In the case of an heterogeneous catalysis, the co-catalyst has to be deposited on the cathode in a negligible amount, so also noble metals can be used.

Good results in terms of lowering the kinetic barriers of the ORR and/or the OER have been reported for Li-O_2 cell with a cathode constituted by a noble-metal in the form of nanoparticles or films (i.e. Pt/Au, Pt, Pd, Au, Ag) deposited on a carbon-based material.[71,72,73,74]

Unfortunately, these systems were still affected by the unavoidable carbon degradation. Recently, research efforts have been devoted to test these co-catalysts on inert materials such as noble (i.e. Au)[75] or transition metals (i.e. Ni)[36].

On the base of the portrait proposed in the previous paragraph, the obvious subsequent advancement is the tentative construction of a composed cathode made of noble metal nanoparticles onto a nanostructured mixed TMO grown on an open metal mesh. As an example, the synergistic co-catalytic effect between Pd nanoparticles and $NiCo_2O_4$ in the form of nanosheets has been demonstrated. However, in this case a reactive carbon foam has been used as support, possibly compromising the overall cell performance.[76]

CHAPTER 2

The PhD activity

2.1. Aims and surrounds of the PhD project

The scientific project of the PhD addressed in this work focused on chemical and electrochemical materials and processes involved in the operation of aprotic Li-O_2 cells. The activity has been devoted to the design of batteries working with different combinations of cathode materials and electrolyte solutions. Taking advantage of a multi-technique characterization approach, the main scope was to increase the knowledge on the reactivity at the triple O_2/cathode/electrolyte interface of the cells. Moreover, at the beginning of the second year of the PhD, the synthesis of new cathode materials showing enhanced electrochemical performance, made possible the assembly of Li-O_2 cells with competitive discharge capacity, reversibility and long-term life.

The supervision of the PhD activity has been performed by Dr. Andrea Giacomo Marrani at the Chemistry Department of La Sapienza, University of Rome. The work was based on an active collaboration with Dr. Sergio Brutti at the Sciences Department of the University of Basilicata.

Particularly, the materials synthesis was performed in the laboratories of both Universities. The cells assembly, the electrochemical tests and the materials characterization by means of Fourier Transform Infrared Spectroscopy (FTIR), Transmission Electron Microscopy (TEM) and X-ray Diffraction (XRD) were realized during periodical working visits at the University of Basilicata.

After the transfer to Rome, the samples were analyzed with X-ray Photoemission Spectroscopy (XPS) in the laboratory coordinated by Professor Robertino Zanoni. Some interesting electrodes were observed with the Scanning Electron Microscope with Field Emission source (FE-SEM) of the *Centro di Ricerca per le Nanotecnologie applicate all'Ingegneria della Sapienza* (CNIS).

At the beginning of the third year, a session of photoemission (XPS and UPS) spectroscopy measurements was performed at the Materials Science beamline of the Elettra synchrotron laboratory in Trieste.

2.2. An overview of the PhD activity through the three years

The **first year** of the PhD activity was devoted to the study of the degradation phenomena affecting a carbon-based cathode in model Li-O_2 cells. By means of electrochemical tests, spectroscopical and microscopical analysis, the interaction between a porous carbon cathode and the electrolyte based on lithium bis(trifluoromethane sulfonyl) imide in tetraethylene glycol dimethyl ether (LiTFSI/TEGDME) was investigated. The goal was to demonstrate the peculiar influence of the $TFSI^-$ anion on the degradation processes of both TEGDME and carbon. Upon cycling, the accumulation of chemical oxidative by-products derived from the solvent and the cathode was identified as the major factor of the long-term efficiency loss of the cell.

At the beginning of the **second year**, the activity was turned to the search of a carbon-free cathode material inert to chemical oxidation, porous and possibly demonstrating catalytic activity for the cell reactions. As explained in paragraph 1.3, Li-O_2 cells assembled with $NiCo_2O_4$ on Ni foam (NC@Ni) as cathode material have been reported to show good electrochemical performance. So, the work started synthesizing this material by means of a hydrothermal method and testing it in combination with the LiTFSI/TEGDME electrolyte. Then, in order to increase the catalytic activity of the NC@Ni system, doping with TM ions was devised and achieved through an opportune modification of the synthetic procedure. The obtained M^{n+}-doped $NiCo_2O_4$ on Ni foam is referred to as NCM@Ni.
Due to the significantly higher discharge capacity and reversibility and lower overpotentials recorded both on discharge and charge for the Cr^{3+}-doped and the Zn^{2+}-doped $NiCo_2O_4$ on Ni foam (NCCr@Ni and NCZn@Ni, respectively) compared to the pure NC@Ni, particular attention was devoted to the effect of these dopants on the electrochemical response of the doped electrodes. A full spectroscopical and morphological characterization was applied to the Ni-supported materials in parallel with the corresponding pure powders (NCCr and NCZn).
After the operation of the cells, selected cathodes were also analyzed ex-situ by means of XRD, XPS and SEM.

At the beginning of the **third year**, pristine NC@Ni, NCCr@Ni and NCZn@Ni electrodes, the corresponding powders and cathodes recuperated from cells that had worked in selected electrochemical conditions were measured at the Materials Science beamline of the Elettra synchrotron by means of XPS, in condition of enhanced resolution and sensibility.
The last months of activity were devoted to process the synchrotron data and formulate a complete portrait of the electrochemical and chemical properties of these materials.
Moreover, another step of the research was to investigate the possible co-catalytic activity of Pd nanoparticles (Pd NP) deposited onto the previously investigated NCCr@Ni material. The production of the Pd NP by pulsed laser ablation in liquid acetone (PLAL) in the fs regime, their deposition on the cobaltite

(which to the composed Pd/PdO@NCCr@Ni electrodes), the electrochemical tests and the XRD and TEM characterization of the materials were performed in collaboration with the research team of Dr. Angela De Bonis from the University of Basilicata, particularly with Dr. Antonio Gentile who based on this project his Master' degree thesis. Then, other investigations on pristine and post-mortem cathodes were performed by means of XPS and SEM in Rome.

CHAPTER 3

Instrumentation and techniques

3.1. Electrochemical characterization

All the electrochemical tests were performed on Li-O_2 cells in two possible closed configuration, filled with a fixed amount of pure O_2 (5.0 purity), setting the static final pressure in the dead volume above the positive electrode (about 3 cm^3) to 1.0 bar. Theoretically, due to the absence of a continuous flow of oxygen, the cell could work until its amount was totally consumed. However, the cell death always preceded this event. The first configuration was that of an MTI Corporation cell type EQ-STC-LI-AIR (Figure 5 a). On the cell base, a stainless steel current collector, a lithium anode, a Whatman glass-fiber separator impregnated with 250 µL of a 1 m LiTFSI/TEGDME electrolyte solution and the porous cathode were set one on top of the other. The cell was closed with a cap equipped with a manometer in order to control the pressure value. The second type of cell was an EC-CELL type ECC-Air (Figure 5 b) in which the components were put in reverse order. On a metallic grid the cathode, a separator impregnated with the electrolyte, a lithium anode and a current collector were stacked and the cell, closed with a cup, was then blocked in a support.

The cells were assembled in an argon-filled glove-box with a moisture concentration below 0.1 ppm, in order to protect the components from the air exposition before the electrochemical tests.

As regards the different types of measurements, both for the carbon-based cells and the cobaltite-based ones, galvanostatic cycling was carried out, connecting them to a MTI Corp. battery cycler. In a first set of electrochemical tests, voltage cut-offs were imposed in discharge and/or in charge in order to investigate the discharge capacity supply, the reversibility and the overvoltages affecting the ORR and the OER. The ex-situ chemical characterization of the cathodes recuperated from cells stopped at various stage of their discharge and charge allowed to monitor the growth/dissolution of the discharge products (i.e. lithium oxides) and/or of the chemical oxidative by-products. In a second set of experiments, capacity limits were imposed, while the number of cycles was set to 100. This electrochemical procedure preserves the degradation of the cell components upon cycling, enabling to test the long-term performance.

In the case of the study on the NC@Ni, NCCr@Ni and NCZn@Ni materials, pseudo-Tafel plots at different temperature were also derived from intermitted galvanostatic titrations experiments performed at various current densities. From the comparison of the results at T=22 °C, the catalytic effect of the dopants on the

decrease of the ORR and the OER kinetic barriers was confirmed. Moreover, for each material, processing the data at two different temperatures allowed the evaluation of the ORR and the OER activation energies.
For all the electrochemical tests, the imposed current densities and the measured capacities were normalized dividing by the geometrical area of the electrodes (1.54 cm^2).

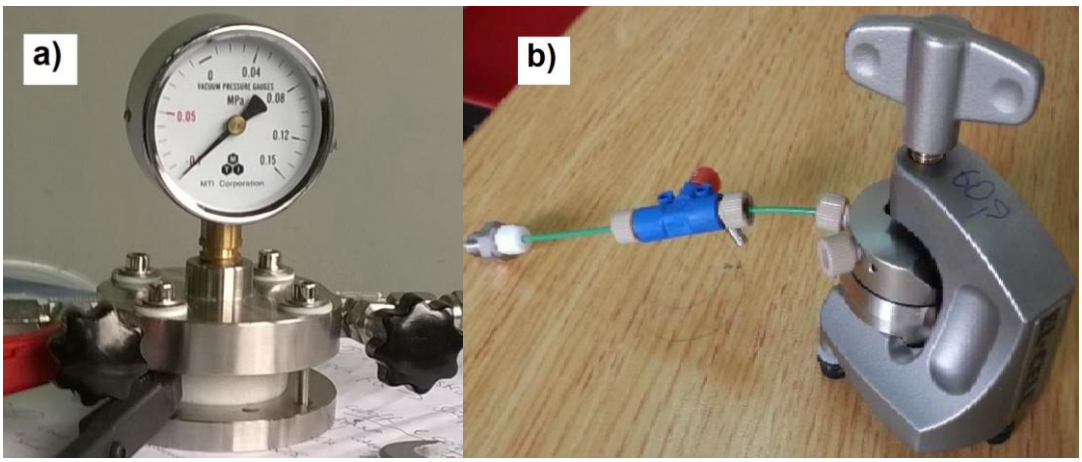

Figure 5. The a) MTI Corporation type EQ-STC-LI-AIR and the b) EC-CELL type ECC-Air Li-O_2 cell configurations adopted for the electrochemical tests addressed in this work.

3.2. Materials characterization

The materials characterization was performed with a powerful multi-technique approach. The aim was to explore the chemistry, the morphology and the crystal structure of the samples combining surface- and bulk-sensitive techniques.

3.2.1. SEM and EDS

The pristine materials and a selection of post-mortem cathodes were observed by means of the Zeiss Auriga Scanning Electron Microscope (FE-SEM) at the *Centro di Ricerca per le Nanotecnologie applicate all'Ingegneria della Sapienza* (CNIS). This instrument is equipped with a field emission source and a Bruker Energy Dispersive X-ray Spectroscopy (EDS) probe. No samples preparation was required.
Changes in the morphology of the post-mortem carbon-based cathodes respect to the pristine were evaluated. In the case of the pristine cobaltite-based materials, SEM allowed to explore possible differences in the nanomorphology between the undoped NC@Ni and the doped NCCr@Ni and NCZn@Ni and between the supported materials and the corresponding powders NC, NCCr and NCZn. Also in this second study, SEM analysis was performed on post-mortem cathodes to evaluate the effect of the electrochemical operations.
Finally, SEM images were recorded to complete the characterization of the Pd NP and the pristine Pd/PdO@NCCr@Ni electrode.

EDS analysis was particularly useful to confirm the homogeneous dispersion of chromium and zinc onto the $NiCo_2O_4$ nanofibers and their incorporation as dopants. Moreover, in the case of the Pd/PdO@NCCr@Ni sample, this instrumentation was used to assess the homogeneous coverage of the $NiCo_2O_4$ nanofibers by the Pd NP.

3.2.2. TEM

TEM observations were recorded using a FEI Tecnai 200 kV cryo-TEM instrument equipped with a LaB_6 electron beam source and two 2D flat cameras (low resolution and high resolution) at 200 kV e-beam acceleration. All the samples were suspended in THF in sealed vials by ultrasonic treatment (five cycles of 15 min of ultrasonic treatment followed by 45 min of rest to cool down the sample and thus avoid thermal heating), and dispersed on copper holey carbon film grids for observation.

In the case of the carbon-based electrodes, TEM images allowed to explore the morphological and structural changes of the carbon nanoparticles due to cell operations. Moreover, the reversible formation of lithium oxides and the overall accumulation of degradation products from carbon and solvent were observed.

As regards the cobaltites, the pristine materials were observed by TEM to assess the absence of structural and morphological modification of the $NiCo_2O_4$ nanofibers due to doping. In this case and for the Pd NP characterization, TEM pictures were analyzed using the ImageJ software.[77] Indexing the electron diffraction patterns derived by selected areas Fast-Fourier-Transform (FFT) of the figures, it was possible to confirm the chemical nature of the materials.

3.2.3. FTIR spectroscopy

FTIR spectra of the carbon-based cathodes were acquired by a Jasco FTIR-460 Plus apparatus in the wave number range between 2000 and 400 cm^{-1} at room temperature in transmission mode. Materials removed from the cathodes and from a pristine carbon positive electrode, as fine powders, were mixed in an Ar-filled glovebox with CsI and then pressed in pellets by a Pike die set and handpress. FTIR spectra were also recorded for pure Li_2O_2, Li_2O, and Li_2CO_3 powders as benchmark materials.

Infrared spectroscopy was useful to detect the discharge products (i.e. lithium oxides) and the by-products of the solvent TEGDME and the carbon cathode accumulated both on its surface and in its pores. In the transmission mode, the infrared rays cross the samples entirely allowing to gain information on the chemical composition both of their surface and bulk.

For the characterization of the pristine cobaltite-based positive electrodes, this technique was not applied due to the relatively “empty” structure of the samples in which low amount of active material is deposited on the Ni foam “open” framework. Infrared spectroscopy measurements were attempted on the cobaltites powders, but the spectra revealed not useful due to the predominance of signals related to samples hydration.

3.2.4. XRD

XRD experiments were carried out on the NC@Ni, NCCr@Ni and NCZn@Ni pristine electrodes and on the corresponding powders NC, NCCr and NCZn using a Siemens D5000 diffractometer equipped with a CuKα source and a graphite monochromator for the diffracted beam. X-ray diffraction was used to unequivocally identify the chemical nature of the materials detecting the characteristic reflections of their crystalline structure. The presence of phases different from $NiCo_2O_4$ spinel was also investigated.

Some XRD measurements were tentatively performed on post-mortem cathodes with the aim to detect crystalline discharge products (i.e. lithium oxides). Unfortunately, the amorphous nature of these materials and/or the low dimension of their crystalline domains prevented to confirm their nucleation on discharge and decomposition on charge by means of this technique for almost all the samples. This was probably related to the effect of the electrolyte solution (i.e. LiTFSI/TEGDME) on the Li_2O_2 growth mechanism and resulting morphology (see Ch. 1, Par. 1.2). For the same reason, X-ray diffractograms were not recorded for carbon-based cathodes studied previously.

3.2.5. XPS

X-ray photoemission spectroscopy is one of the most powerful surface analysis techniques. It is sensitive to the first atomic layers of the samples and provides information about their elemental composition, the elements oxidation states and their chemical surroundings.

XPS measurements were performed on the NC@Ni, NCCr@Ni and NCZn@Ni pristine electrodes and on the corresponding powders NC, NCCr and NCZn to highlight the redox states of the transition metals and their relative abundance at the samples surface, eventually modified in the doped samples respect to the pure material. This information could help in the interpretation of the electrochemical performance of the undoped and doped cathodes. XPS analysis was also conducted on post-mortem cathodes to assess the reversible formation of lithium oxides and the factors related to the cell death.

In the study concerning the use of Pd NP as co-catalyst, XPS revealed particularly useful because it was the only technique able to shed light on the real nature of the Pd deposits.

For all the samples, XP spectra were recorded using a modified Omicron Nano-Technology MXPS system equipped with a monochromatic X-ray source (Omicron XM-1000) and an Omicron EA-127 energy analyzer (Figure 6 a).

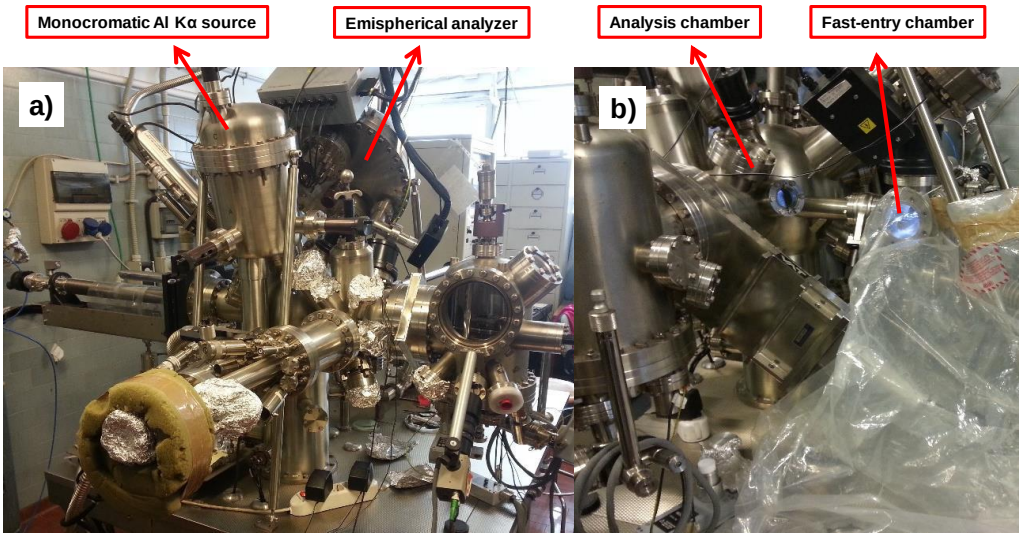

Figure 6. a) The spectrophotometer used for the XPS measurements addressed in this work; b) the XPS fast-entry lock chamber with connected an argon-filled glove-bag to avoid the contact of the samples with air before measurements.

The exciting radiation was Al Kα (hυ = 1486.7 eV), generated operating the anode at 14−15 kV and 10−20 mA. All of the photoionization regions were acquired using an analyzer pass energy of 20 eV, except for the survey scan, taken at 50 eV pass energy. Take-off angles of 11° with respect to the sample surface normal were adopted. The measurements were performed at room temperature, and the base pressure in the analyzer chamber was about 2×10^{-9} mbar. Samples extracted from the cells after the electrochemical tests were transferred into the spectrometer through an argon-filled glove-bag connected to the fast-entry lock chamber of the instrument to avoid contact with air (Figure 6 b). Sample degradation due to X-ray exposure was not evident within the duration time of each experimental observation. On the basis of appropriate criteria, for the different samples internal standard references were selected for the construction of a Binding Energy (BE) scale (accuracy of ±0.05 eV).

The experimental spectra were reconstructed by fitting the secondary electrons' background to a Shirley function and the elastic peaks to pseudo-Voigt functions described by a common set of parameters (position, fwhm and Gaussian−Lorentzian ratio) free to vary within narrow limits. During the fitting procedure the Gaussian−Lorentzian ratio was left free to vary between 0.6 and 0.9. XPS atomic ratios between relevant element components were estimated from experimentally determined area ratios (with ±10% associated error), which were corrected for the corresponding photoelectron cross sections according to Scofield calculations and for the square root dependence of the photoelectron kinetic energy. The softwares ESCA300 and XP Spectral Data Processor were used for the spectra reconstruction and the atomic relative quantification, respectively.

3.2.6. XPS measurements with synchrotron radiation

Unfortunately, use of the lab XPS instrument to study NC@Ni, NCCr@Ni and NCZn@Ni pristine electrodes proved nearly inefficient to perform the relative surface quantification of the metal components. In

fact, due to the low signal-to-noise (S/N) ratio only a tentative curve fitting reconstruction of the Ni 2p, Co 2p, Cr 2p and Zn 2p photoemission regions was attempted. Moreover, the determination of the atomic ratios (i.e. Ni/Co etc.) was compromised by the contribute to the signal intensity in the Ni 2p photoemission region of the underlying Ni mesh. So, a proposal was submitted to the Elettra synchrotron facility to acquired spectra in condition of higher energy resolution and sensibility.

XPS measurements were performed at the Materials Science beamline on pristine NC@Ni, NCCr@Ni and NCZn@Ni electrodes, on the corresponding NC, NCCr and NCZn powders and on post-mortem cathodes from Li-O_2 cells that had operated in various electrochemical conditions.

Materials Science is a beamline suitable for experiments in materials science, surface physics, catalysts and organic molecules on various surfaces. The tunability of the photon energy ranges from 22 to 1000 eV with mainly linearly polarized light from a bending magnet source and tunable excitation energy for the best photoionization cross sections. The spot size on the sample has a diameter of ~100 μm. Photoelectrons from the sample are analyzed by hemispherical electron energy analyzer. In Figure 7 a and 7 b a photograph of the spectrophotometer at Materials Science and a scheme of the beamline are shown, respectively.

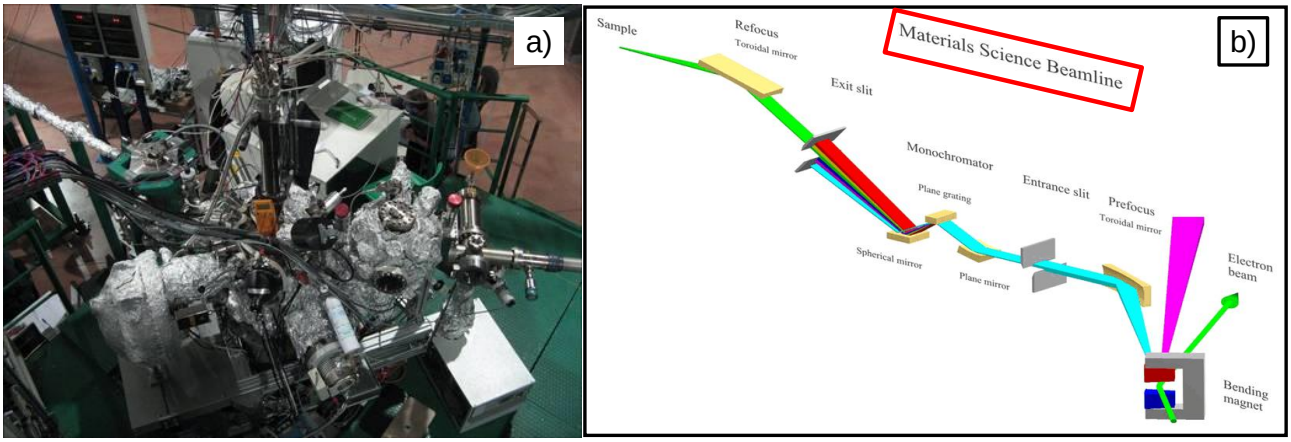

Figure 7. a) The spectrophotometer used at Materials Science; b) a scheme of the beamline.

The resolving power is naturally better at lower energies, allowing the photon flux to be further increased by opening both the entrance and exit slit wider than the typical values (100 μm for entrance and 200 μm for exit slit). In this case the resolving power is still higher than 1000 and photon energy resolution below 100 meV. In Figure 8 the experimental flux curve for a storage ring energy of 2.0 GeV normalized to 300 mA ring current is shown. The data are collected from a photodiode inserted at the end of the beamline with the entrance slit open to 100 μm and exit slit to 250 μm (typical setting). Below 50 eV the flux can be increased by factor of 10 by opening the slits without significant impact to energy resolution.

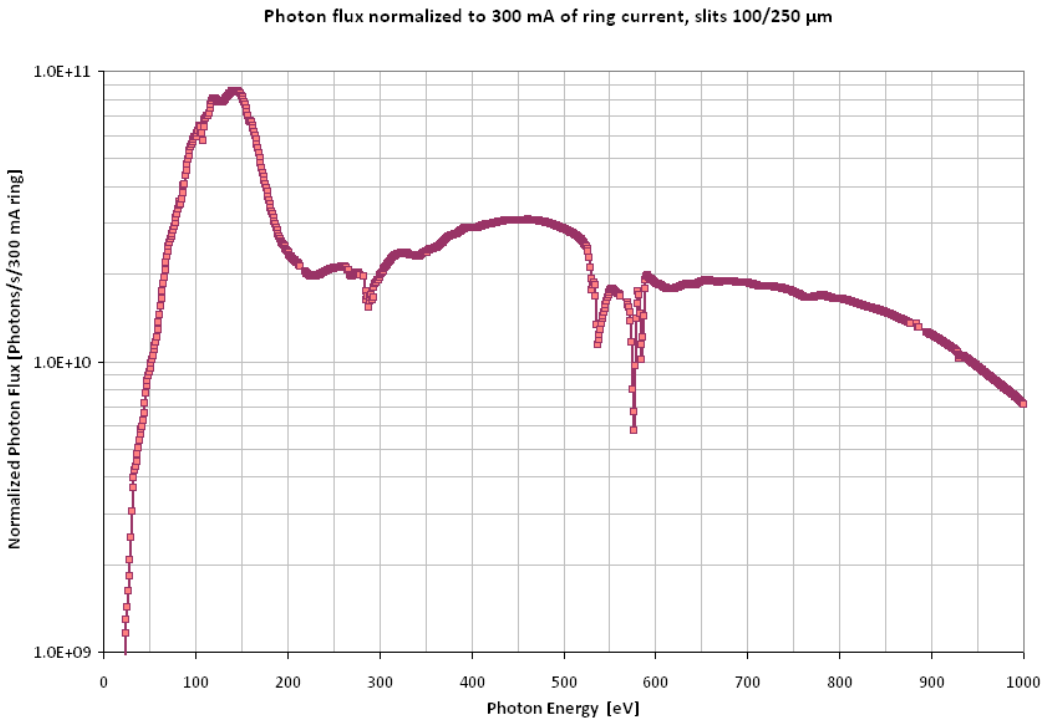

Figure 8. The experimental flux curve at Materials Science for a storage ring energy of 2.0 GeV normalized to 300 mA ring current.

During the measurements upon the cobaltite-based samples addressed in this work, the exciting radiation was varied choosing the best for all the acquired photoemission regions. The criteria adopted refers to the general rule that a photoemission cross section is greater if the used excitation energy is similar to the energy of the corresponding ionized orbital. The experiments were performed at room temperature and the base pressure in the analyzer chamber was about 2×10^{-9} mbar. Post-mortem cathodes were transferred to Elettra in sealed vials and inserted into the spectrometer through an argon-filled glove-bag connected to the fast-entry lock chamber of the instrument to avoid contact with air. Sample degradation due to X-ray exposure was not evident within the duration time of each experimental observation.

The data processing was performed by means of the software KolXPD. First of all, a calibration of the photon energy was applied referring to the Au 4f photoemission line as standard.

As regards the fitting procedure, the experimental spectra were reconstructed by fitting the secondary electrons' background to a Shirley function and the elastic peaks to Voigt functions described by a common set of parameters (position, amplitude, Gaussian and Lorentzian fwhm) free to vary within narrow limits. XPS atomic ratios between relevant element components were estimated from experimentally determined area ratios (with ±10% associated error), which were corrected for the corresponding photoelectron cross sections derived from literature, reported in the Elettra website and stored in the KolXPD memory.

CHAPTER 4

Study on a carbon-based cathode

4.1. Aims

The PhD activity started studying model Li-O_2 cells assembled with a porous carbon cathode in combination with LiTFSI/TEGDME as electrolyte solution.[19] The goal was to describe the reactivity at the triple interface O_2/cathode/electrolyte where the electrochemical and chemical reactions occur. On discharge, both the carbon-based cathodes and the ethereal solvents used in Li-O_2 cells are known to undergo degradation due to the chemical oxidative attacks mediated by the oxygen reduced species.[29–32] Gaining major insights in these processes competing with the Li_2O_2 reversible formation by means of the ORR/OER is fundamental for identifying mitigation strategies to improve cell efficiency upon cycling. Particularly, an evaluation of the peculiar interaction between the cathode material and the electrolyte could be useful. In fact, in this work great attention was given to the $TFSI^-$ anion influence on the chemical nature of the cathode degradation products.

4.2. Samples preparation and cells assembly

As described in chapter 3, paragraph 3.1, Li-O_2 cells and electrolyte solutions were prepared in an Iteco Engineering argon-filled glovebox with moisture concentration below 0.1 ppm. In the case of the study on carbon-based cathodes, the batteries were assembled by using a MTI Corporation cell type EQ-STC-LI-AIR MTI Corp. (Figure 5 a) consisting of a stainless steel current collector, a metallic lithium foil as anode, a glass-fiber separator (Whatman, 18 mm in diameter) impregnated with 250 μL of a 1 m electrolyte solution, and a commercial porous carbon foil (MTI Corp., 14 mm in diameter) as cathode. The positive electrode was constituted of a mixture of Super P carbon and a fluorinated polymeric binder (Kynar, Arkema) dispersed on an inert carbonaceous gas diffusion layer. The ratio between carbon Super P and the binder was 38:62 w/w. This average percentage was systematically obtained measuring the weight of carbon remaining after vigorously washing with tetrahydrofuran (THF) and treating in an ultrasound bath of some pristine electrodes to completely remove the binder. The exact composition of this fluorinated polymer is not known but it is probably a co-polymer of polyvinylidene fluoride (PVDF) and hexafluoropropene (HFP). The salt

and the porous cathodes were dried at 110 °C overnight under vacuum before use. The solvent was used after drying/storage on regenerated 3 Å molecular sieves (Sigma-Aldrich) and lithium chips for at least 15 days in a glovebox. Li−O_2 cells were filled with pure O_2 (5.0 purity spilled from a high-pressure cylinder through stainless steel gas lines, preliminarily evacuated, equipped with a molecular sieve-filled moisture trap), setting a static final pressure of 2.2 bar in the dead volume (about 3 cm^3) above the porous electrode.

In a first set of electrochemical tests, galvanostatic cycling of the cell was carried out, connecting to a MTI Corp. battery cycler, setting to a single cycle with a current density of 0.2 mA cm^{-2} and stopping at cut-off voltages of 2.6, 2.5, and 2.0 V in discharge and 4.0 and 4.6 V in charge. The measured capacity was normalized dividing by the geometrical area of Super P carbon electrode (1.54 cm^2). The reversibility was calculated as the ratio between the capacities measured on charge and on discharge. A second type of experiments were devoted to test the long-term performance, so galvanostatic cycling were carried out imposing capacity limits of 0.2 and 0.4 mA h cm^{-2} and current density values of 0.2 and 0.4 mA cm^{-2}, while the number of cycles was set to 100.

After the electrochemical measurements, the cells were disassembled in glovebox. Their cathodes were recuperated and washed in TEGDME and in THF to remove the excess electrolyte, and dried under vacuum at room temperature prior to the chemical characterization.

A pristine carbon foil and a carbon foil wet with electrolyte were considered as benchmarks samples.

4.3. Electrochemical tests

4.3.1. Voltage limited performance on one cycle

Electrochemical discharge and discharge/charge tests were carried out under galvanostatic control at a constant current rate of 0.2 mA cm^{-2} with fixed voltage cut-offs. An example of the measured cell voltage profile is shown in Figure 9 for a cell fully cycled between 2.0 and 4.6 V. The corresponding performance in terms of specific capacity and charge reversibility are summarized in Table 1.

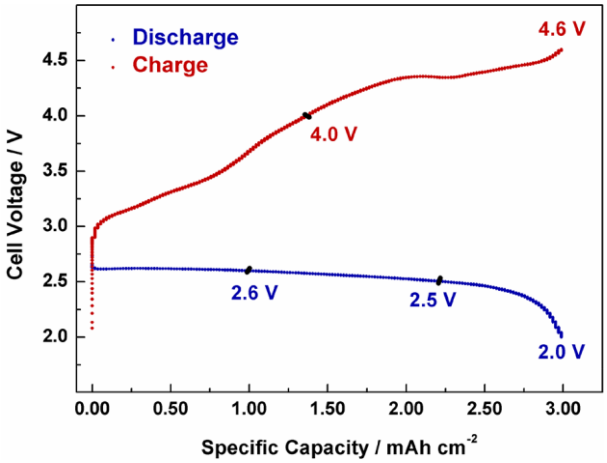

Figure 9. Galvanostatic cycle between 2.0 and 4.6 V of a carbon-cathode based cell. Cathodic and anodic cut-off voltages for partially discharged and charged cells are marked with black dots. Applied current density was 0.2 mA cm^{-2}.

The profile of the galvanostatic curve resembles that reported in literature for similar systems (see Figure 1).[1] On discharge (Figure 9, blue curve), we observe a stable plateau at about 2.6 V, below the thermodynamically estimated potential for the ORR (3.1 V), thus suggesting the occurrence of moderate overvoltages. This feature is due to the partial insulating character of both the main discharge product Li_2O_2 and the eventually formed chemical degradation by-products from the carbon electrode and the TEGDME solvent. As expected, upon discharge the specific capacity increases for deeper reductions (see Table 1).

On charge, a short plateau at about 3.3 V and a long plateau at about 4.4 V are visible. These charge plateaus are related to the OER from an oxygen-rich species (i.e. a layer "LiO_2 –like" covering the Li_2O_2 particles) and from the bulk of lithium peroxide particles, respectively.[14,15] Also on charge, due to the partial insulating character of both lithium peroxide and degradation by-products, overvoltages are registered. In fact, the two plateaus are above the thermodynamically estimated potential for the OER.[1] The total capacity increases at high anodic voltage cut-offs, reaching an overall charge reversibility of 1 for the cell fully cycled between 2.0 and 4.6 V (see Table 1) .

Sample	**Galvanostatic condition ($J = 0.2$ mA cm^{-2})**	**Discharge capacity (mAh cm^{-2})**	**Charge capacity (mAh cm^{-2})**	**Reversibility**
D. 2.6 V	discharge to 2.6 V	0.99 ± 0.15		
D. 2.5 V	discharge to 2.5 V	2.21 ± 0.33		
D. 2.0 V	discharge to 2.0 V	2.99 ± 0.45		
C. 4.0 V	discharge to 2.0 V and charge to 4.0 V	2.99 ± 0.45	1.37 ± 0.21	0.46 ± 0.07
C. 4.6 V	discharge to 2.0 V and charge to 4.6 V	2.99 ± 0.45	2.97 ± 0.44	0.99 ± 0.07

Table 1. Summary of the carbon-based cells studied on one galvanostatic discharge-charge cycle and corresponding performance. The reversibility has been calculated as the ratio between the charge and the corresponding discharge capacity.

4.3.2. Long-term performance

Long-term tests for the carbon-based cells were carried out performing their galvanostatic cycling at two different values of limited capacity and current densities, while the number of cycles was set to 100.

The resulting electrochemical performance are shown in Figure 10 in terms of specific capacity and charge reversibility versus cycle number. The samples and their corresponding cycle of death are summarized in Table 2.

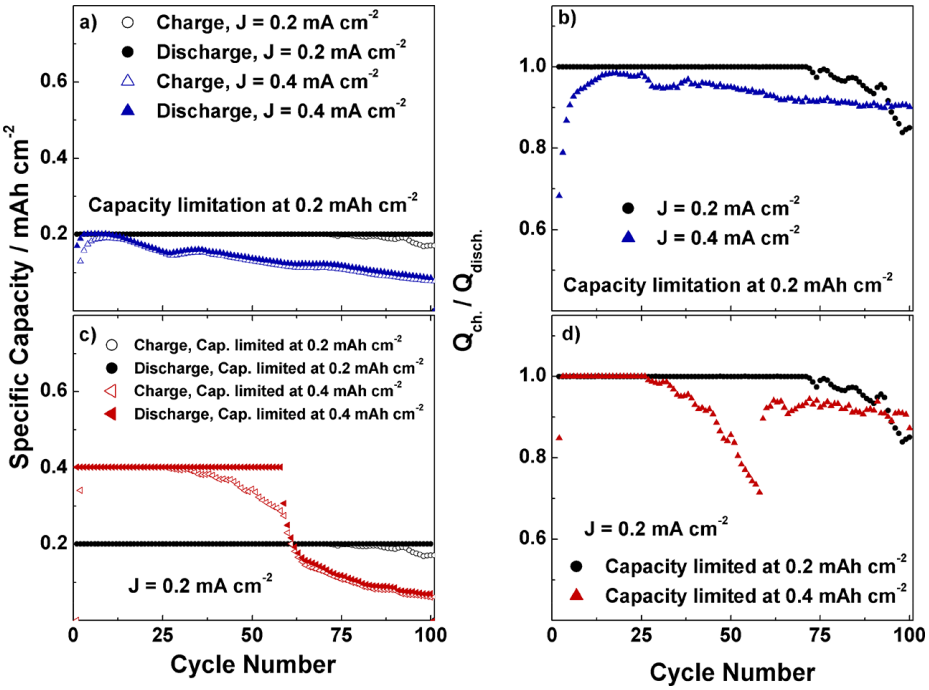

Figure 10. Cell performance upon cycling: (a,c) specific capacity and (b,d) charge reversibility (see text for more details).

Upon cycling the performance of the carbon-based cells addressed in this work were comparable with those reported in the available literature for similar configurations.[31]

At a current rate as large as 0.2 mA cm^{-2},a target capacity limitation of 0.2 mA h cm^{-2} (Figure 10 a) was successfully reached for more than 70 cycles, both in discharge and charge. In contrast, at higher rates, that is 0.4 mA cm^{-2}, the cell suddenly failed to supply the programmed maximum capacity. As reported in Figure 11 a, this was due to the increase of both the charge and discharge overvoltages at increasing current rates.[78]

A similar trend is observed if the discharge/charge capacity limitation is doubled. In fact, at the same current rate, that is, 0.2 mA cm^{-2}, identical cells reached the capacity limitation of 0.2 and 0.4 mA h cm^{-2} (Figure 10 c), both in discharge and charge for 71 and 26 cycles, respectively.

As regards the reversibility trends, at 0.2 mA cm^{-2} this parameter dropped below 1 after cycle 71 whereas at 0.4 mA cm^{-2} it was always smaller than unity (Figure 10 b). In the former case, the high charge reversibility recorded up to the 71st cycle is explained considering that the imposed capacity limit (0.2 mAh cm^{-2}) amounts to less than the 10% of the total discharge capacity of the cell when neither capacity nor voltage limits are imposed (see Figure 9). For what concerns the cell cycled at 0.2 mA cm^{-2} but with a doubled capacity limitation of 0.4 mAh cm^{-2}, the charge reversibility falls below 1 after cycle 26 (Figure 10 d). In this type of cell configuration a charge reversibility smaller than 1 has mainly to be related to the increase of charge overvoltages upon cycling (Figure 11 b). Despite the reversibility approaching 1, it is worth noting that this trend occurred even for the cell cycled at 0.2 mA cm^{-2}. So, in these systems even working in not "stressful" conditions leads to an accumulation of insoluble and not fully redox-reversible reaction products or degradation byproducts over the positive electrode surface. This is the cause to an increase of the overall electrode resistance and to large overvoltages.

Sample	Galvanostatic condition	Cycle of cell death
100 cycles	100 cycles at 0.4 mA h cm^{-2} limited capacity, end state in charge, J = 0.2 mA cm^{-2}	26
100 cycles (II)	100 cycles at 0.2 mA h cm^{-2} limited capacity, end state in charge, J = 0.2 mA cm^{-2}	72
100 cycles (III)	100 cycles at 0.2 mA h cm^{-2} limited capacity, end state in charge, J = 0.4 mA cm^{-2}	1

Table 2. Summary of the long-term tests and corresponding cycle of death of the carbon-based cells addressed in this work.

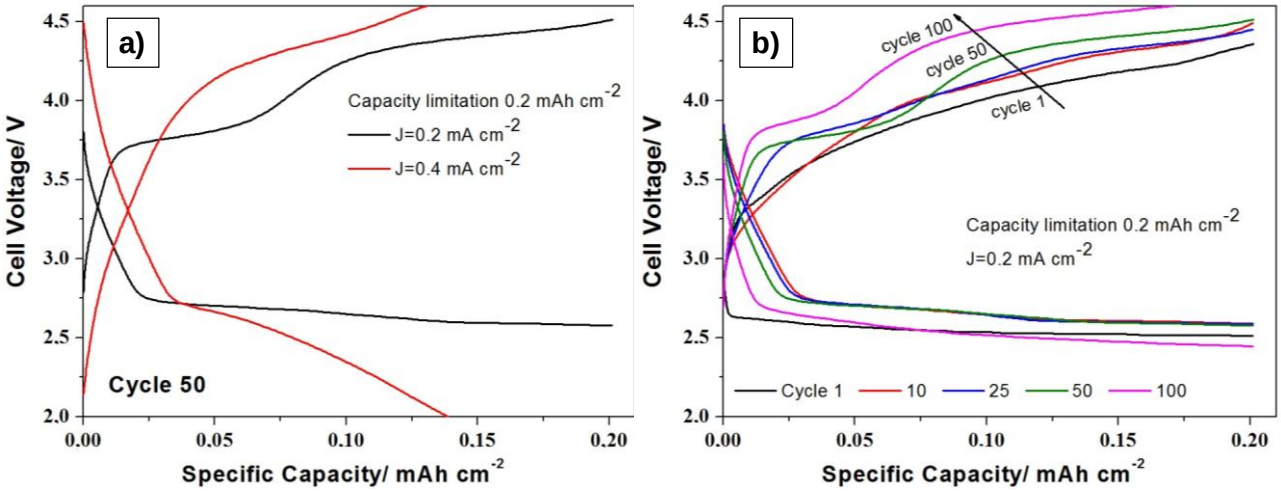

Figure 11. a) Comparison between the carbon-based cell voltage profiles (cycle 50) at 0.2 and 0.4 mAh cm^{-2}; b) carbon-based cell voltage profiles upon discharge and charge at 0.2 mAh cm^{-2}.

4.4. Chemical characterization

4.4.1. TEM

By means of transmission electron microscopy images, we observed the morphological change of the active carbon material due to operation in the cells. Particularly, the results of TEM measurements on cathodes recuperated from cells stopped at various stages of one discharge-charge cycle are shown in Figure 12 b-d. For comparison, an image of the pristine carbon Super P material is also shown (Figure 12 a). The preparation of the samples and other experimental details have been described in chapter 3, paragraph 3.2.2.
As expected, commercial Super P carbon is constituted by round-shaped nanoparticles with a diameter of 20−30 nm (Figure 12 a). Upon discharge, even at the high cut-off voltage of 2.6 V, a discontinuous polymer-like matrix appears and surrounds the carbon particles. This gelatinous deposit may be constituted by organic degradation by-products. Moreover, additional irregular and smaller nanoparticles with a diameter of 5−10

nm are visible. In the inset of the Figure 12 b, a tentative indexing of the partial FFT of the selected area is shown, attesting that these deposits may be constituted by Li_2O_2.

In fact, the interplanar distance found at 8 Å may be due to the reflection of the (001) plane of the peroxide lattice, to be compared to d(002) = 3.55 Å[79] for the layer stacking in graphitic carbons.

At the end of discharge (i.e. 2.0 V, see Figure 12 c), the original carbon particles are almost invisible due to an almost complete coverage by the amorphous matrix. However, after a complete cycle of discharge and charge (i.e. at 4.6 V, see Figure 12 d), the carbon particles recuperate their original round-shaped morphology. Moreover, no other deposits can be observed, suggesting a complete decomposition of the lithium peroxide and the degradation compounds by means of the OER and other competitive electrochemical oxidative processes, respectively. Particularly, carbonaceous degradation compounds could be removed from the cathodes by means of an oxidation to carbon dioxide.[1]

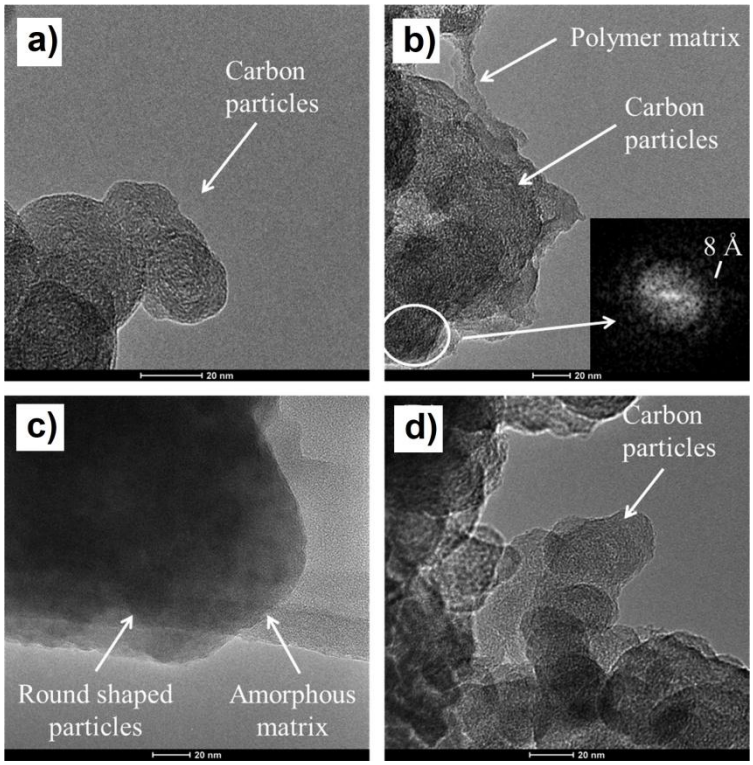

Figure 12. TEM images of materials from the carbon-based cathodes: (a) pristine; (b) sample discharged to 2.6 V; (c) sample discharged to 2.0 V; (d) sample discharged to 2.0 V and charged to 4.6 V. In the inset of Figure 12 b the calculated fast-Fourier transform (FFT) of the selected area and its tentative indexing are shown.

A TEM image of materials from the cathode extracted from the cell set to 100 cycles at J = 0.2 mA cm^{-2} limiting the capacity at 0.4 mAh cm^{-2} and died after the 26th cycle (see Table 2) is shown in Figure 13 b. For comparison another image of the carbon particles from the pristine electrode is shown in Figure 13 a.

The presence of diffuse smooth amorphous-like layers (thickness <10 nm) grown upon cycling over the carbon nanoparticles can be clearly observed. This evidence suggests that the observed removal of the degradation products from the cathode surface on one cycle is not ensured upon cycling, even at the high

charge voltage of 4.6 V. Due to their insulating character, the accumulation of these by-products has to be considered as one of the main reasons for the rise of the overvoltage and the cell death.

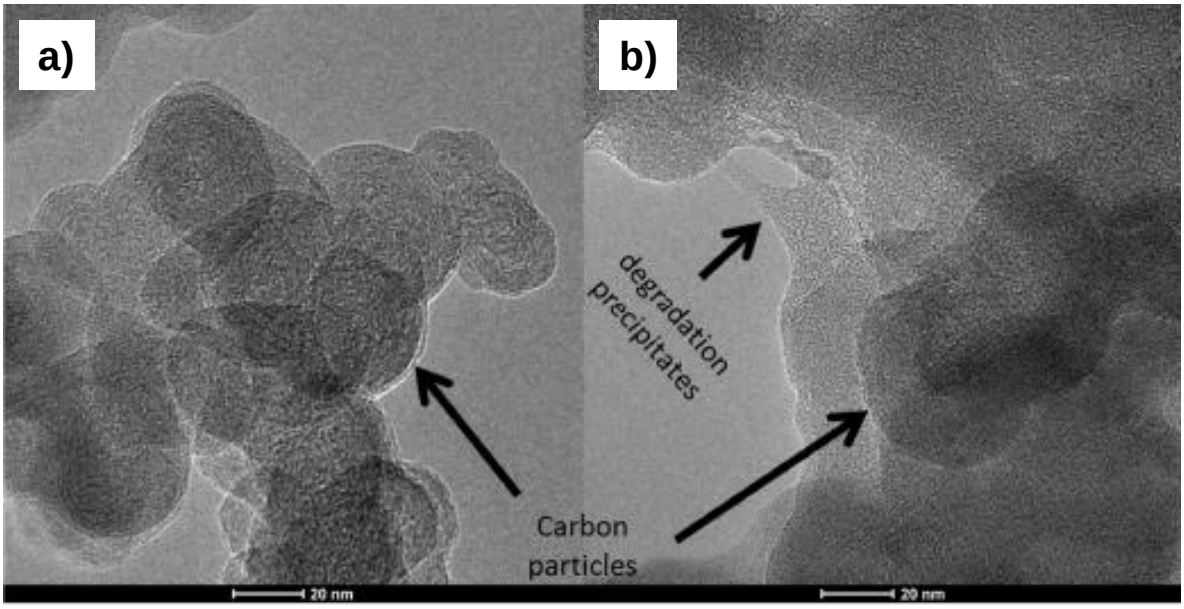

Figure 13. TEM images of materials from the carbon-based cathodes: (a) pristine; (b) from the cell cycled between 2.0 V and 4.6 V at J = 0.2 mA cm^{-2} limiting the capacity at 0.4 mAh cm^{-2}. The cell died after the 26th cycle.

4.4.2. FTIR spectroscopy

The ex-situ FTIR spectra of the discharged and charged cathodes on one cycle (see Table 1) are shown in Figure 14 e-i. The intensity of these spectra was normalized to the intensity at 1100 cm^{-1}, corresponding to the most intense absorption peak of TEGDME.[80] The reference spectra of a pristine carbon electrode and pure Li_2O, Li_2O_2, and Li_2CO_3 powders are also shown in Figure 14 a-d.

Both in the reference spectra for lithium oxide and lithium peroxide a broad band in the 400−600 cm^{-1} region is visible (Figure 14 a and b), related to the Li−O bond stretching.[81–87] Li_2CO_3 also gives a minor signal in this region (Figure 14 c), but its FTIR fingerprint bands are at about 860, 1440, and 1507 cm^{-1}. The first band is for the O=C−O bending mode, while the others are for its stretching vibrations.[84–86,88,89]

In the spectrum for the pristine cathode (Figure 14 d), an intense and broad band with maximum at 1020 cm^{-1} can be observed, possibly associated with the stretching mode of superficial oxidized groups of the carbon support, such as C−O−C and C=O.[90,91] At lower wavenumbers minor signals from the fluorinated binder vibrations are visible.[92,93]

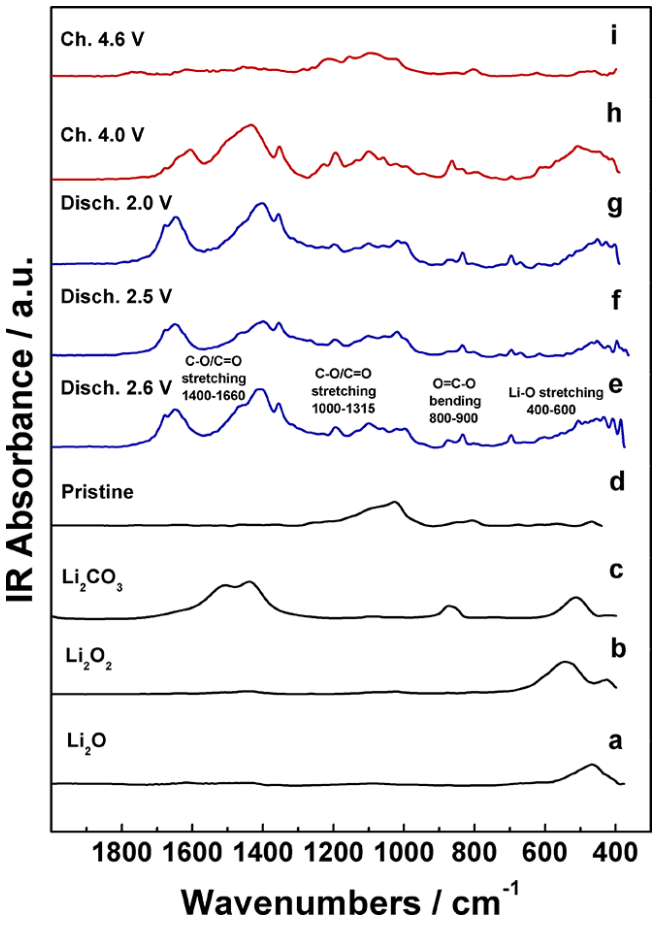

Figure 14. FTIR spectra of Li_2O, Li_2O_2, and Li_2CO_3 pure powders (spectra a–c), and of materials from pristine (spectrum d), discharged (spectra e–g), and cycled (spectra h and i) carbon-based electrodes addressed in this work.

Upon discharge, between 400 and 600 cm^{-1} region, where the stretching of Li–O bond is expected, a broad band increases, remains almost equal on charge to 4.0 V and disappears at 4.6 V (Figure 14 e–i). This trend may confirm the overall accumulation of oxidized lithium compounds upon discharge and their removal charging at high overvoltage.

On discharge (Figure 14 e–g), according to the growth of a polymer matrix possible made of degradation products observed by TEM, even at the high voltage of 2.6 V, signals increase in the spectral ranges for the C–O and C=O stretching mode. These peaks can be related to the accumulation of carbonates and alkylcarbonates (C–O and C=O symmetric stretching at 1020–1300 cm^{-1}, C–O and C=O asymmetric stretching at 1400–1660 cm^{-1})[81,82,84–86,89] and carboxylates (C=O symmetric stretching at 1500–1660 cm^{-1}).[81,82] However, the lack of bands in the 1700–1800 cm^{-1} region, where the asymmetrical stretching of C=O carboxylates groups is expected,[87,94] suggests the presence of these species only in the outermost layers of the samples.

As remembered in chapter 3, paragraph 3.2.3, unlike a surface-sensitive technique such as XPS, FTIR in transmission mode allows detection of compounds, such as inorganic Li_2CO_3, grown in the inner regions of

the samples. Thus, it is worth noting the apparent lack of any fingerprint for this last compound both in discharge and charge. This evidence suggests a peculiar degradation reactivity of the carbon electrodes in presence of the LiTFSI salt compared to that reported for other configurations.[37]

As shown in Figure 14 h and i, on charge the FTIR spectra demonstrate the permanence of carbonates and alkylcarbonates on the cathode charged to 4.0 V, whereas the same spectral features are completely absent when the cut-off voltage is increased to 4.6 V. These results are compatible with the recovery of the pristine morphology shown by TEM images at high overvoltage (Figure 12 d), and could be associated with oxidative removal of carbonaceous deposits.

4.4.3. XPS

Cathodes extracted from the cell stopped at different cut-off voltages of the first discharge−charge cycle (see Table 1) and from the battery set to 100 cycles at J = 0.2 mA cm^{-2} limiting the capacity at 0.4 mAh cm^{-2} (see Table 2, sample "100 cycles", died after 26 cycles) were analyzed ex-situ by means of X-ray photoelectron spectroscopy to investigate their surface composition. To facilitate the interpretation of these spectra, a pristine carbon electrode and a carbon electrode impregnated with the electrolyte (i.e. "uncycled" sample) were considered as benchmark materials. In chapter 3, paragraph 3.2.5, XPS experimental details have been described. In the case of the XPS analysis of the carbon-based electrodes, the C 1s BE of the $-CF_2-$ group at 292.0 eV belonging to the fluorinated polymer binder[95] of the pristine carbon electrode was used as an internal standard reference for the BE scale (accuracy of ±0.05 eV). The reason for this choice is explained in the results discussion. During the curve fitting procedure, the asymmetry was fixed to 0.0 for all the peaks except for the graphitic-like carbon peak in the C 1s region, for which it was set to 0.15.[96]

Photoemission regions on one cycle

In Figure 15 the **C 1s photoionization regions** of the samples extracted from the cell stopped at different cut-off voltages of the first discharge−charge cycle are shown.

For the pristine carbon support (Figure 15 a) we observe the typical contributions from a lowly ordered graphitic carbon material, whose main feature is the graphitic sp^2-hybridized C signal at 284.3 eV, slightly asymmetric at its high BE side.[96,97] The subsequent peak is attributable to defects that are mainly sp^3-hybridized C sites.[98] Considering all the spectra in Figure 15 a-g, its BE shift with respect to graphitic carbon was found to vary within the range +1.0 to +1.3 eV. At 286.7 eV a contribution from oxidized graphite (i.e. superficial epoxy and C=O groups)[98,99] can be found. The broad shake-up transition visible at 289.3 eV is typical of extended π-delocalized carbonaceous systems and accounts for 10% of the main feature intensity.[98] At 292.0 eV, there is a peak associated with the $-CF_2-$ groups of the fluorinated binder.[95] As previously mentioned, this signal was chosen as an internal reference for the BE scale. In fact, as evident in Figure 15, a BE position shift is experienced by some components (see green and black lines), as in the presence of a differential surface charging, apparently dependent on the working conditions of the cell. The $-CF_2-$

component was adopted as a reference for BE scale because it is associated with one of the constituents of the carbon cathode material. This aspect will be clarified later.

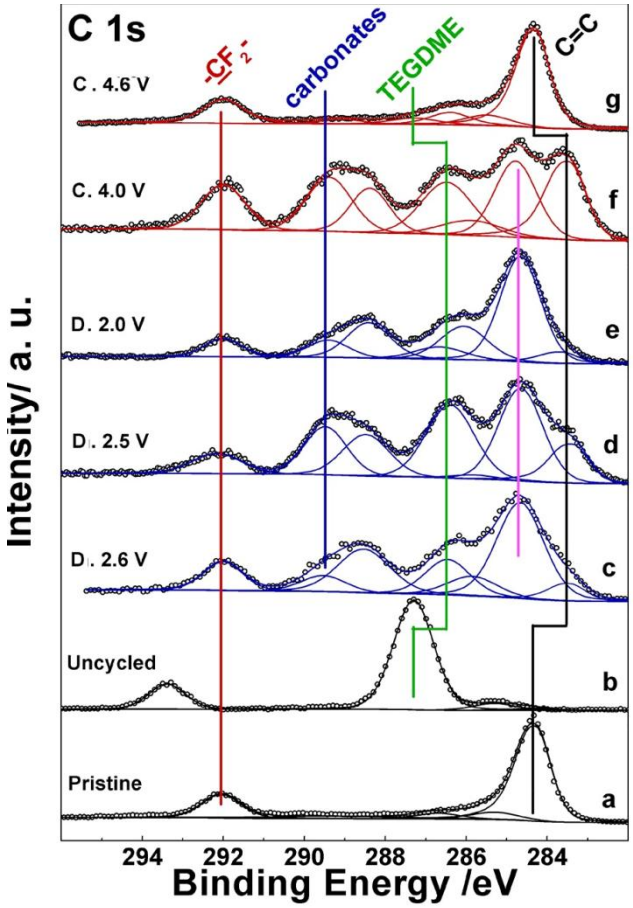

Figure 15. C 1s XP spectra of pristine and uncycled (black lines, spectra a and b), discharged (blue lines, spectra c−e), and cycled (red lines, spectra f and g) carbon cathodes. The positions of some peaks and their possible shifts are marked with colored lines.

In Figure 15 b, for the uncycled cathode, the peaks associated with the carbon support are hardly detectable since its surface was probably covered by a layer of electrolyte. Indeed, the additional features at 287.3 and 293.4 eV are associated with ethereal C−O bonds in physisorbed TEGDME[82,99] and with $-CF_3$ groups in $TFSI^-$ anion,[100,101] respectively. These signals are significantly reduced compared to those from carbon in the spectra of discharged and cycled cathodes (Figure 15 c−g) because the electrodes were rinsed with pure solvents after cycling.

Figure 15 c shows the effects of discharging the cell to 2.6 V. Signals similar to those for the pristine (Figure 15 a) can be identified, although with different relative intensities. However, a striking difference is the inversion of the relative intensities of the graphite-like carbon signal (see the black line in Figure 15) and the defect related peak (see the magenta line in Figure 15). In this case, a stronger enhancement is observed respect to that for previous studied carbon-based systems.[37] We speculated that on discharge, because of the low DN of the solvent and the $TFSI^-$ anion,[1,18,26] a thick layer of lithium oxides was deposited on the surface of the carbon foil. This thick precipitate may lead to the attenuation of outcoming photoelectrons and

contributed to the structural damage of the graphite C=C network. In presence of different Li salts, such as lithium triflate, ($LiSO_3CF_3$, i.e. LiTFO), the enhancement of such component has been reported to increase remarkably only when the discharge potential drops to 2.0 V.[37] Therefore, we evaluated that the use of LiTFSI had a more dramatic impact on the degradation of the carbon cathode. The predominance of the defects-related feature over the graphitic one is constant throughout the discharged samples (spectra c−e). On the other hand, such a feature is still present even in the sample charged to 4.0 V (spectrum f), whereas it is completely recovered to its pristine intensity in the sample charged to 4.6 V (spectrum g).We hypothesized that this behavior, similar to that found in the presence of LiTFO[37] and confirmed by other observations, can be explained referring to a partial decomposition, upon deep charging, of both lithium oxides and oxidized carbon by-products, both contributing to the elimination of the defects-related component by CO_2 release.[1]

Signals associated with carboxylate and carbonate groups[82,99–103] are present at 288.5 and 289.5 eV, respectively, in spectra c−f. Their presence calls for the occurrence of degradation phenomena related to the carbon cathode and the TEGDME solvent, possibly due to the exposition to Li_2O_2 particles.[39] It is worth noting that, in the presence of the LiTFSI salt, carboxylates were not found to behave as an intermediate step to the formation of carbonates, as reported in presence of other salts such as LITFO.[37] In fact, the variable relative intensity ratio of the two contributions throughout the spectra from discharged samples reveals that the two oxidized carbon moieties are not part of the same reaction path, but have different origins.

As to the presence of Li_2CO_3, that could nucleate on the cathode surface and in its pores due to the oxidant attacks from Li_2O_2 particles to the underlying carbon support,[1,104] it is not possible to discern whether the peak at 289.4 eV can be assigned to this compound or to variably substituted organic carbonates. As discussed later, the Li_2CO_3 fingerprint is also missing in Li 1s spectra, and its absence is in agreement with the corresponding FTIR spectra (see paragraph 4.4.2).

Charging the cell to 4.0 V (Figure 15 f) just few modifications respect to the discharged samples can be observed. In fact, oxidative degradation products (carboxylates, carbonates) are still present on the cathode surface, while defects of the graphitic network are only partly removed (see the magenta line in Figure 15). As evidenced adopting other lithium salts such as LiTFO,[37] in the first discharge/charge cycle of the cell, only an extreme charging up to 4.6 V can restore the original structure of the carbon cathode. In fact, at 4.6 V we observed a recovery of the original degree of defectiveness parallel to the abatement of oxidized carbon features (spectrum g).

As mentioned above, with reference to the $-CF_2-$ position (red line), a negative BE shift of 0.8 eV is experienced by the graphite-like (black line), defects (magenta line), and TEGDME (green line) peaks of spectra from the discharged and 4.0 V charged samples. On the other hand, according to the proposed energy calibration, the position of carbonates peak (blue line) is coherent with the literature.

Similar BE shifts have been reported by Edström et al. for signals associated with the solid electrolyte interphase (SEI) and bulk materials of Li-ion cells anodes.[105] The nature of such shift is not apparently chemical, and since it is found to be dependent on the presence of carboxylates/carbonates species, it may be related to changes in the state of charge at the electrode's surface. Edström et al.[105] explained a similar

phenomenon occurring in a Li-ion battery as due to the buildup of an electric potential gradient at the interface between the SEI and the anode during lithiation. Such gradient was attributed not much to the insertion of lithium but to the deposition of polar components, such as adsorbed solvent molecules and/or degradation products. In the case of the carbon-based cathodes addressed in this work, upon referencing to the binder $-CF_2-$ groups, the downshifted components are those related to the graphitic and defective carbon and the TEGDME solvent, which are likely localized in a portion of the electrode where a fractional negative charge is concentrated.[105] On the other hand, the degradation product's peak around 289 eV seems to maintain its chemical shift from the $-CF_2-$ group. Similar to the case of LiTFSI, also in the presence of LiTFO[19] this shift disappears upon charge to 4.6 eV, in parallel to the complete removal of carbonates. To explain this phenomenon, a mechanism similar to that described for Li-ion cells[105] was proposed to be in operation in $Li-O_2$ cells. Therefore, the negative BE shift for the C=C and TEGDME components of the carbon electrode used in the LiTFSI/TEGDME system was related to an electric potential gradient induced by accumulation of oxidized carbon byproducts formed during discharge, such as carbonates, which directly involve degradation of both Super P carbon and TEGDME solvent. On the other hand, the possible role of oxidized lithium compounds in contributing to the BE shift[105] was excluded, since the Li/C area ratio (see Table 3) was not found to be directly proportional to the extent of the BE shift itself.

Sample	**Galvanostatic condition ($J = 0.2$ mA cm^{-2})**	**Li/C atomic ratio**
D. 2.6 V	discharge to 2.6 V	0.055
D. 2.5 V	discharge to 2.5 V	0.043
D. 2.0 V	discharge to 2.0 V	0.034
C. 4.0 V	discharge to 2.0 V and charge to 4.0 V	0.032
C. 4.6 V	discharge to 2.0 V and charge to 4.6 V	--

Table 3. Li/C atomic ratios determined from XP spectra of the carbon-based cathodes recuperated from cells working in one cycle of discharge and charge.

The **Li 1s region** of the carbon cathodes XP spectra is shown in Figure 16.

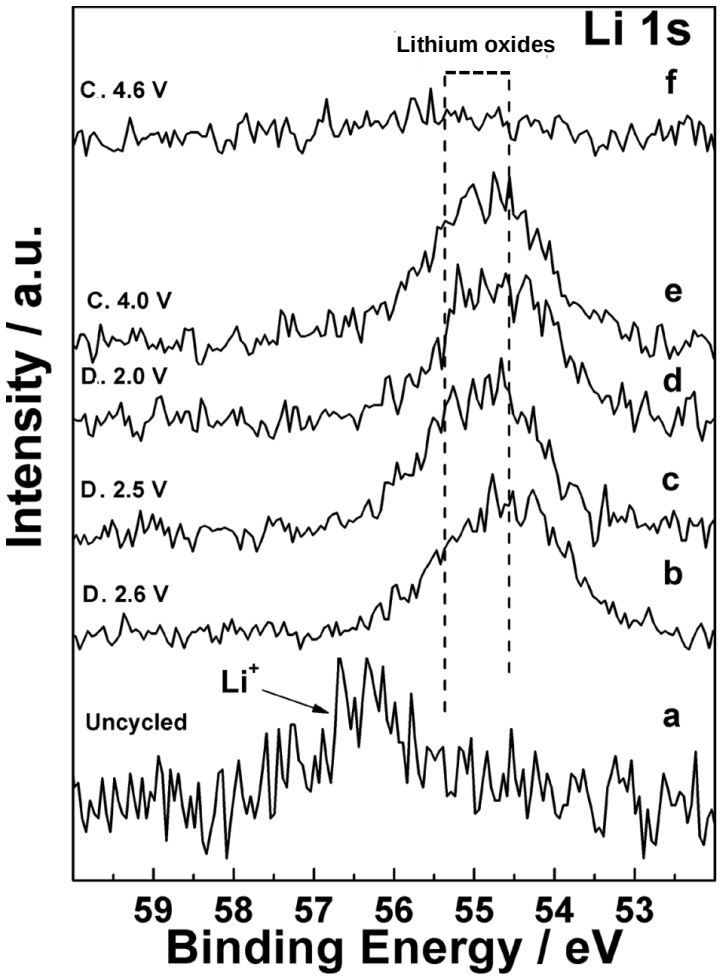

Figure 16. Li 1s XP spectra of uncycled (spectrum a), discharged (spectra b−d),and cycled (spectra e and f) carbon cathodes addressed in this work.

In the spectrum for the uncycled electrode we observe a single broad peak around 56.2 eV, attributable to the Li^+ ion in the LiTFSI salt.[106] Such signal is not visible in the spectra of the discharged and cycled cathodes, due to the rinsing procedure applied after the extraction of the cathodes from the cell. In spectra b−d, a broad signal can be detected in the range 54.0−55.5 eV, which can be attributed to the ORR products (i.e. lithium oxides) accumulated on the carbon cathodes upon discharge to 2.6, 2.5, and 2.0 V. Because of the inherent low photoionization cross section and large peak width, it is not possible to resolve Li_2O and Li_2O_2 different peaks in this area, while it seems more reasonable the presence of lithium peroxide.[82,104,107,108,109] As hypothesized from TEM observations, the presence of a well-pronounced Li 1s signal at the surface of a 2.6 V discharged cathode suggests that O_2 reduction took place already at 2.6 V. The presence of lithium peroxide is detected up to the 4.0 V on charge. However, charging the cell to 4.6 V (spectrum f) an abatement of Li 1s signal is observed, suggesting an almost complete decomposition of lithiated compounds at this highest potential.

Apparently, in all the spectra, no other signals can be observed, nor related to residual physisorbed LiTFSI salt molecules, neither from other species formed as reactions by-products, such as lithium carbonate or lithium fluoride.

In Figure 17 **the valence band photoionization region** (BE range 0−21.0 eV) is shown for the discharged and charged carbon cathodes (spectra c−g), as well as for pristine and uncycled carbon foil (spectra a and b).

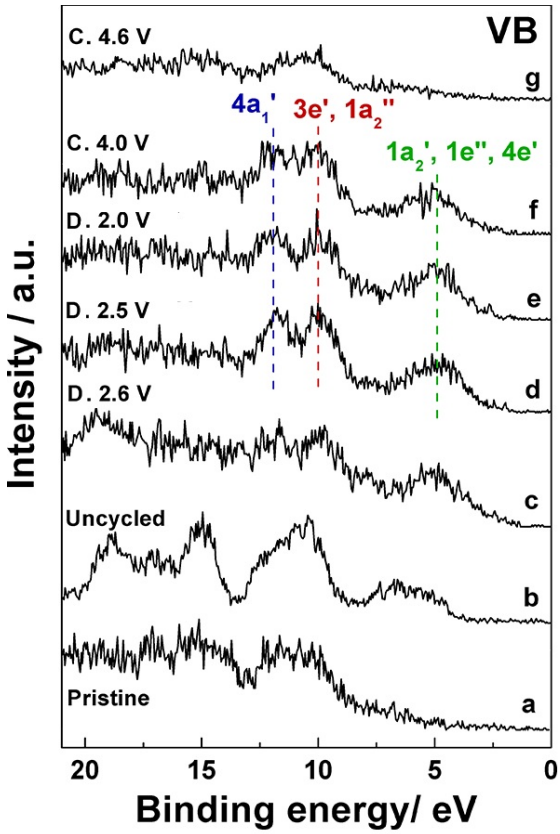

Figure 17. XP spectra of valence ionization region of pristine (spectrum a), uncycled (spectrum b), discharged (spectra c−e), and cycled (spectra f and g) carbon cathodes addressed in this work. Blue, red, and green dashed lines indicate the bands arising from ionization of CO_3^{2-} MOs.

The spectrum of the pristine sample (a) is dominated by the density of states (DOS) at the surface of the carbonaceous cathode, mostly due to lowly ordered graphitic material, which gradually rises only after about 5 eV, whereas is close to zero for BE< 5 eV.[110,111]

In the spectrum of the uncycled cathode (b), a sequence of at least five bands showing up roughly at 6.6, 10.4, 15.0, 17.0, and 18.8 eV can be found, attributable to ionization of molecular orbitals of the LiTFSI/TEGDME couple. Although not coupled to the TEGDME solvent, the $TFSI^-$ anion has been the object of a few studies, both theoretical (DFT) and spectroscopic (UPS/XPS),[112–116] which support these attributions.

In the spectra for the discharged and charged cathodes (Figure 17 c−g), the bands due to the LiTFSI/TEGDME couple can be considered absent because of the washing procedure. Three bands at 5.0

(green line), 10.0 (red line), and 12.0 (blue line) eV are visible in all the spectra, with a maximum of intensity in spectrum d (cathode discharged to 2.5 V). These peaks constitute a fingerprint of carbonate species on the cathodes surface.[117,118,119,120] As already mentioned, the presence of carbonate species was attributed to the oxidation of the carbon cathode surface. Indeed, the occurrence of photoionization features due to carbonate species in the valence region parallels the appearance of corresponding peaks at 290 eV in the C 1s spectra of the same samples (see Figure 15).

C 1s and Li 1s photoemission regions after multiple cycling

In Figure 18 is shown the **C 1s spectrum** acquired from the carbon electrodes cycled within the voltage range 2.0 V (discharge) and 4.6 V (charge) at J = 0.2 mA cm^{-2}, limited at the capacity value of 0.4 mAh cm^{-2} (see Table 2 and Figure 10). For comparison the spectrum of the pristine cathode, previously shown in Figure 15 a, is reported.

As to the spectrum of the 100-times cycled sample (b), the intensity of the defects-related peak (white, 284.8 eV) increases and new features arise for the carboxylate (cyan, 288.5 eV) and carbonate (blue, 289.5 eV).

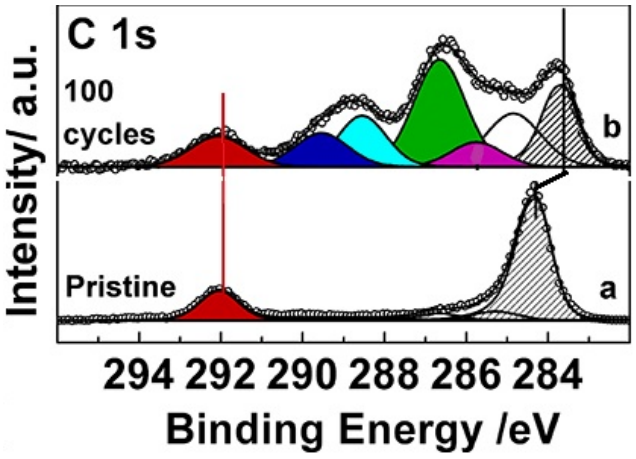

Figure 18. C 1s XP spectra of a) pristine and b) 100 cycles samples (see Table 2) addressed in this work. Color key: graphitic carbon (gray), defects (white), epoxyl (violet), TEGDME (green), carboxylate (cyan), carbonate (blue) and $-CF_2-$ (red).

Furthermore, the TEGDME contribution (green) is visible. Similar to the previous set of C 1s spectra (Figure 15), the BE scale was referenced to the binder $-CF_2-$ group value at 292.0 eV (red). Although the final voltage was 4.6 V, after 100 cycles partial degradation of the electrode material with accumulation of oxidized carbon by-products occurred. Furthermore, the presence of carboxylates/carbonates is accompanied by a −0.65 eV BE shift for the C=C, epoxyl- and defects-related components, which supports the above-mentioned role of such degradation species in this phenomenon. As to the possible accumulation of oxidized lithium compounds, after 100 discharge/charge cycles the presence of Li_2O_2 could be inferred observing the **Li 1s region** (Figure 19).

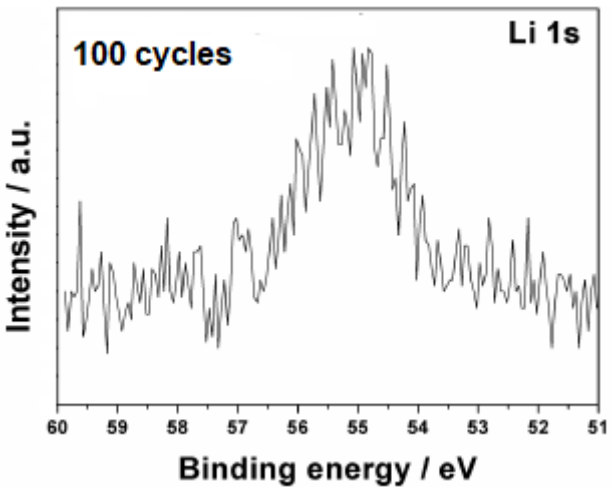

Figure 19. Li 1s XP spectrum of the 100 cycles sample (see Table 2) addressed in this work.

Overall, XP spectra of carbon electrodes that have worked in capacity-limited mode showed that 100 of such cycles, at least, lead to an accumulation of inert insoluble and not fully redox-reversible reaction products at the surface, which contribute to the buildup of considerable overvoltages, as discussed previously (see paragraph 4.3). Further evidence of this materials accumulation has been shown by TEM image in Figure 13.

4.5. Conclusions

The study on Li-O_2 cells assembled with a commercial carbon-based cathode in combination with the aprotic LiTFSI/TEGDME electrolyte solution highlighted the peculiar role of the $TFSI^-$ anion in the degradation process occurring at the surface of the positive electrode. The ex-situ characterization of the materials extracted from cells was performed by a powerful multi-technique approach. Particularly, from the analysis of the XP spectra, with the support of FTIR measurements and TEM images, a remarkable impact of the $TFSI^-$ anion on the oxidative degradation of the carbon cathode has been demonstrated, observing the appearance of carboxylate/carbonate organic groups on its surface and a simultaneous increase of defectivity within its graphitic domains. Interestingly, in contrast with the reports about the use of other lithium salts, the presence of inorganic Li_2CO_3 has been excluded.

A reversible modification of the carbon particles surface and morphology has been evaluated on the first discharge-charge cycle. In fact, on charge up to 4.6 V a total removal of degradation products and defectiveness has been detected, possibly accompanied by an evolution of electrochemically generated CO_2.

As regards the long-term stability of the cell, upon cycling the rise of the overvoltage both on discharge and charge was the major factor leading to the battery death after some cycles. By means of the ex-situ characterization of the materials extracted *post-mortem* from the cell, these phenomena have been related to

the not fully redox-reversible character of some insulating reactions products (i.e. Li_2O_2) and by-products (i.e. carboxylates and carbonates) that accumulated on the positive electrode cycle by cycle.

Moreover, for the first time in the field of $Li–O_2$ cells, the occurrence of the buildup of an electric potential gradient at the surface of the carbon cathode strictly associated with the formation of carbonate moieties chemically bound to the graphitic domains of the cathode material has been demonstrated. Such moieties, probably as a consequence of their directionality with respect to the graphitic planes, are responsible for the negative binding energy shift of the graphitic peak in the C 1s XP spectra. It is worth noting that such electric potential gradient has been demonstrated to be independent from the presence of lithiated compounds at the surface of the electrode.

Overall, the detrimental behavior of $TFSI^-$ anion with respect to the degradation issues in the carbon cathode used in this work can possibly be attributed to its moderately low donor number (DN). In fact, this feature, coupled with the low DN of the solvent used, inhibits the superoxide anion solvation and its departure from the electrode surface, while prolonging its confinement at the surface itself. In this way, the carbon cathode surface results in more serious exposure to the nucleophilic attacks of the freshly generated O_2^- and LiO_2 species, responsible both for the chemically driven formation of carbonate species during discharge and for the growth of an insulating compact layer of Li_2O_2. Furthermore, as recently reported, disproportionation of the surface-confined LiO_2 might be an active reaction path leading to the highly reactive $^1O_2$ species, which might severely contribute to degradation of the carbonaceous cathode.[32]

CHAPTER 5

Study on novel carbon-free cobaltite-based cathodes and corresponding powders

5.1. Aims

Despite the general good features of carbon based materials, which encouraged their use for positive electrodes in Li-O_2 cells, their oxidative degradation motivated us to test more stable configurations. The first study performed during the PhD activity, reported in chapter 4, confirmed this evidence and led to the search of a carbon-free material suitable as cathode for Li-O_2 batteries in combination with the ether-based electrolyte LiTFSI/TEGDME.

Inspired by the literature, we decided to adopt a nanostructured $NiCo_2O_4$ grown on Ni foam (see chapter 1, paragraph 1.3).

Preliminary tests of preparation of $NiCo_2O_4$ on Ni foam electrodes (NC@Ni) were attempted by means of a hydrothermal method introducing one at a time minor modifications to the reported procedure (see following sections). The aim was to favor the growth of more abundant $NiCo_2O_4$ and/or to improve its morphology and structure. Unfortunately, these attempts did not give significant results.

In order to enhance the catalytic activity of $NiCo_2O_4$ towards the cell reactions, we attempted to dope this material with transition metals different from Ni and Co.

M^{n+}-doped $NiCo_2O_4$ on Ni foam cathodes (NCM@Ni) were produced and tested in Li-O_2 cells. Only two materials, the Cr^{3+}-doped (NCCr@Ni) and the Zn^{2+}-doped (NCZn@Ni) ones, demonstrated superior electrochemical performance respect to the pure nickel cobaltite and were put at the center of a deeper electrochemical and chemical characterization. In order to complete the portrait about these novel materials, a parallel study on the corresponding powders (i.e. NC, NCCr and NCZn) was realized as well.

5.2. Samples preparation

The procedure for the hydrothermal synthesis of the $NiCo_2O_4$ on Ni foam samples was derived from the literature.[50]

The Ni foam was punched into discs with a diameter of 14 mm, degreased with acetone, etched with HCl 6 M for 10 min, rinsed with deionized water and absolute ethanol and then dried at 333 K. The average weight of each disc was 54 mg.

0.474 g $CoCl_2 \cdot 6H_2O$ and 0.237 g $NiCl_2 \cdot 6H_2O$ as cobaltite precursors and 0.18 g urea as precipitating agent were dissolved in 30 mL of distilled H_2O. After magnetic stirring for 15 min (Figure 20 a), the resulting pink solution was transferred into a 50 mL Teflon lined stainless autoclave (Figure 20 b) together with some pre-treated Ni foam discs, sealed and kept at 120 °C for 6 h. The obtained composite discs were washed with water, dried at 60 °C for 10 min and finally calcined at 300 °C for 4 h in air. The average cobaltite loading on each disk was 1 mg cm^{-2} (Figure 20 c).

Figure 20. (a) The pink aqueous solution of the nickel cobaltite precursors and urea under magnetic stirring; (b) the Teflon lined stainless autoclave used for the hydrothermal synthesis; (c) the obtained composite discs of $NiCo_2O_4$ on Ni foam.

As reported in literature,[53] the $NiCo_2O_4$ growth mechanism is described by the following reactions:

$$Ni^{2+} + Co^{2+} + 4OH^- \rightarrow Ni(OH)_2 + Co(OH)_2 \quad (5)$$

$$2Ni(OH)_2 + 4Co(OH)_2 \xrightarrow{\Delta} 2NiCo_2O_4 + 6H_2O \quad (6)$$

The precipitation of nickel and cobalt hydroxides on the Ni foam discs is possible at the basic pH of the aqueous solution induced by the urea hydrolysis (5). During calcination, the dehydration of the sample takes place leading to the $NiCo_2O_4$ formation (6).

A full characterization of the materials is proposed in the subsequent paragraphs. A SEM image of a NC@Ni sample is reported, in comparison with a picture of the same material derived from the literature (Figure21).[50] Fast SEM observations were really useful to understand if a synthesis was successful or failed due to possible experimental drawbacks.

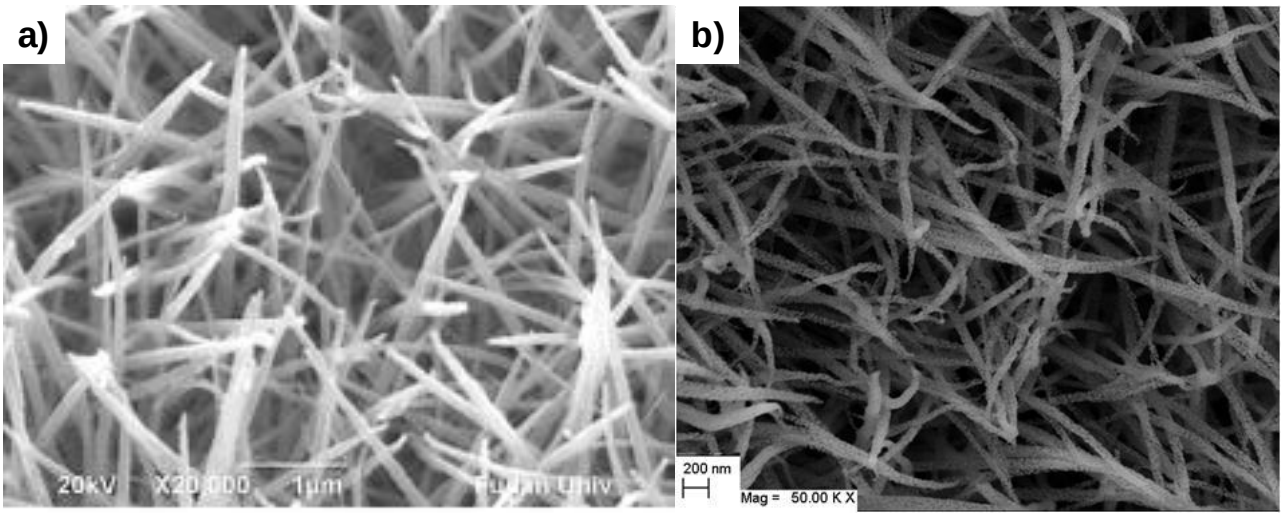

Figure 21. SEM images of $NiCo_2O_4$ on Ni foam samples (a) derived from literature (see Ref. [50] and (b) successfully synthesized in our laboratory.

5.2.1. Attempts to modify the synthesis procedure and results

Some attempts of modification of the NC@Ni synthesis procedure were performed with the aim of depositing more abundant active material on the Ni foam and/or increase the nickel cobaltite grade of nanostructure. In such ways, more catalytic sites could be active due to an higher surface exposition. All of these experiments revealed ineffective. Here two examples are reported.

Upon setting the hydrothermal bath at higher temperature (i.e. 180 °C instead of 120 °C), the synthesized electrodes turned darker than those produced at low temperature, so a more abundant growth of cobaltite could be inferred. Nevertheless, Li-O_2 cells assembled with these materials as cathode were affected by electrical contact problems (i.e. short circuit conditions) or demonstrated very low discharge capacities.

The addition of ammonium fluoride (NH_4F) to the synthesis solution seemed to favor the growth of more abundant $NiCo_2O_4$, particularly on one side of the Ni foam discs, according with the general idea that salt crystals act as crystallization nuclei. Despite this, the corresponding Li-O_2 cells failed to supply the minimal request discharge capacity (i.e. that performed by the cathode synthesized by means of the unmodified procedure). SEM measurements demonstrated that this synthesis failed (Figure 22 a): fibrous aggregates and platelets instead of the typical $NiCo_2O_4$ nanofibers were grown onto the Ni foam.

.

5.2.2. Attempts to doping and results

No modifications of the NC@Ni synthesis procedure can be introduced without compromising its success. So, to produce an innovative material, the idea was to insert transition metal ions (M^{n+}) as dopants in the nickel cobaltite spinel lattice. The goal was to register an higher catalytic effect towards the ORR and/or the OER respect to the pure NC@Ni (i.e. higher discharge capacity and reversibility, lower overvoltages, increasing long-term stability etc.). These materials were prepared dissolving weighted amounts of the

dopants precursors in the synthesis solution. The dopant molar concentration was equal to 1/10 compared to that of cobalt. No other changes in the synthesis procedure were introduced.

The metal ions tested as dopants, the weighted amounts of their precursors and the results of these doping attempts, evaluated on the basis of the performance of Li-O_2 cells assembled with these materials as positive electrodes, are summarized in Table 4.

Dopant	Precursor and weight		Result
Cr^{3+}	$Cr(NO_3)_3 \cdot 9H_2O$	0.080 g	Positive
Zn^{2+}	$Zn(NO_3)_2 \cdot 6H_2O$	0.059 g	Positive
Cu^{+}	CuCl	0.020 g	Negative
Ru^{3+}	$RuCl_3$	0.041 g	Negative
Pd^{2+}	$PdCl_2$	0.035 g	Negative

Table 4. Summary of the metal ions tested as $NiCo_2O_4$ dopants, the weighted amounts of their precursors (dopant molar concentration equal to 1/10 respect to that of cobalt) and the results of these doping attempts (based on the electrochemical response of corresponding Li-O_2 cells).

Here, a discussion about the doping failed attempts is proposed. The electrochemical and chemical characterization of the successful NCCr@Ni and NCZn@Ni materials is reported in the other paragraphs of this chapter.

Li-O_2 cells assembled with NCCu@Ni, NCRu@Ni and NCPd@Ni as positive electrodes demonstrated electrical contact problems and/or failed to supply the minimum desired discharge capacity (i.e. that of the pure NC@Ni). SEM images revealed that Cu^{+}, Ru^{3+} and Pd^{2+} dopants had remarkable effects on the nickel cobaltite amount and morphology (Figure 22 b-d).

NCCu@Ni (Figure 22 b) was constituted by compact and rigid nanowires, much less porous than those of NC@Ni. The Ru(III)-doped sample (Figure 22 c) showed isolated large wires, accompanied by some pseudo-cubic aggregates, possibly made by a phase different from $NiCo_2O_4$ (i.e. CoO and/or NiO). Instead of nanowires, nanoflowers constituted the NCPd@Ni sample (Figure 22 d), suggesting the growth of a separate phase of metallic Pd.[121,122]

Explaining the unsuitability of these ions as dopants for the $NiCo_2O_4$ is beyond the PhD research topic. However, one can speculate that the larger Shannon ionic radii of Ru(III) and Pd(II) (i.e. 0.820 and 0.860 Å, respectively) than those of Ni(II)/Ni(III) and Co(II)/Co(III) (i.e. 0.550, 0.560, 0.580, 0.545 Å, respectively)[123] possibly hampered their introduction in the cobaltite spinel lattice.

It is worth noting that, in the case of the NCCr@Ni and NCZn@Ni materials, the dimensions of the dopants were not an obstacle for the good result of the synthesis. In fact, both Cr(III) and Zn(II) have Shannon ionic radii similar to those of Ni and Co (i.e. 0.615 and 0.740 Å, respectively).[123]

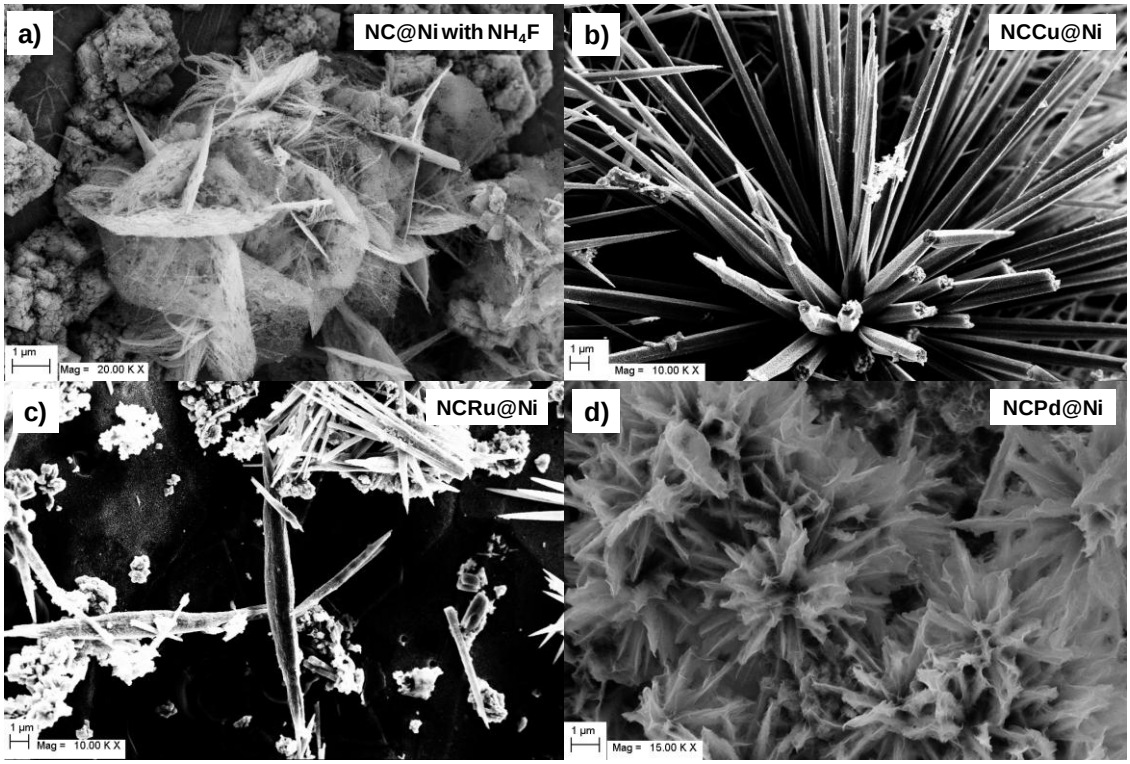

Figure 22. SEM images of materials produced by means of failed synthesis due to (a) modification of the procedure (i.e. addition of NH_4F in the precursors solution); doping with not suitable metal ions (b) Cu^{+}, (c) Ru^{3+} and (d) Pd^{2+}.

The powders corresponding to the successfully doped materials (i.e. NCCr and NCZn) and the pure one (i.e. NC) as reference sample were synthesized with minor modification of the literature procedure. In this case, no Ni foam discs were introduced in the Teflon stainless lined autoclave. Then, the muddy pink deposit formed after the hydrothermal treatment was filtered on a Whatman mesoporous alumina filter and washed with distilled H_2O and EtOH. After drying at 60 °C for 15 min, the resulting powders were calcined at 300 °C for 4h.

5.3. Electrochemical tests on NC@Ni, NCCr@Ni and NCZn@Ni electrodes

As described in chapter 3, paragraph 3.1, Li-O_2 cells and electrolyte solutions were prepared in an Iteco Engineering argon-filled glovebox with moisture concentration below 0.1 ppm. In the case of the study of the cobaltite-based electrodes, the batteries were assembled by using an EC-CELL type ECC-Air (Figure 5 b) consisting of a stainless steel current collector, a metallic lithium foil as anode, a glass-fiber separator (Whatman, 18 mm in diameter) impregnated with 250 µL of a 1 m electrolyte solution, and the synthesized NC@Ni or NCCr@Ni or NCZn@Ni materials as cathode.

The salt and the porous cathodes were dried at 110 °C overnight under vacuum before use. The solvent was used after drying/storage on regenerated 3 Å molecular sieves (Sigma-Aldrich) and lithium chips for at least

15 days in a glovebox. Li−O_2 cells were filled with pure O_2 (5.0 purity spilled from a high-pressure cylinder through stainless steel gas lines, preliminarily evacuated, equipped with a molecular sieve-filled moisture trap), setting a static final pressure of 1.0 bar in the dead volume (about 3 cm^3) above the porous electrode.

In a first set of electrochemical tests, galvanostatic cycling of the cells was carried out, connecting to a MTI Corp. battery cycler, setting to a single cycle with a current density of 0.025 mA cm^{-2} and stopping at cut-off voltage of 2.0 V in discharge and 4.1 V in charge. The measured capacity was normalized dividing by the geometrical area of the positive electrodes (1.54 cm^2). The reversibility was calculated as the ratio between the capacities measured on charge and on discharge. In the case of the NCCr@Ni electrode, the effect on the measured discharge capacity and voltage hysteresis of decreasing the applied current density from 0.1 mA cm^{-2} to 0.025 cm^{-2} was also tested.[124]

A second type of experiments were devoted to test the long-term performance of the cells, so galvanostatic cycling were carried out imposing capacity limit of 0.1 mAh cm^{-2} and current density value of 0.2 mA cm^{-2}, while the number of cycles was set to 100. For the NCCr@Ni electrode, the capacity limit was then increased to 0.2 mAh cm^{-2} at two different current density values of 0.1 mA cm^{-2} and 0.2 mA cm^{-2}.[124]

Pseudo-Tafel plots at different temperatures were also derived from intermitted galvanostatic titrations experiments performed at various current densities. All the electrodes were partially pre-discharged with a voltage cut-off fixed at 2.6 V at 0.025 mA cm^{-2} and then, after 12 h of relaxation in open circuit conditions (OCV), a constant current density signal (J) was applied followed by 6 h of cell relaxation in OCV, in order to restore after each polarization the starting electrode composition. Nine J values were sampled both in ORR and OER (±1.3, ±3.3, ±6.5, ±13,±32.5, ±65, ±130, ±325 μA cm^{-2}, respectively) by partially discharging/charging the electrodes with a capacity limitation of ±0.01 mAh cm^{-2}.

After the electrochemical measurements, the cells were disassembled in glovebox. Their cathodes were recuperated and washed in TEGDME and in THF to remove the excess electrolyte, and dried under vacuum at room temperature. Samples derived from the first and the second type of experiments were chemically characterized by means of a multi-technique approach. Pristine NC@Ni or NCCr@Ni or NCZn@Ni were considered as benchmarks samples.

5.3.1. Voltage limited performance on one cycle

The performance on one cycle of discharge/charge between 2.0 V and 4.1 V at J = 0.025 mA cm^{-2} of the NC@Ni, NCCr@Ni and NCZn@Ni materials in Li-O_2 cells are compared in Figure 23 a. At J = 0.025 mA cm^{-2}, the NCCr@Ni and NCZn@Ni electrodes outperform four times and three times, respectively, the discharge capacity of the pure NC@Ni one. Moreover, both the doped samples show a larger Coulombic efficiency (i.e. about 100%, while for NC@Ni is 88%) and, particularly in the case of the Cr(III)-doped cathode, smaller overvoltages affect the cell both in discharge and charge. As expected, decreasing the applied current density, the discharge capacity supplied by the NCCr@Ni electrode increases (Fig. 23 b), and

quadruplicates at J = 0.025 mA cm^{-2} compared to J = 0.1 mA cm^{-2}. Moreover, the corresponding voltage hysteresis between ORR and OER decreases.[124]

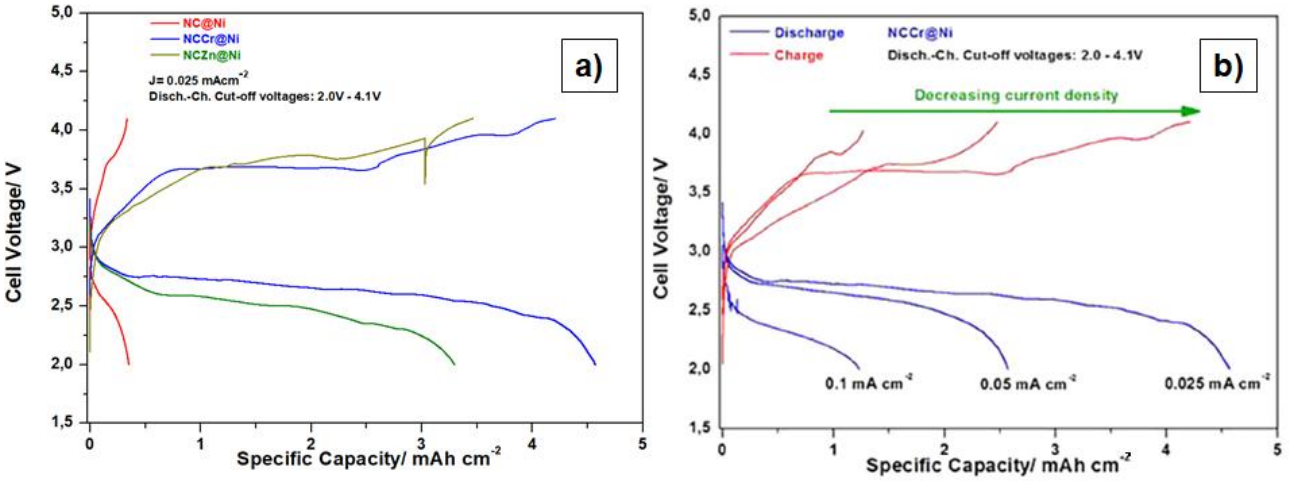

Figure 23. (a) Comparison between the performance on one galvanostatic cycle between 2.0 and 4.1 V at J = 0.025 mA cm^{-2} of the NC@Ni (red curve), NCCr@Ni (blue curve) and NCZn@Ni (green curve) materials; (b) effect of decreasing the applied current density on one discharge/charge cycle for the NCCr@Ni material.

5.3.2. Long-term performance

The Cr(III) and Zn(II) doping had a remarkable beneficial effect on the long-term stability of the cell. However, in this case, the most striking performance was for the NCCr@Ni cathode. As reported in Figure 24 a, at J = 0.2 mA cm^{-2}, the capacity limitation of 0.1 mAh cm^{-2} is successfully reached with a Coulombic efficiency of 100% between charge and discharge for 15 and 52 cycles by the Zn(II) and the Cr(III) –doped electrodes, respectively, whereas the NC@Ni one fails at cycle 1 (data not shown).

Due to its particular effect, the long-term performance of the NCCr@Ni positive electrode were further investigated, varying both the current density and the capacity limitation (Figure 24 b).[124]

As expected, at the same current density (i.e. 0.2 mA cm^{-2}) but with the higher capacity limitation of 0.2 mAh cm^{-2} the NCCr@Ni electrode fails earlier (i.e. at cycle 16, blue spheres). An intermediate performance is registered at the lower current density of J = 0.1 mA cm^{-2} with a capacity limitation of 0.2 mA cm^{-2} (i.e. cell death at cycle 46, blue triangles).

As discussed in the previous chapter, the carbon cathodes failure had to be related to the accumulation of degradation by-products cycle-by-cycle on its surface and in its pores.[19] In this case, instead, being assembled with positive electrodes inert to oxidative chemical attacks, the cobaltite-based cell death has possibly to be motivated referring to the organic solvent degradation.

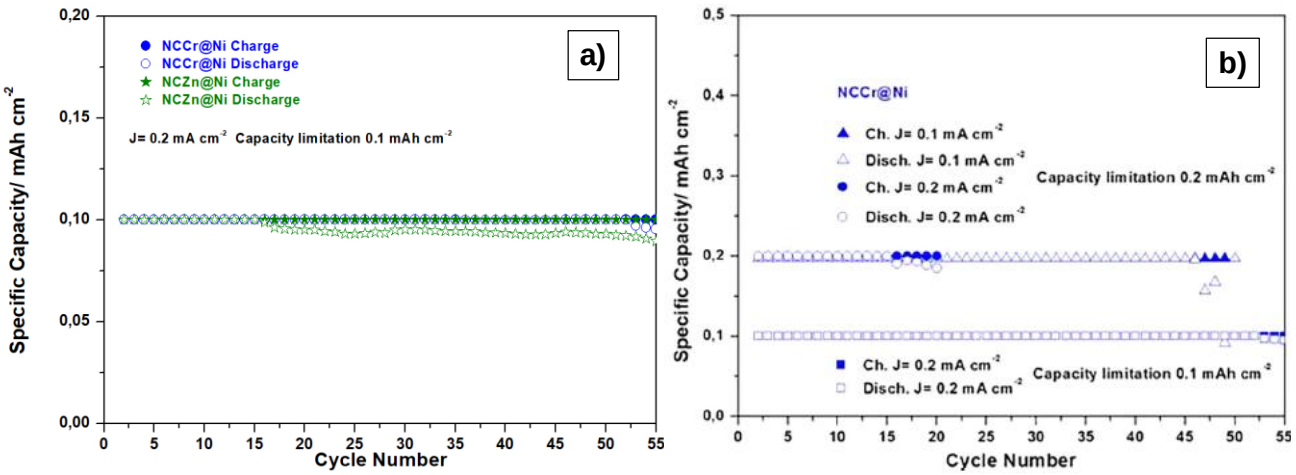

Figure 24. (a) Comparison between the performance upon cycling of the NCCr@Ni (blue spheres) and the NCZn@Ni (green stars) electrodes; (b) cycling performance in various galvanostatic conditions (capacity limitations and current density) for the NCCr@Ni sample.

5.3.3. Pseudo-Tafel plots

As reported in the following paragraphs, by means of a multi-technique characterization we demonstrated that the NC@Ni, NCCr@Ni and NCZn@Ni materials display alike morphology and structure. Moreover, the catalyst mass loading onto the Ni mesh was similar. So, the enhanced electrochemical response of the doped materials was supposed to be related to an improvement in the electro-catalytic properties respect to the pure one.

This aspect was further investigated, recording the ORR and OER overvoltages at different current density by means of the pseudo-Tafel plots at T= 22 °C shown in Figure 25 for the NCCr@Ni and NCZn@Ni, compared with that for the pure NC@Ni.

On discharge both the NCCr@Ni (blue triangles) and the NCZn@Ni (green stars) electrodes show smaller overvoltages (η_{ORR}) compared to the undoped NC@Ni (red spheres) ones. Instead, on charge the Cr(III)-doped material outperforms both the Zn(II)-doped and the pure nickel cobaltite in terms of small overvoltages (η_{OER}). This trend is in line with the performance on one cycle (see Figure 23 a) and proves the increase of the electro-catalytic power induced by doping. Moreover, the higher catalytic effect of Cr(III) on the OER possibly leads to the enhanced reversibility upon cycling and explains the better performance of the NCCr@Ni electrode in long-term test (see Figure 24).

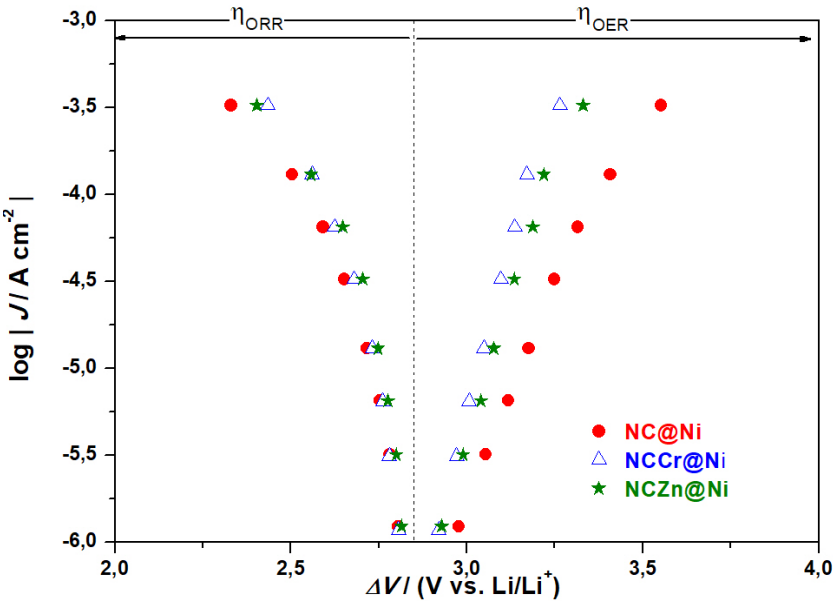

Figure 25. Pseudo-Tafel plots registered at T= 22 °C for the NC@Ni (red spheres), NCCr@Ni (blue triangles) and NCZn@Ni (green stars) materials addressed in this work.

As explained in chapter 1, paragraph 1.2, the use of an electrolyte solution in which both the lithium salt anion and the solvent have moderately low DNs, such as $TFSI^-$ and TEGDME, favors the growth of Li_2O_2 by means of a surface-mediated process.[3,20–28]

According to literature,[125,126] when this mechanism is working, the kinetics of Li_2O_2 formation and dissolution appears limited by the following reactions:

$$Li^+ + O_2{}^* + e^- \rightarrow LiO_2{}^* \quad (7)$$

$$Li_2O_2 \rightarrow LiO_2{}^* + Li^+ + e^- \quad (8)$$

where * indicate the species adsorbed on the cathode surface. In this view, in the experimental pseudo-Tafel plots, both on discharge and charge, the current density *J* should depend linearly on the concentration of O_2* at constant temperature and electrolyte composition.

Then, *J* can be written as a function of the overpotential η by means of the equation:

$$J \approx -[\mathrm{Li}^+]O_2{}^* exp\left(-\frac{\Delta G_0^{\pm}}{k_B T}\right) exp\left(\frac{\alpha e \eta}{k_B T}\right) \quad (9)$$

where $[Li^+]$ and O_2* are the reactants concentrations at or near the surface, $\Delta G_0^{\pm}$ is the kinetic barrier to the limiting reactions (7) or (8) at the equilibrium potential, α is the symmetric factor generally assumed equal to 0.5 both on discharge and on charge, *e* is the charge of one electron and η is the overpotential.[125,126]

The pseudo-Tafel plots for the NC@Ni, NCCr@Ni and NCZn@Ni electrodes were recorded at different temperatures. Assuming *J* constant at two temperatures (i.e. 22 °C and 55 °C), the kinetic barriers $\Delta G_0^{\pm}$ to the limiting reactions (7) and (8) on discharge and charge were estimated by means of the equation:

$$\Delta G_0^{\pm} = \alpha e \left(\frac{T_1\eta_2 - T_2\eta_1}{T_1 - T_2}\right) \quad (10)$$

The results of these calculations are summarized in Table 5.

Sample	$\Delta G_0^{\pm}$ ORR [eV]	$\Delta G_0^{\pm}$ OER [eV]
NC@Ni	0.19 ± 0.01	0.17 ± 0.01
NCCr@Ni	0.14 ± 0.01	0.17 ± 0.01
NCZn@Ni	0.16 ± 0.02	0.17 ± 0.02

Table 5. Kinetic barriers $\Delta G_0^{\pm}$ for the limiting reactions on discharge (ORR) and on charge (OER) calculated from the pseudo-Tafel plot data at two different temperatures for the NC@Ni, NCCr@Ni and NCZn@Ni materials.

It is worth noting that the calculated $\Delta G_0^{\pm}$ are an order of magnitude smaller than those reported previously for carbon-based cathodes,[125] suggesting boosted kinetics for both the ORR and the OER on cobaltite-based materials.

Interestingly, on discharge (ORR) the $\Delta G_0^{\pm}$ trend reflects those of the η_{ORR} values at T= 22 °C (Figure 25). So, we tentatively explained the enhancement of the ORR kinetics for the Cr(III) and Zn(II) –doped electrodes by considering a possible alteration of their surface chemistry (i.e. the presence of different and/or differently concentrated catalytic centers) respect to the pure material that could modify the O_2 and LiO_2 adsorption kinetics and increase their concentration as reagents on the surface.

On the contrary, despite the higher difference between the η_{OER} values at T= 22 °C for NCCr@Ni respect to those for NC@Ni and NCZn@Ni, on charge (OER) the calculated $\Delta G_0^{\pm}$ are similar.

We speculated that, in contrast with the carbon-based system studied in the reference [125], the path (8) could not be the OER kinetics limiting one when a cobaltite-based cathode is adopted, due to the growth of low dimension and low crystallinity lithium oxides aggregates on its surface and pores (see paragraphs 5.4.1 and 5.4.2 about our XRD and SEM characterization of post-mortem cathodes). In fact, charge transfer in equation (8) mainly occurs at oxygen-enriched crystal facets and sites at the surface of "well-formed" Li_2O_2 particles.[125]

A study on the alteration of the nickel cobaltite chemical surface composition in terms of transition metal atomic concentrations due to doping was performed by means of XPS and is reported in paragraph 5.4.4.

5.4. Chemical characterization of NC@Ni, NCCr@Ni and NCZn@Ni

5.4.1. XRD

By means of the equipment described in paragraph 3.2.4, XRD experiments were carried out on NC@Ni, NCCr@Ni and NCZn@Ni pristine electrodes in the range 20° - 70°, setting a step of 0.05° and an acquisition time of 6s. In Figure 26 the diffraction patterns are reported in the range 24° - 35° to cut-off the major peak of the Ni support. For comparison references XRD for $NiCo_2O_4$ and NiO are also shown.

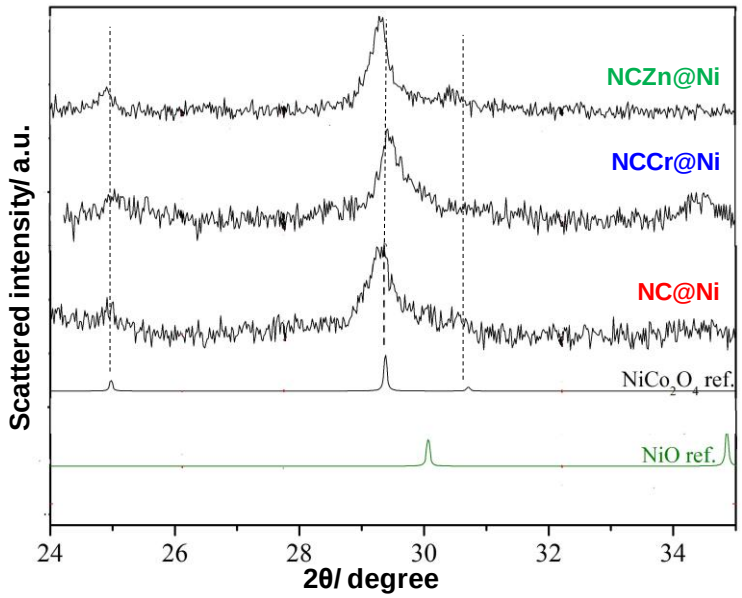

Figure 26. Diffraction patterns of the NC@Ni, NCCr@Ni and NCZn@Ni materials addressed in this work in comparison with those of $NiCo_2O_4$ and NiO derived from literature.

For all the materials, the diffraction patterns show the characteristic peaks of a cubic $NiCo_2O_4$ phase crystallized in an inverse spinel lattice (space group Fd3m 227, JCPDS Card No.73-1702) where Ni occupies the octahedral 16d sites and Co is distributed in both the 16d and the tetrahedral 8a sites.[47] In the selected range, only a minor contribution around 30° can be attributed to traces of NiO (space group Fm3m 225, JCPDS Card No. 73-1523)[127] possibly grown from the Ni mesh due to its spontaneous corrosion in alkaline aqueous solutions.[128] The peaks for the doped samples appear slightly shifted compared to those for the undoped one. This evidence accords with a change in the crystal cell size due to doping. The calculate cell parameters of the NCCr@Ni and the NCZn@Ni materials are larger (i.e. a = 8.128 ± 0.003 Å and a = 8.130 ± 0.004 Å, respectively) compared to the undoped NC@Ni (i.e. a = 8.117 ± 0.005 Å, in line with Ref. [129])[129]. The cell expansion in the doped samples matches well with the substitution in the lattice of Ni(II)/Ni(III) and Co(II)/Co(III) ions with the larger Cr(III) and Zn(II) ions (Shannon ionic radii 0.550, 0.560, 0.580, 0.545, 0.615 and 0.740 Å for Ni(II), Ni(III), Co(II), Co(III), Cr(III) and Zn(II), respectively)[123].

Low S/N ratio affected the diffraction patterns in Figure 26 due to the low amount of nickel cobaltite grown on the Ni foam. So, to confirm that doping did not induce changes in the $NiCo_2O_4$ spinel lattice, XRD measurements were performed for the NC, NCCr and NCZn powders. Thanks to the absence of the Ni foam, the full range of acquisition is reported in Figure 27. No differences are detectable between the samples.

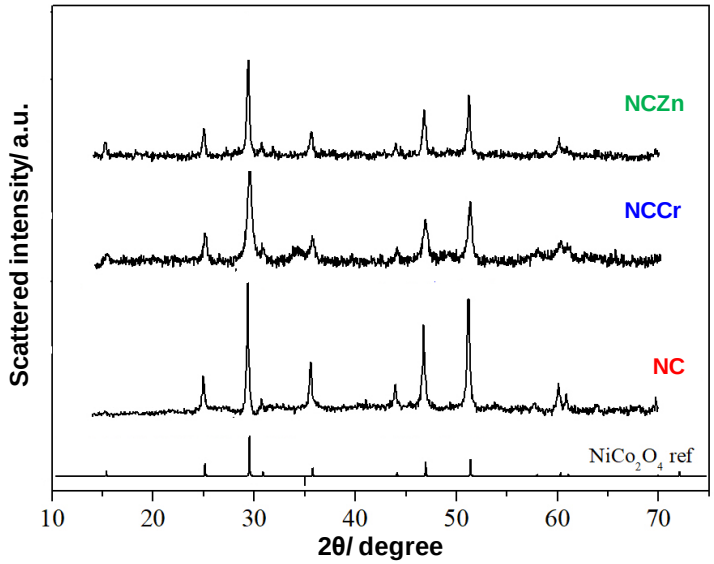

Figure 27. Diffraction patterns of the NC, NCCr and NCZn powders in comparison with the $NiCo_2O_4$ one derived from literature.

As explained in paragraph 3.2.4, the XRD characterization of cathodes extracted from cells that worked in various electrochemical conditions was only tentatively performed due to the possible arduous detection of lithium oxides deposits because of the effect of the used electrolyte solution (i.e. LiTFSI/TEGDME). As expected, the moderate low DNs of both the anion salt and the solvent prevented the growth of discharge products in large crystalline particles in almost all the experiments. Only for one electrode, made of NCCr@Ni and discharged to 2.0 V at the lowest current density of 0.025 mA cm^{-2} (i.e. the best performing cathode on one discharge/charge cycle, see Figure 23 a), the X-ray diffraction pattern shows additional reflections respect to those for the $NiCo_2O_4$, possibly related to Li_2O_2 (space group $P6_3/mmc$, JCPDS Card No. 73-1640) (Figure 28). The reference patterns for $NiCo_2O_4$ and Li_2O_2 and the experimental ones for a pristine NCCr@Ni electrode and for the same discharged to 2.0 V at the higher current density of 0.1 mA cm^{-2} are also shown.

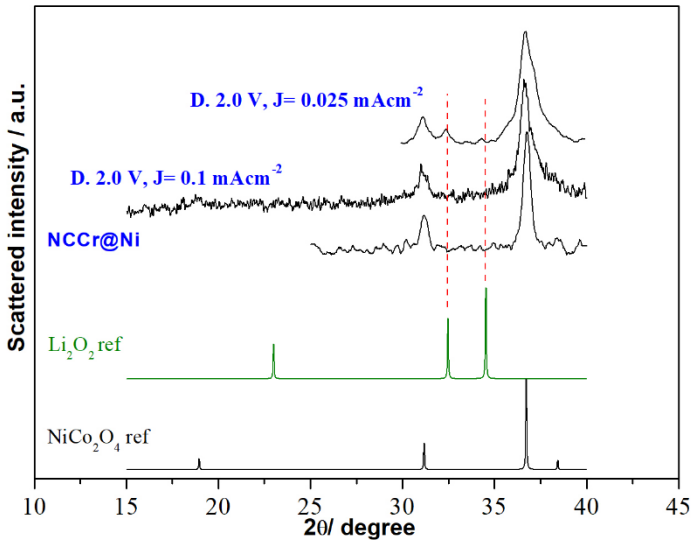

Figure 28. Diffraction patterns of NCCr@Ni electrodes discharged to 2.0 V at J = 0.1 mA cm^{-2} and J = 0.025 mA cm^{-2}. The XRD of a pristine NCCr@Ni cathode (experimental) and of $NiCo_2O_4$ and Li_2O_2 (references) are also shown.

5.4.2. SEM and EDS

A piece of Ni foam, pristine NC@Ni, NCCr@Ni and NCZn@Ni electrodes, their corresponding powders NC, NCCr and NCZn and a selection of significant cathodes extracted from Li-O_2 cells were observed at the Scanning Electron Microscope of the *Centro di Ricerca per le Nanotecnologie applicate all'Ingegneria della Sapienza* (CNIS).

After the synthesis, the Ni foam clean and smooth pores walls (Figure 29 a) are covered by aggregates of $NiCo_2O_4$ (Figure 29 b, effect shown for the NC@Ni material preparation). Nevertheless, the composed electrode maintains a relatively void structure and can ensure both good oxygen flow and accumulation of abundant amounts of discharge products when used as cathode for Li-O_2 cells.

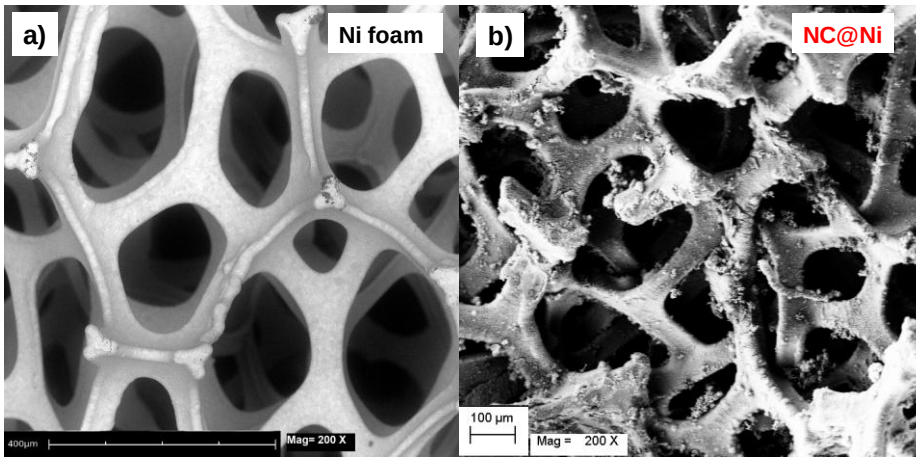

Figure 29. SEM micrographs at low magnification of (a) a clean piece of Ni foam and (b) a pristine NC@Ni cathode.

By means of XRD (see previous paragraph), we demonstrated that Cr(III) and Zn(II) doping leaves the $NiCo_2O_4$ spinel lattice unaltered. SEM observations also attest that dopants do not induce morphological changes in the cobaltite nanostructure. NC@Ni, NCCr@Ni and NCZn@Ni materials are constituted by porous nanowires of approximately 50–150 nm in diameter and 1–3 µm in length (Figure 30).

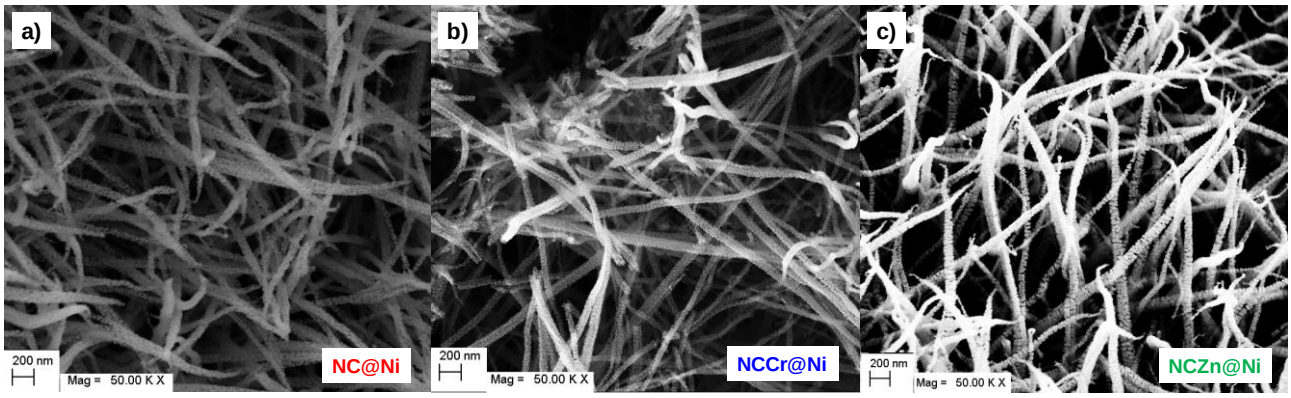

Figure 30. Comparison between morphologies by SEM of the (a) NC@Ni, (b) NCCr@Ni and (c) NCZn@Ni pristine electrodes addressed in this work.

EDS maps on selected areas of the doped samples (Figure 31) highlight the homogeneous distribution of chromium and zinc on the $NiCo_2O_4$ nanostructures and confirm their incorporation as dopants. Due to the unavoidable effect of the Ni foam support, it was not possible to calculate significant values for the Ni/Co atomic ratios by means of the EDS analysis.

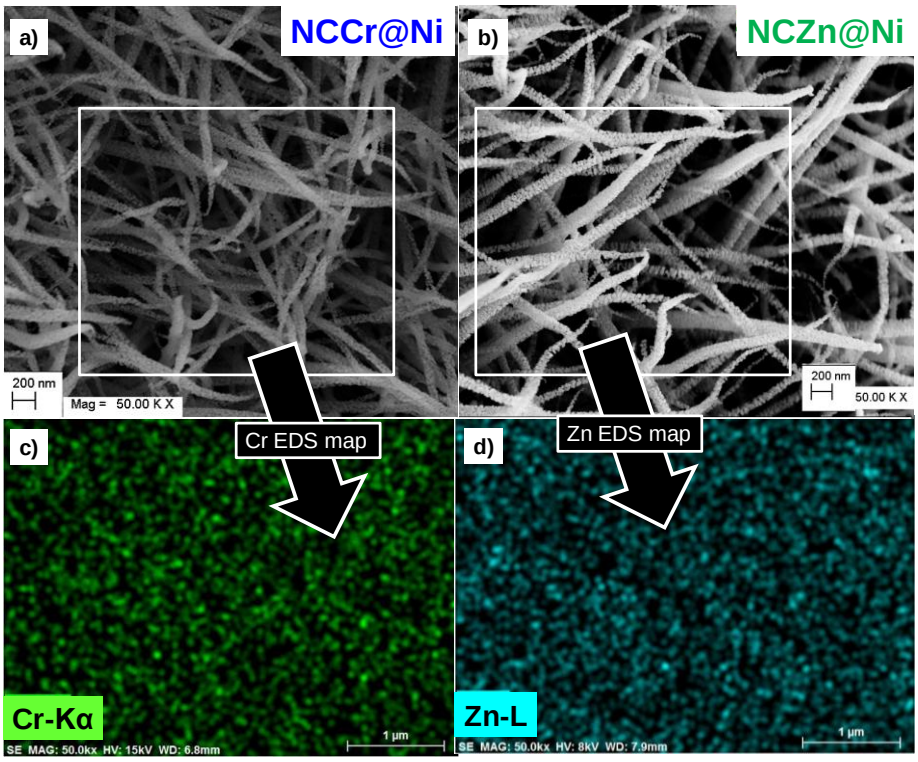

Figure 31. SEM micrographs of the (a) NCCr@Ni and (b) NCZn@Ni pristine electrodes; EDS maps of the (c) Cr-Kα and (d) Zn-L emissions from the areas highlighted in (a) and (b), respectively.

The comparison of the SEM micrographs of the pristine electrodes (Figure 30) with those of the corresponding powders (Figure 32), helps recognize the probable influence exerted by the Ni foam support on the $NiCo_2O_4$ crystal growth and morphology. In the case of the pure NC powder, we observe nanowires not vertically aligned as on the NC@Ni electrode (Figure 30 a), but circularly oriented in flower-like aggregates (Figure 32 a).

Interestingly, the iso-morphology of the pristine NC@Ni, NCCr@Ni and NCZn@Ni cathodes, is not replicated by their corresponding powders. In fact, the NCCr and NCZn samples appear much more disordered than the NC one, with no evidence of aggregates assuming particular shapes (Figure 32 b-c).

However, the nanowires of the doped samples (Figure 32 b-c) could have likely been more affected by mechanical operation due to the grinding of the powders when pasted onto the SEM stubs than the undoped one.

The amount of powders pasted onto the SEM stubs was not sufficiently high to derive significant values for the Ni/Co atomic ratios from the EDS analysis.

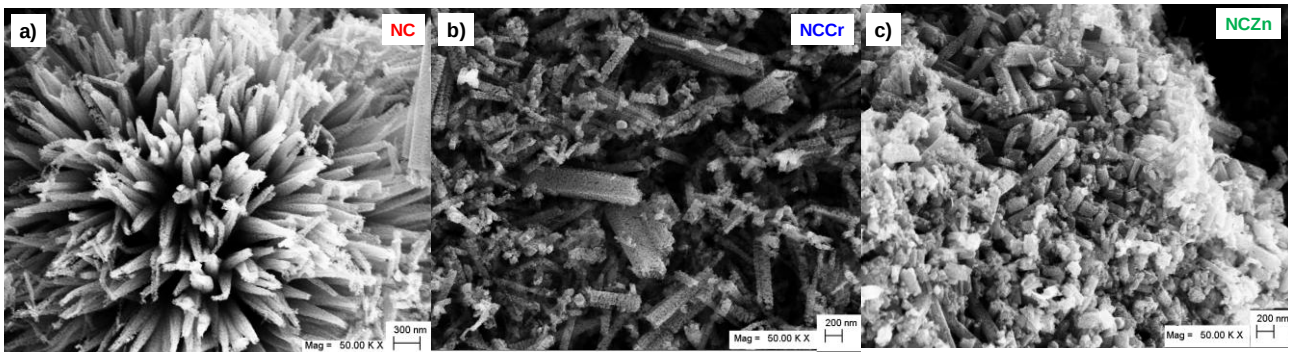

Figure 32. Comparison between morphologies by SEM of the (a) NC, (b) NCCr and (c) NCZn powders addressed in this work.

We obtained similar scanning electron micrographs for the NC@Ni, NCCr@Ni and NCZn@Ni cathodes discharged to 2.0 V at J = 0.025 mA cm^{-2}. We observed the growth of amorphous aggregates possibly constituted by organic degradation products from the TEGDME solvent, surrounding the $NiCo_2O_4$ nanowires and occluding their pores. Instead, the stability of the cathode material was confirmed, being its nanostructure nicely unaltered.

As discussed previously, due to the effect of the $TFSI^-$ and TEGDME moderately low DNs, we did not expect to observe lithium oxides particles. Surprisingly, on the Cr(III)-doped positive electrode, Li_2O_2 deposits were visible. Effectively, the higher discharge capacity registered for this sample respect to the others (see Figure 23 a) accounts for the possible growth of a major amount of ORR products. Moreover, the crystallinity of these deposits was confirmed by XRD measurement (see Figure 28). It is worth noting that, in contrast with literature, in our systems lithium peroxide particles grew on the $NiCo_2O_4$ nanowires vertically aligned on the Ni foam support assuming a flower-like shape (Figure 33 b).[69]

ORR products were not observed on the same cathode discharged to 2.0 V at the higher current density of J = 0.1 mA cm^{-2} (Figure 33 a), confirming the effect of decreasing current density on the lithium oxides growth mechanism and morphology.[23]

Upon charging the cell up to 4.1 V at J = 0.025 mA cm^{-2}, a complete reversibility was observed. In fact, the removal of both lithium oxides and degradation products led to the depletion of the $NiCo_2O_4$ pores and surface (Figure 33 c).

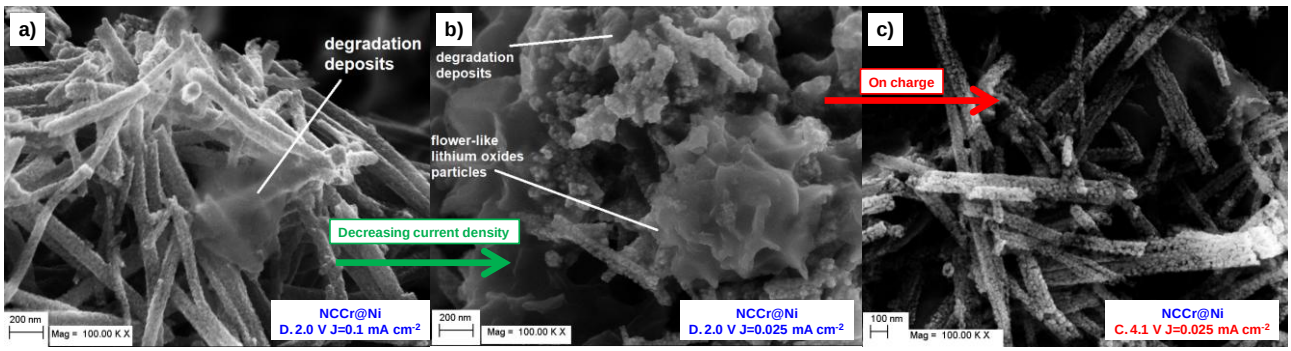

Figure 33. SEM images for NCCr@Ni electrodes (a) discharged to 2.0 V at high current density (i.e. 0.1 mA cm^{-2}); (b) discharged to 2.0 V at low current density (i.e. 0.025 mA cm^{-2}) and (c) cycled between 2.0 V and 4.1 V at J = 0.025 mA cm^{-2}.

In Figure 34, a comparison by means of SEM between the Zn(II) and the Cr(III)-doped electrodes extracted from cells cycled at J = 0.2 mA cm^{-2} with a capacity limitation of 0.1 mAh cm^{-2} (see long term performance in Figure 24 a) is reported. Both the materials show an almost totally unaltered nanostructure, being their nanowires slightly more disordered respect to those of the pristine electrodes (Figure 31). However, particularly in the case of the early died NCZn@Ni cathode, upon cycling we observe loss of reversibility in terms of degradations by-products removal (Figure 34 b). This evidence supports the idea about the relation between the cells death and the deactivation of the $NiCo_2O_4$ electrocatalyst due to the occlusion of its surface and pores by insulating organic compounds derived from TEGDME oxidative decomposition.

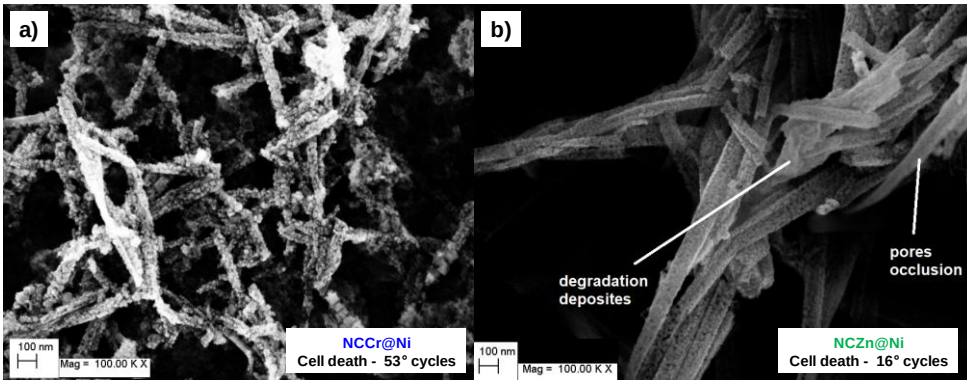

Figure 34. SEM images for (a) NCCr@Ni and (b) NCZn@Ni electrodes cycled at J = 0.2 mA cm^{-2} with a capacity limitation of 0.1 mAh cm^{-2} until the cells death.

5.4.3. TEM

The nanostructures of the NC@Ni, NCCr@Ni and NCZn@Ni samples were further investigated by means of TEM (Figure 35).

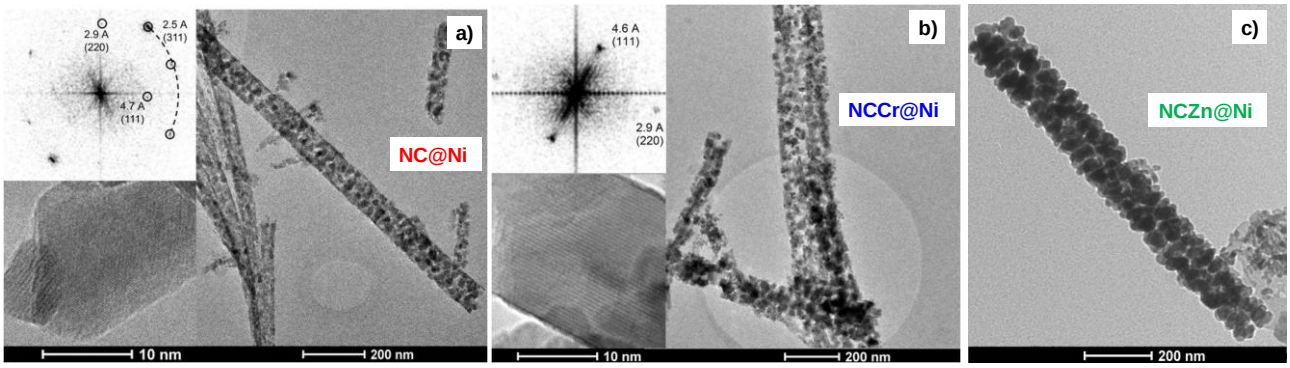

Figure 35. Comparison between the morphologies by TEM of materials from the (a) NC@Ni, (b) NCCr@Ni and (c) NCZn@Ni pristine electrodes. In the insets of Figure 35 a-b TEM magnifications, the corresponding FFT simulated diffraction patterns and some characteristic interplanar distances are shown.

In agreement with XRD and SEM observations, the absence of structural and morphological difference between the pure, the Cr(III) and Zn(II)-doped materials was confirmed. As expected,[42,50] all the samples are constituted by nanowires formed by highly crystalline cubic particles with linear size in the 20-30 nm range. By means of FFT performed on high magnification images (see the simulated electron diffraction patterns for NC@Ni and NCCr@Ni in the insets of Figure 35 a and b, respectively), we observed some families of crystal planes of the samples and measured their characteristic interplanar distances.

5.4.4. XPS

The surface composition of the pristine NC@Ni, NCCr@Ni and NCZn@Ni electrodes and the corresponding NC, NCCr, and NCZn powders was investigated by means of XPS. In chapter 3, paragraph 3.2.5, XPS experimental details have been described. In the case of the powders analysis, an adequate amount of material was dispersed on a conductive scotch prior to the attachment on the instrument sample holder. The C 1s binding energy (BE) of the $–CH_2–$ groups at 284.8 eV belonging to the aliphatic carbon contamination on the cathodes surface was used as an internal standard reference for the BE scale (accuracy of ±0.05 eV).

Wide XP spectra and core photoemission regions for the pristine electrodes

From the **wide XP spectra** for the NC@Ni, NCCr@Ni and NCZn@Ni pristine cathodes shown in Figure 36 we derived information about the elemental composition at their surface. The characteristic photoemission peaks and Auger signals[99] of the main elements (i.e. Ni, Co and O) constituting the analyzed samples are indicated by arrows. Additional peaks are also observed in all the spectra due to aliphatic carbon contamination (C 1s) and residual chlorides from the synthesis (Cl 2p signal at about 200 eV). Instead, the absence of signals in the N 1s region suggests that nitrates were totally removed after the hydrothermal treatment by means of the washing procedure and/or during calcination.

As regards the Cr(III) and the Zn(II) –doped pristine electrodes, no sensible differences are visible in their spectra (Figure 36 b-c) respect to the pure material (Figure 36 a), except for the presence of the characteristic peaks of the dopants (i.e. Cr 2p and Zn 2p and 3p, respectively).

Overall, XPS confirmed the synthesis of nickel cobaltite-based electrodes and, in the case of the doped samples, the incorporation of chromium and zinc in the $NiCo_2O_4$ spinel lattice.

In order to perform a deep investigation of the composition of the samples, exploring both the transition metal oxides states of oxidation and their relative amounts at the surface, we acquired the core photoemission regions of Ni, Co, Cr and Zn in detail. It is worth noting that, the evaluation of the state of charge of both Ni and Co (i.e. the presence of Ni^{2+} and/or Ni^{3+} and that of Co^{2+} and/or Co^{3+}, respectively) by means of the analysis of their Auger peaks was not attempted because of the low signal-to-noise ratio due to the relatively low amount of $NiCo_2O_4$ grown on the Ni foam.

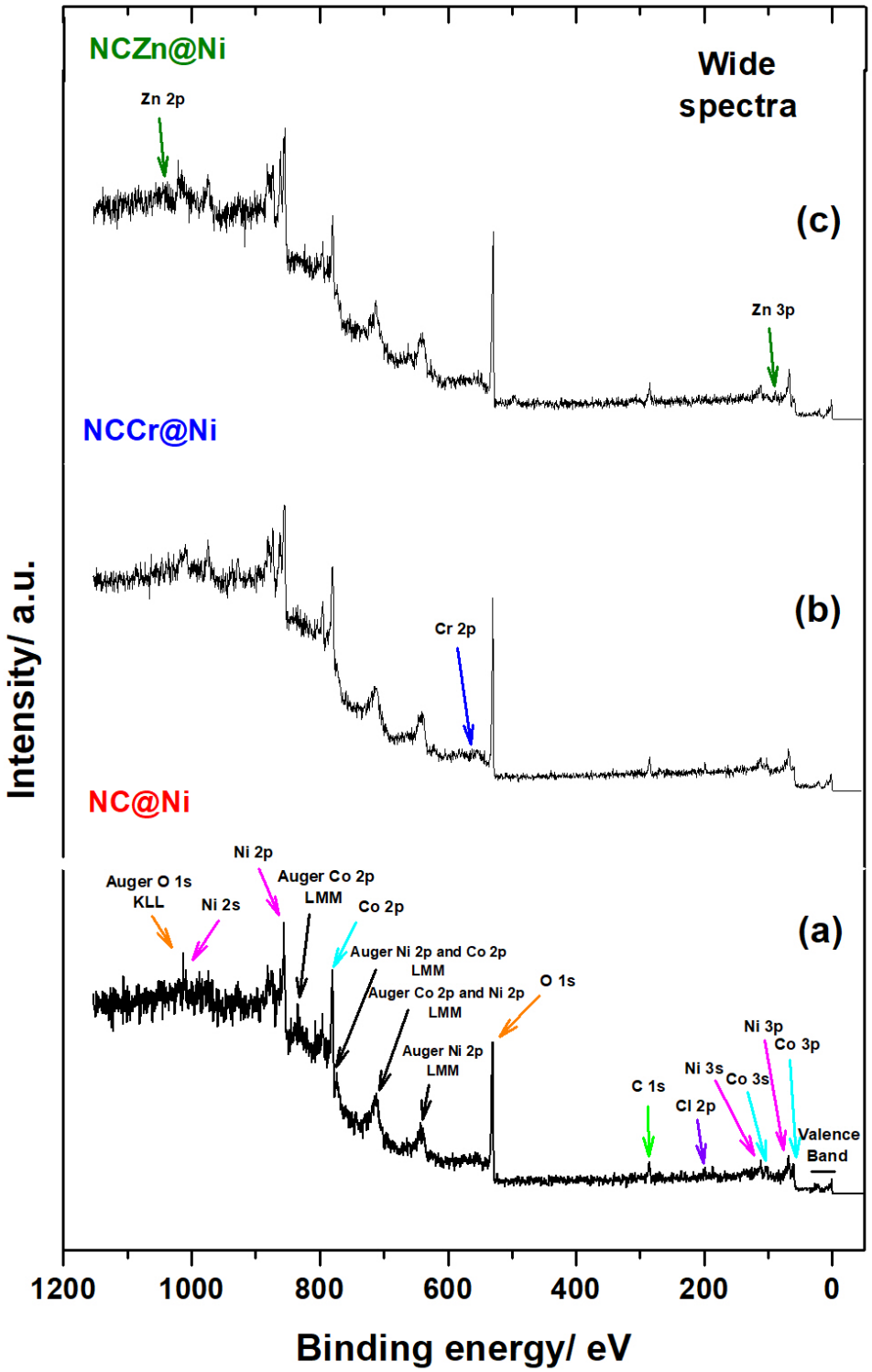

Figure 36. Wide XP spectra for the (a) NC@Ni, (b) NCCr@Ni and (c) NCZn@Ni pristine electrodes addressed in this work. Peaks observed for all the three samples are marked in spectrum (a). Characteristic signals for Cr and Zn are marked in the spectra (b) and (c), respectively.

The **C 1s regions** of the XP spectra for the NC@Ni, NCCr@Ni and NCZn@Ni materials are shown in Figure 37. According to reports on the XPS characterization of NiO samples,[130,131] the BE of the first peak belonging to the $–CH_2–$ groups of the unavoidable aliphatic carbon contamination was reported at 284.8 eV and, as stated previously, was used as an internal standard reference for the BE scale. In all the spectra, a second peak was visible for oxidized functions (i.e. C-O, C-O-C etc.) at the carbon surface (286.3-286.4 eV).[99] A faint third signal at 288.8 eV, related to higher oxidized carbonaceous groups possibly grown due to the X-ray exposition,[99] was observed only for the pure material (spectrum a).

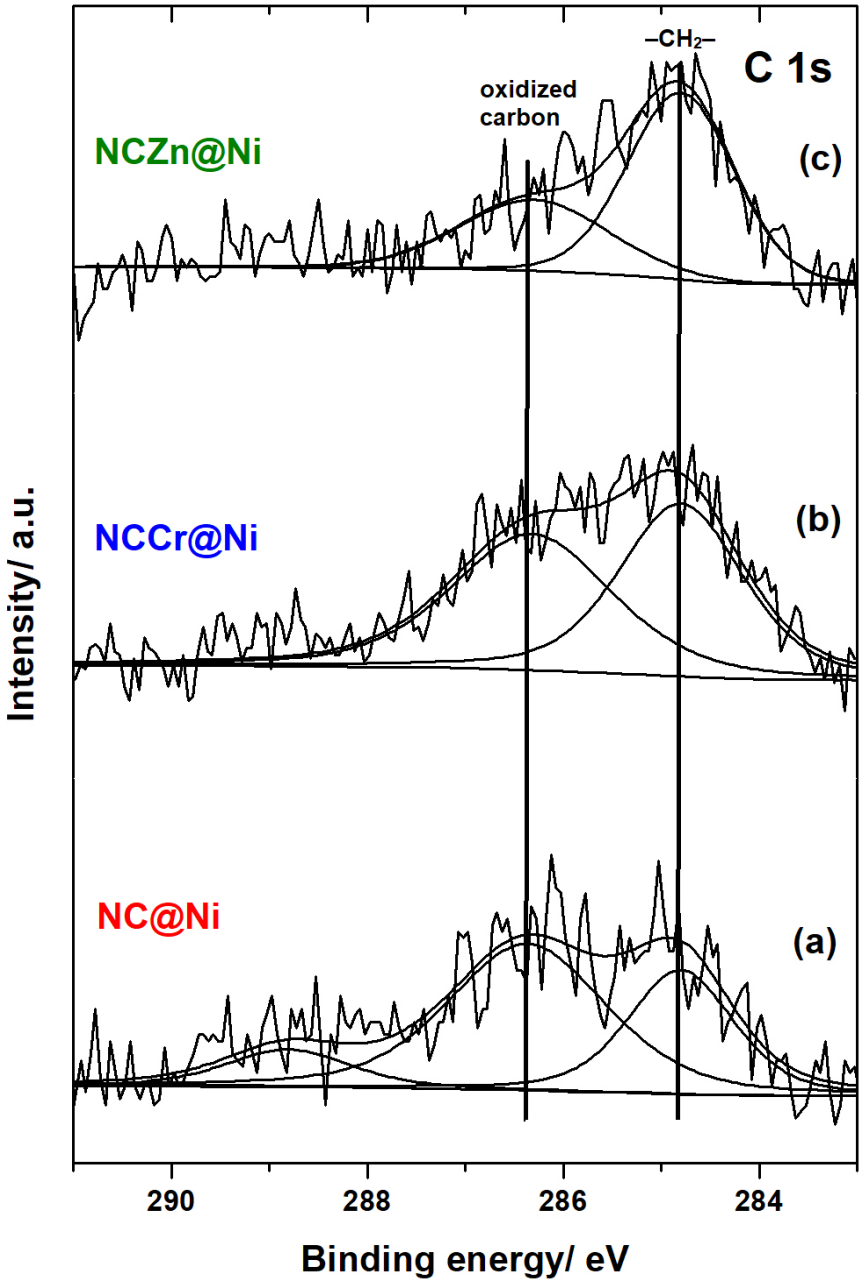

Figure 37. C 1s XP spectra for the (a) NC@Ni, (b) NCCr@Ni and (c) NCZn@Ni pristine electrodes addressed in this work.

Due to the low S/N ratio affecting both the Ni $2p_{3/2}$ and Co $2p_{3/2}$ XP spectra of the samples (Figures 38 and 39, respectively), no attempts were given to their reconstruction by means of a curve fitting procedure. Moreover, the effect of the Ni foam support hampered the relative quantification of Ni and Co of the $NiCo_2O_4$ deposit. However, some interesting information were derived from the analysis of the overall experimental profiles.

For all the materials, the **Ni $2p_{3/2}$ signal** shape (Figure 38) is fully compatible with already reported data on cobaltite-type compounds.[59,108,132] However, in the spectra b and c for the doped samples, we observe a decrease of the shoulder at about 856 eV (cyan dashed line) respect to the first peak located around 854 eV (pink dashed line). In NiO this feature has been widely accepted to be related to the d^8:$\underline{c}d^9\underline{L}$ final ionized states of Ni(II) sites[133,134] whereas, in spinel phases, its attribution to Ni(III) centers has been proposed by many authors.[58,59,108] Thus, our experimental evidence suggested an altered surface composition on the doped cobaltite surface respect to the pure material with a reduced concentration of Ni(III) centers induced by the creation of Cr(III) or Zn(II) sites.

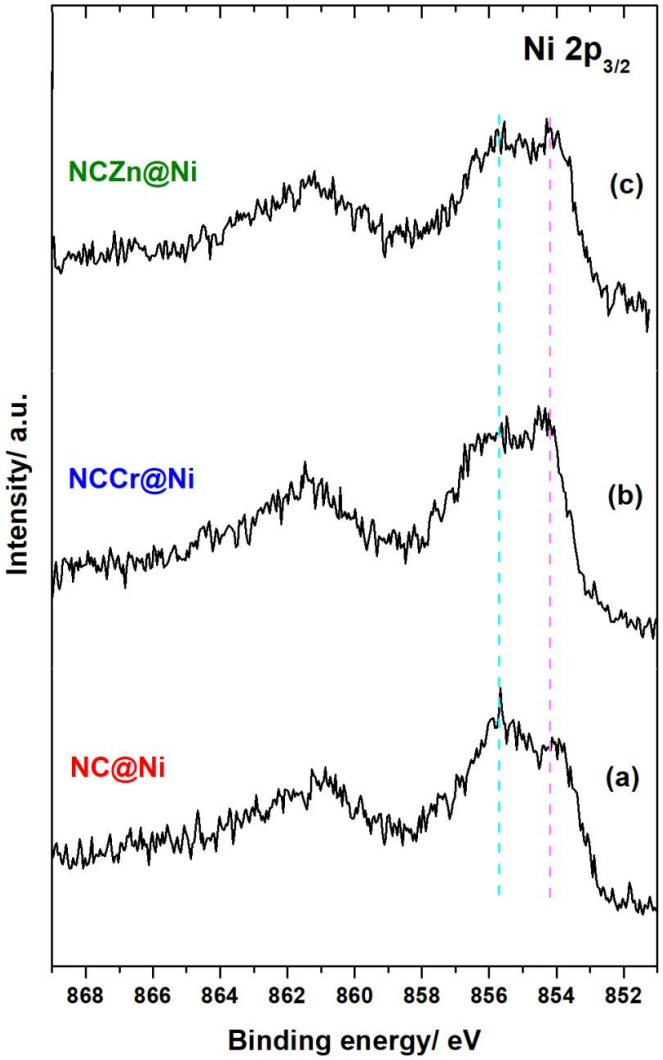

Figure 38. Ni $2p_{3/2}$ XP spectra for the (a) NC@Ni, (b) NCCr@Ni and (c) NCZn@Ni pristine electrodes addressed in this work. The intensity trends of the first peak and its shoulder at high BE are marked with pink and cyan dashed lines, respectively.

A similar picture was observed in the **Co $2p_{3/2}$ photoionization regions** (Figure 39), where the absolute positions of the broad signals are analogue to those for mixed-valence cobalt oxides (i.e. Co_3O_4 samples) and in good agreement with already reported data on cobaltite-type compounds.[59,108,132,135]

The broad feature at about 780 eV suggested the co-presence of Co(III) and Co(II) ions in the $NiCo_2O_4$ lattice. Moreover, the very low intensity of the shake-up signal in the region 783–787 eV call for the presence of Co(II) predominantly in tetrahedral sites.[59,108,132]

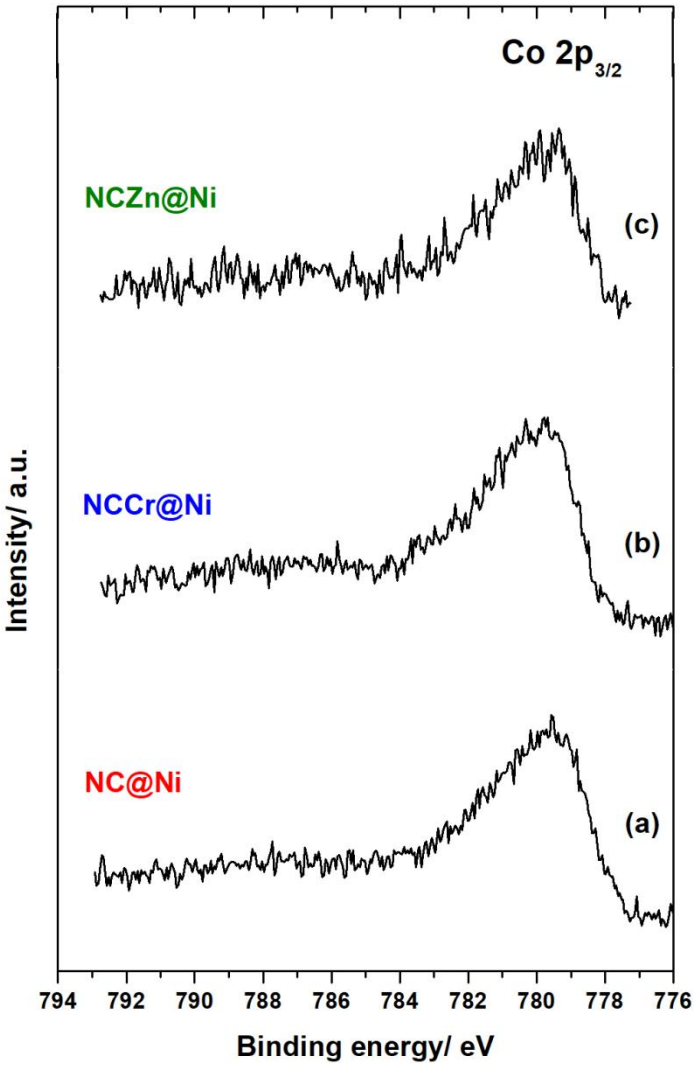

Figure 39. Co $2p_{3/2}$ XP spectra of the (a) NC@Ni, (b) NCCr@Ni and (c) NCZn@Ni pristine electrodes addressed in this work.

The **Cr 2p and Zn 2p photoemission regions** are reported in Figure 40 for the NCCr@Ni and NCZn@Ni pristine electrodes, respectively.

In the Cr 2p region (Figure 40 a), the position (575–579 eV for the $2p_{3/2}$ peak) of the two spin-orbit components, broadened due to multiplet splitting, confirmed the incorporation of Cr(III) within the spinel lattice.[135]

The Zn 2p region (Figure 40 b) shows two spin-orbit split components (the $2p_{3/2}$ peak at ca. 1021 eV) separated by ca. 23 eV, in agreement with the insertion of Zn(II) in an oxide-type environment.[99]

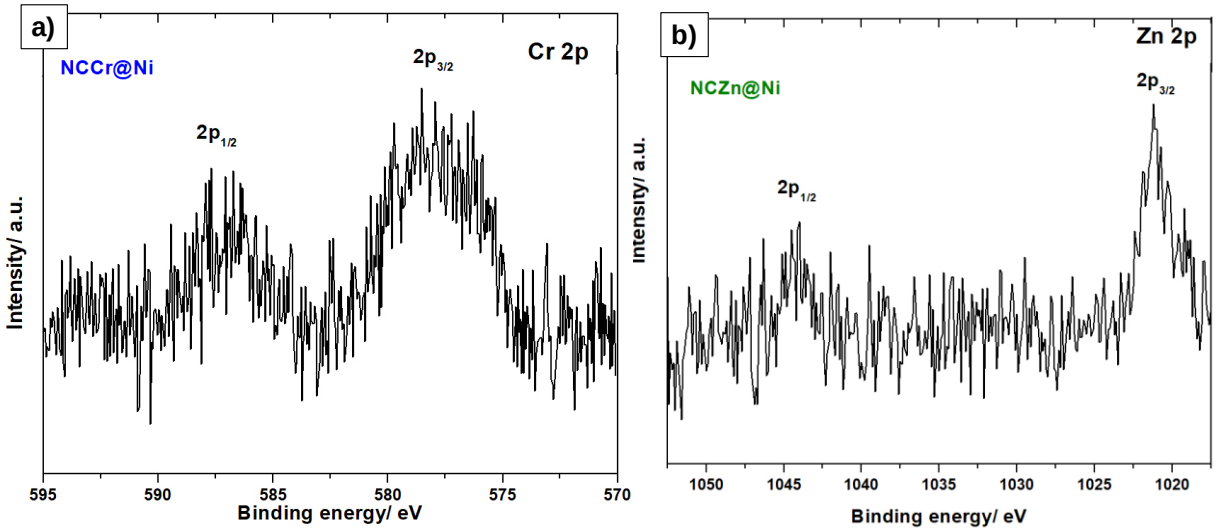

Figure 40. (a) Cr 2p XP region for the NCCr@Ni sample and (b) Zn 2p XP region for the NCZn@Ni sample.

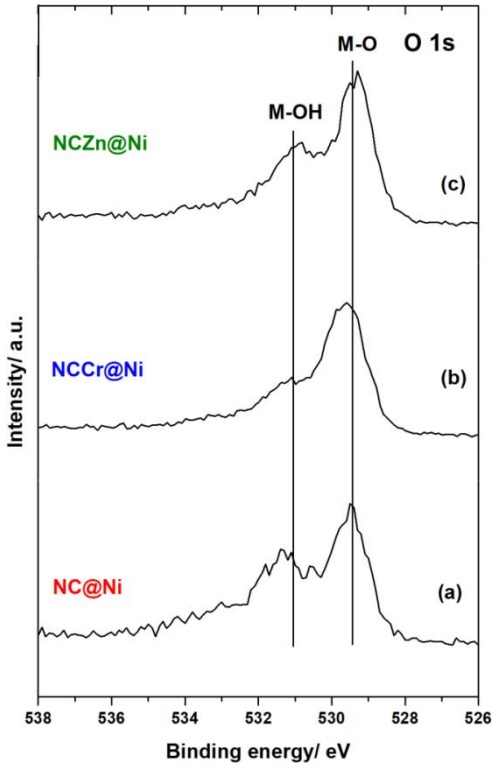

Figure 41. O 1s XP spectra for the (a) NC@Ni, (b) NCCr@Ni and (c) NCZn@Ni pristine electrodes addressed in this work.

For completeness, although their interpretations are arduous when acquired for mixed metal oxides samples, **the O 1s photoemission regions** are reported in Figure 41. For all the materials, an intense first peak at about 529.5 eV was related to the various metal-oxygen (M-O) bonds in the bulk of the cobaltite spinel

lattice,[136] while a second broad signal at about 531 eV accounted for the presence of chemisorbed hydroxides species (i.e. M-OH bonds), which form spontaneously on the surface of the samples upon exposition to air.[137,138]

Significant core photoemission regions for the powders

The **wide XP spectra** and the **C 1s, O 1s, Cr 2p and Zn 2p photoemission regions** acquired for the NC, NCCr and NCZn powders (data not shown) did not show significant difference from those for the corresponding cobaltite-based materials on Ni foam. Also for these samples, the BE of the first peak in the C 1s regions, belonging to the $–CH_2–$ groups of the aliphatic carbon contamination, was reported at 284.8 eV and, as stated previously, was used as an internal standard reference for the BE scale.

The absence of the spectral contributions from the Ni foam allowed to full reconstruct the Ni $2p_{3/2}$ and the Co $2p_{3/2}$ photoemission regions by means of a curve fitting procedure and to perform the relative quantification of nickel and cobalt.

The **Ni $2p_{3/2}$ photoionization regions** (Figure 42) were theoretically reconstructed using six peaks. Their absolute positions and their relative distances were in agreement to those reported for NiO samples.[130,131,139] These parameters and the attributions of the signals to different final ionized states of Ni(II) centers are reported in Table 6.

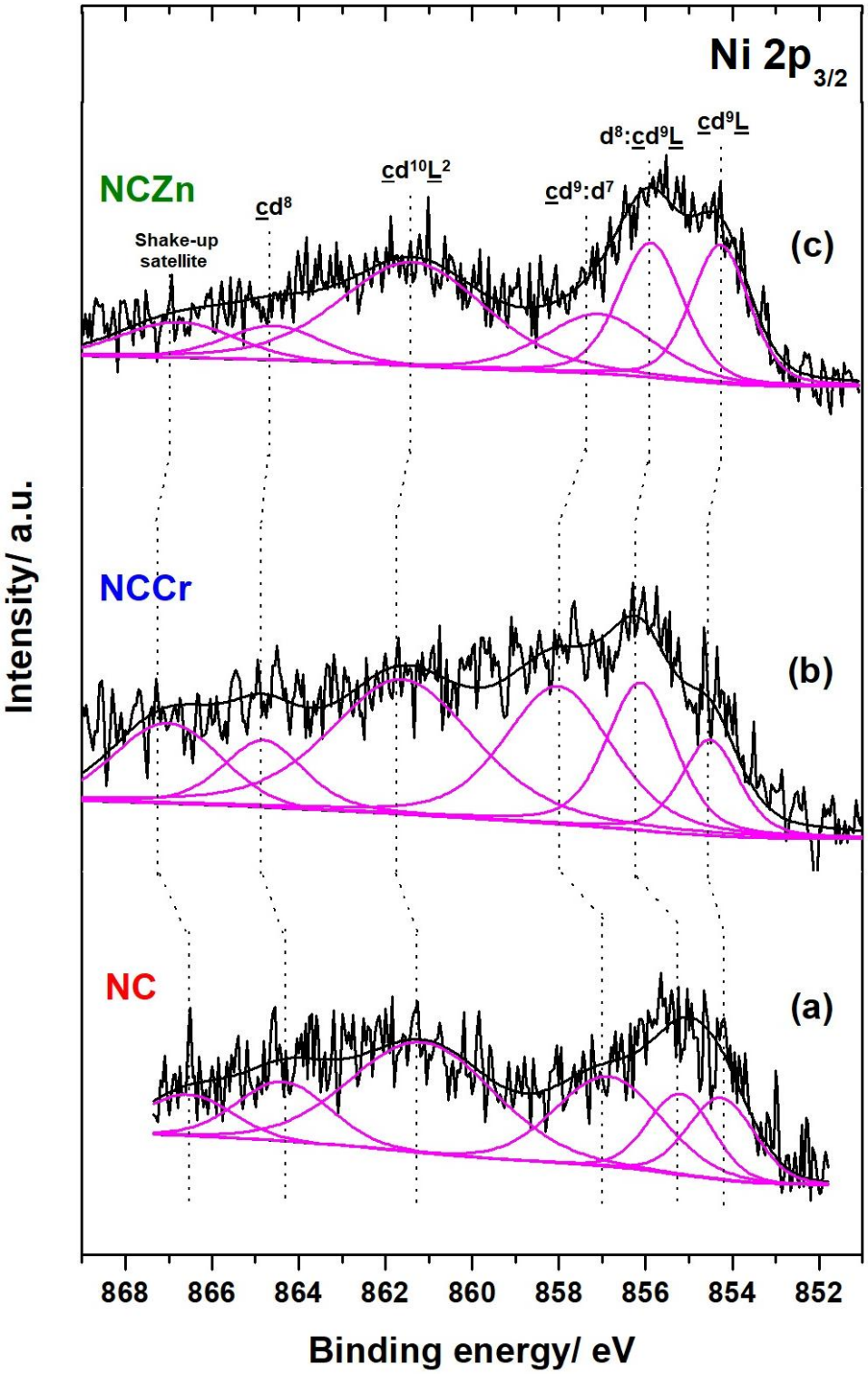

Figure 42. Ni $2p_{3/2}$ XP spectra of the (a) NC, (b) NCCr and (c) NCZn powders reconstructed by means of a curve fitting procedure. The signals are related to different final ionized states of Ni(II) centers and their shifts are indicated with dotted lines.

Sample	BE position (eV)	Assignments
NC	854.2	$\underline{c}d^9\underline{L}$
	856.2	d^8:$\underline{c}d^9\underline{L}$
	857.9	$\underline{c}d^9$:d^7 non-local screening
	861.2	$\underline{c}d^{10}\underline{L}^2$
	864.4	$\underline{c}d^8$
	866.6	shake-up satellite
NCCr	854.5	$\underline{c}d^9\underline{L}$
	856.1	d^8:$\underline{c}d^9\underline{L}$
	858.0	$\underline{c}d^9$:d^7 non-local screening
	861.6	$\underline{c}d^{10}\underline{L}^2$
	864.8	$\underline{c}d^8$
	867.0	shake-up satellite
NCZn	854.3	$\underline{c}d^9\underline{L}$
	855.9	d^8:$\underline{c}d^9\underline{L}$
	857.1	$\underline{c}d^9$:d^7 non-local screening
	861.4	$\underline{c}d^{10}\underline{L}^2$
	864.6	$\underline{c}d^8$
	866.8	shake-up satellite

Table 6. BE position and assignments for the peaks determined after curve fitting of the experimental Ni $2p_{3/2}$ spectra for the NC, NCCr and NCZn powders.

The **Co $2p_{3/2}$ photoionization regions** (Figure 43) were theoretically reconstructed using five peaks. Their absolute positions and their relative distances were in good agreement to those reported for Co_3O_4 and $NiCo_2O_4$ samples.[59,108,132,135] These parameters and the attributions of the signals to different final ionized states of Co(II) and Co(III) centers are reported in Table 7. Therefore, the co-presence of Co(II) and Co(III) ions in the $NiCo_2O_4$ spinel lattice was confirmed both in the case of the pure and the doped samples. Moreover, as observed in the case of the electrodes, the low intensity of the peak located in the range 785.0-785.5 eV, related to a shake-up satellite of Co(II) sites, was compatible with a Co(II) predominance in tetrahedral sites.[132]

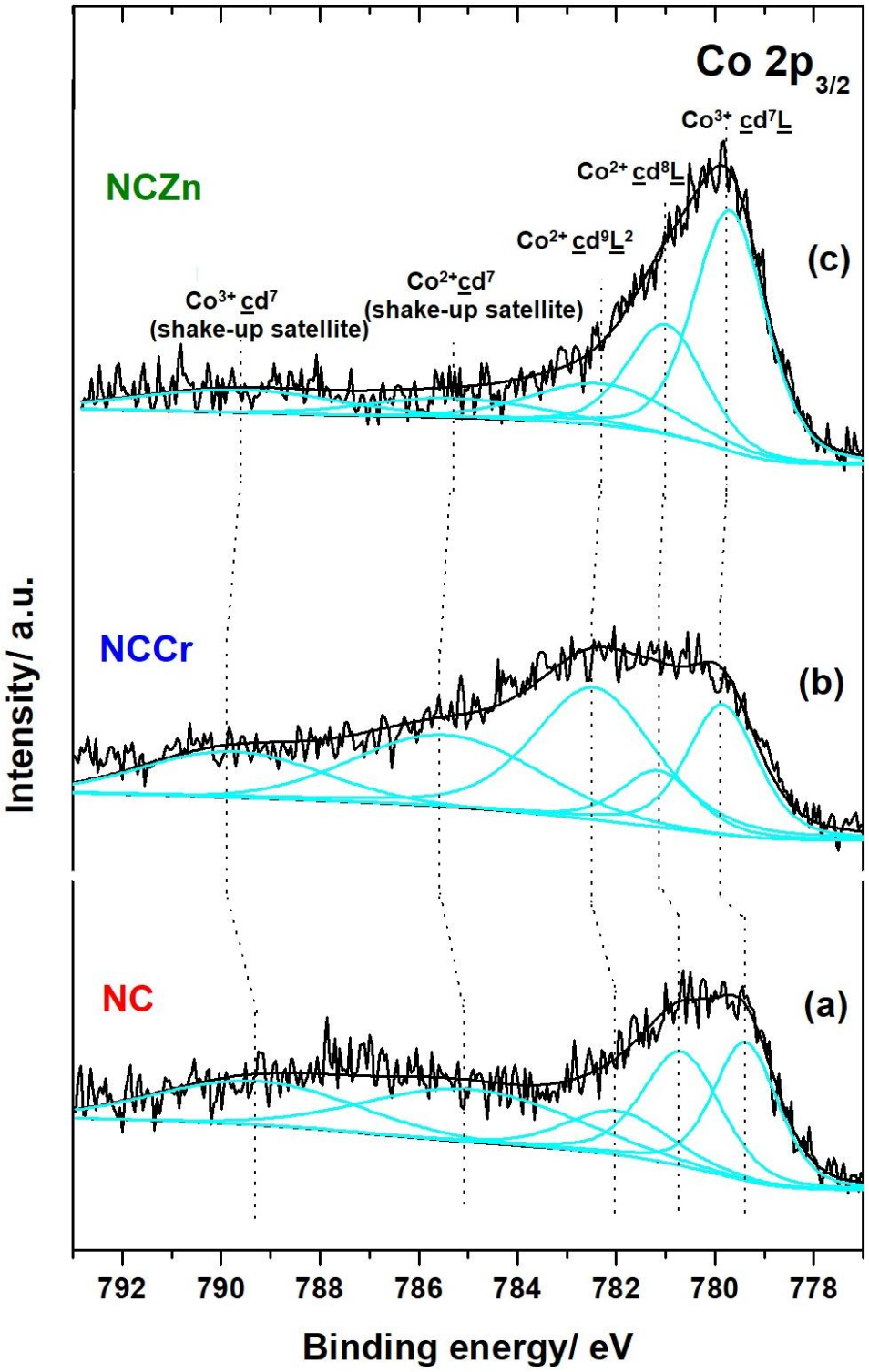

Figure 43. Co $2p_{3/2}$ XP spectra of the (a) NC, (b) NCCr and (c) NCZn powders reconstructed by means of a curve fitting procedure. The signals are related to different final ionized states of Co(II) and Co(III) centers and their shifts are indicated with dotted lines.

Sample	BE position (eV)	Assignments
NC	779.4	Co^{3+} $\underline{c}d^7\underline{L}$
	780.7	Co^{2+} $\underline{c}d^8\underline{L}$
	782.0	Co^{2+} $\underline{c}d^9\underline{L}^2$
	785.0	Co^{2+} $\underline{c}d^7$ (shake-up satellite)
	789.3	Co^{3+} $\underline{c}d^7$ (shake-up satellite)
NCCr	779.9	Co^{3+} $\underline{c}d^7\underline{L}$
	781.2	Co^{2+} $\underline{c}d^8\underline{L}$
	782.5	Co^{2+} $\underline{c}d^9\underline{L}^2$
	785.5	Co^{2+} $\underline{c}d^7$ (shake-up satellite)
	789.8	Co^{3+} $\underline{c}d^7$ (shake-up satellite)
NCZn	779.7	Co^{3+} $\underline{c}d^7\underline{L}$
	781.0	Co^{2+} $\underline{c}d^8\underline{L}$
	782.3	Co^{2+} $\underline{c}d^9\underline{L}^2$
	785.3	Co^{2+} $\underline{c}d^7$ (shake-up satellite)
	789.6	Co^{3+} $\underline{c}d^7$ (shake-up satellite)

Table 7. BE position and assignments for the peaks determined after curve fitting of the experimental Co $2p_{3/2}$ spectra of the NC, NCCr and NCZn powders.

Although moving from the pure (Figures 42 a and 43 a) to the doped samples (Figures 42 b,c and 43 b,c), we observed a retention of the number and relative distances of the peaks, particularly in the case of the chromium doping, a moderate shift (i.e. minimum shift 0.1 eV, maximum shift 0.5 eV) towards the high B.E was registered. As discussed in chapter 6, a similar picture was observed in the XP spectra registered by means of synchrotron radiation both for the pristine electrodes and their corresponding powders. This observation suggested a moderate alteration of the $NiCo_2O_4$ electronic structure due to doping with possible influence on its activity as ORR/OER electrocatalyst. However, a deeper investigation on this effect requires theoretical and/or experimental studies by means of other techniques (e.g. magnetic and spin properties measurements) both going beyond the PhD activity described in this work.

Instead, by means of the calculation of the Co/Ni atomic ratios reported in Table 8, we confirmed our hypothesis (see paragraph 5.3.3) about an alteration of the $NiCo_2O_4$ surface composition due to doping. In fact, both Cr(III) and Zn(II) insertion in the cobaltite lattice decreased the Ni sites concentration at the surface. As discussed in chapter 6, similar calculation were performed on the XP synchrotron spectra of the powders. In these cases, the high instrumental resolution and sensitivity enabled to demonstrate that dopants substituted not only Ni(III) and Ni(II) but also Co(II) ions at the materials surface. As proposed in paragraph 5.3.3, this alteration of the NCCr@Ni and NCZn@Ni electrodes surface chemistry respect to the pure NC@Ni one could lead to the enhancement of the ORR kinetics, observed by means of the registration of

pseudo-Tafel plots, due to a possible modification in the O_2 and LiO_2 adsorption kinetics and an increase of the concentration of these compounds as reagents on the surface.

Sample	Co/Ni atomic ratio
NC	1.42
NCCr	1.01
NCZn	0.87

Table 8. Co/Ni atomic ratios calculated for the NC, NCCr and NCZn powders referring to their laboratory XP spectra. A decrease of the Ni concentration at the surface due to doping was registered.

5.5. Conclusions and open questions

Novel M^{n+}-doped (M^{n+}=Cr^{3+} and Zn^{2+}) $NiCo_2O_4$ nanomaterials grown on Ni foam (NCCr@Ni and NCZn@Ni) were successfully synthesized by a hydrothermal route. These porous carbon-free composite electrodes, inert to oxidative chemical attacks, were tested as cathodes for Li-O_2 cells. Compared to the pure NC@Ni material, the doped ones showed a remarkable enhancement of the electrochemical activity in terms of larger discharge capacity, lower discharge/charge overvoltages and prolonged cycle life. So, for the first time in the literature, the beneficial effect of the Cr(III) and Zn(II) doping of the $NiCo_2O_4$ spinel to increase its electrocatalytic activity towards both the ORR and the OER was demonstrated.

A deep chemical characterization by means of a multi-technique approach was performed both on the pristine electrodes and their corresponding unsupported powders (NC, NCCr and NCZn). The incorporation of chromium and zinc as dopants was confirmed by means of EDS maps and XPS analysis. The retentions of the crystallographic structure and the morphology for the doped materials respect to the pure one were demonstrated by XRD measurements and SEM/TEM observations, respectively.

XPS results revealed a change in the $NiCo_2O_4$ chemical surface composition due to doping, with a decrease in the Ni(III)/Ni(II) centers concentration. This observation supported the idea of a possible relationship between the alteration of the electrocatalyst surface composition and the O_2 and LiO_2 adsorption kinetics, leading to boosted kinetics for the cell reactions, particularly for the ORR, as revealed by pseudo-Tafel plots.

However, this in-house study on the cobaltite-based materials was not conclusive. Particularly, a full reconstruction of the XP spectra of the pristine electrodes was not attempted preventing their plain comparison with those of the corresponding powders. So, we decided to perform further XPS measurements by means of synchrotron radiation. Moreover, in conditions of enhanced resolving power and sensitivity, we could attempt a post-mortem characterization of selected cathodes with the aims of confirming the reversible formation of lithium oxides on these materials and gaining information about the reason for the cells death.

CHAPTER 6

XPS study on cobaltite-based samples by means of synchrotron radiation

6.1. Aims

Novel Cr(III) and Zn(II) –doped $NiCo_2O_4$ on Ni foam materials (NCCr@Ni and NCZn@Ni, respectively) were synthesized in our laboratory by means of a hydrothermal method and tested as cathodes for Li-O_2 cells. These materials showed a remarkable enhancement of the electrocatalytic activity respect to pure $NiCo_2O_4$ on Ni foam (NC@Ni). Despite of this, all these samples had analogous structure and nano-morphology. Some experimental evidences suggested a relationship between the boost of the nickel cobaltite electrochemical performance by means of doping and modifications in the surface composition in terms of amount and nature of transition metal ions sites (see previous chapter). However, a full characterization of these materials was not obtained by means of laboratory XPS measurements due to the impossibility of reconstruction of their Ni 2p and Co 2p photoemission regions affected by low S/N ratio and a considerable contribution from the Ni substrate.

In order to complete the investigation on these samples, we decided to perform other XPS analysis with synchrotron radiation in conditions of enhanced resolution power and sensitivity.

Our proposal with the title "Investigation on the surface reactivity of M^{n+}-doped $NiCo_2O_4$@Ni (M^{n+}= Cr^{3+}, Zn^{2+}) foam cathodes in a Li-O_2 cell" was accepted at the Elettra Materials Science beamline, where we performed measurements shifts from November, 27 to December, 2 2017.

Details about the beamline structure and operation features have been reported in chapter 3, paragraph 3.2.6.

In our laboratory, adopting a source of Al Kα photons, we did not analyze post-mortem cathodes extracted from cells due to the intrinsic low cross-section in photoemission regions such as Li 1s. Instead, we decided to investigate also a selection of these samples at Elettra. In fact, the high photon flux and unique beam monochromatization/collimation coupled to the wide tunability of the photon energy at Materials Science makes it possible to achieve very high resolution and excellent S/N ratio especially over the ionization regions below 200 eV. Analyzing Li 1s and C 1s spectral regions of discharged and charged cathodes, we aimed to confirm the reversible formation of lithium oxides and the relationship between the cell death and

the deactivation of the $NiCo_2O_4$ electrocatalyst due to the growth of degradation compounds from the organic solvent TEGDME on its surface and pores.

6.2. Summary of the samples and experimental details

The samples measured at Materials Science are summarized in Table 9. Post-mortem cathodes were recuperated from Li-O_2 cells whose electrochemical performance were analogous to those reported in chapter 5, paragraphs 5.3.1 and 5.3.2.

Material	Sample	Electrochemical procedure
NC@Ni	Pristine	--
	D. 2.0 V	Discharge to 2.0 V J = 0.025 mA cm^{-2}
	C. 4.1 V	Discharge to 2.0 V Charge to 4.1V J = 0.025 mA cm^{-2}
NCCr@Ni	Pristine	--
	D. 2.0 V	Discharge to 2.0 V J = 0.025 mA cm^{-2}
	C. 4.1 V	Discharge to 2.0 V Charge to 4.1V J = 0.025 mA cm^{-2}
	Cell death	Cycling at J = 0.2 mA cm^{-2} Capacity limit at 0.1 mAh cm^{-2}
NCZn@Ni	Pristine	--
	D. 2.0 V	Discharge to 2.0 V J = 0.025 mA cm^{-2}
	C. 4.1 V	Discharge to 2.0 V Charge to 4.1V J = 0.025 mA cm^{-2}
	Cell death	Cycling at J = 0.2 mA cm^{-2} Capacity limit at 0.1 mAh cm^{-2}
NC	Powders	
NCCr		
NCZn		

Table 9. Summary of the samples measured at the Materials Science beamline of the Elettra synchrotron by means of XPS.

All the samples were transferred to Materials Science sealed in vials in order to avoid contact with air before measurements.

The structure of the beamline end-station spectrometer was similar to that of our laboratory instrument (see Figures 6 a and 7 a), allowing all the samples to be transferred into the fast-entry chamber through an argon-filled glove-bag to avoid contact with air (see Figure 6 b). Pieces of the electrodes were attached on the instrument sample holder by means of a conductive scotch. As to the powders, an aliquot of material was dispersed onto the scotch and inserted in the fast-entry chamber without any further manipulation.

KolXPD was the software adopted for the data collecting and curve fitting. The photon energy calibration was performed by acquiring spectra of the Au 4f line from cleaned gold surfaces. Details on the curve fitting procedure have been reported in chapter 3, paragraph 3.2.6.

6.3. Results

6.3.1. Pristine electrodes

C 1s, Ni 2p and Co 2p photoemission regions were acquired for the pristine NC@Ni, NCCr@Ni and NCZn@Ni cathodes. The Cr 2p and Zn 2p regions were not acquired due to the still too low intensity of the former signal and the too high BE (>1000 eV) of the latter orbital with respect to the photon energy upper limit at Materials Science. On the other hand, our laboratory XPS measurements had already confirmed the incorporation of the Cr(III) and Zn (II) ions in the $NiCo_2O_4$ spinel lattice (see chapter 5).

The number and the relative positions of the peaks in the **C 1s spectra** (data not shown) were the same of those recorded for these samples in our laboratory (see Figure 37). Also for the synchrotron data processing, the position of the aliphatic carbon contamination at 284.8 eV was chosen as an internal standard reference for the BE scale.

The **Ni $2p_{3/2}$ photoemission regions** (Figure 44) were theoretically reconstructed using six peaks. Except for a moderate shift (i.e. about -0.3 eV) of the second and the third signals, detectable due to the higher resolution power at Material Science, the relative peaks distances were in agreement to those reported for NiO samples[130,131,139] and observed for the corresponding powders in our laboratory (see Figure 42). The signals positions and their attributions to different final ionized states of Ni(II) centers are reported in Table 10.

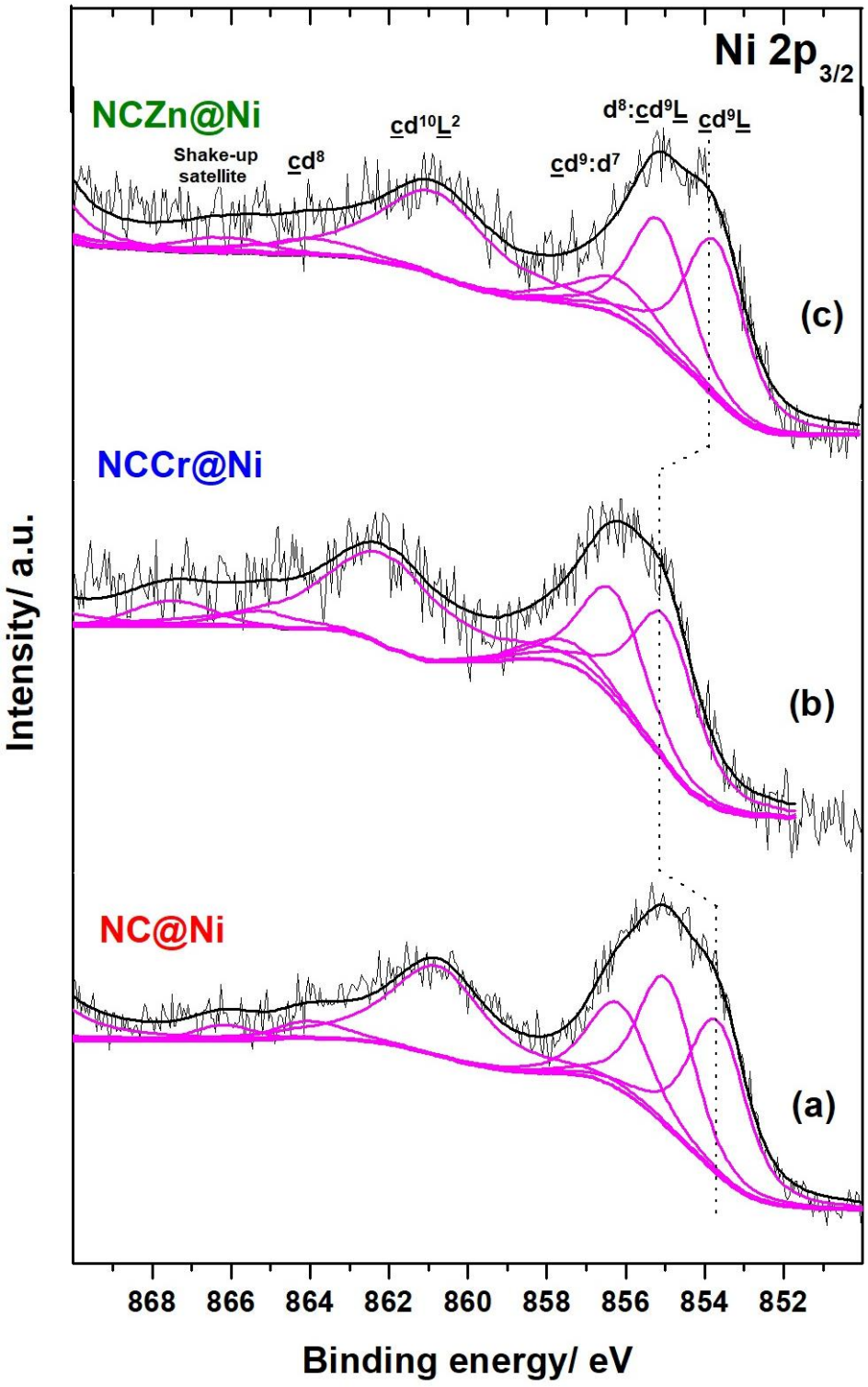

Figure 44. Ni $2p_{3/2}$ XP synchrotron spectra for the (a) NC@Ni, (b) NCCr@Ni and (c) NCZn@Ni pristine electrodes addressed in this work. The BE shift is marked with a dotted line only for the first peak.

Sample	BE position (eV)	Assignments
NC@Ni	853.7	$\underline{c}d^9\underline{L}$
	855.0	d^8:$\underline{c}d^9\underline{L}$
	856.2	$\underline{c}d^9$:d^7 non-local screening
	860.8	$\underline{c}d^{10}\underline{L}^2$
	864.0	$\underline{c}d^8$
	866.2	shake-up satellite
NCCr@Ni	855.0	$\underline{c}d^9\underline{L}$
	856.3	d^8:$\underline{c}d^9\underline{L}$
	857.5	$\underline{c}d^9$:d^7 non-local screening
	862.1	$\underline{c}d^{10}\underline{L}^2$
	865.3	$\underline{c}d^8$
	867.5	shake-up satellite
NCZn@Ni	853.7	$\underline{c}d^9\underline{L}$
	855.1	d^8:$\underline{c}d^9\underline{L}$
	856.2	$\underline{c}d^9$:d^7 non-local screening
	860.8	$\underline{c}d^{10}\underline{L}^2$
	864.0	$\underline{c}d^8$
	866.2	shake-up satellite

Table 10. BE positions and assignments for the peaks determined after curve fitting of the experimental Ni $2p_{3/2}$ synchrotron spectra for the NC@Ni, NCCr@Ni and NCZn@Ni pristine electrodes.

The **Co $2p_{3/2}$ photoionization regions** (Figure 45) were theoretically reconstructed using five peaks. Their relative distances were in good agreement to those reported for Co_3O_4 and $NiCo_2O_4$ samples[59,108,132,135] and observed for the corresponding powders in our laboratory (see Figure 43). As in the Ni$2p_{3/2}$ spectra, a moderate shift (i.e. about −0.3 eV) for the second and the third peaks was observed. The signals positions and their attributions to different final ionized states of Co(II) and Co(III) centers are reported in Table 11. Therefore, the co-presence of Co(II) and Co(III) ions in the $NiCo_2O_4$ spinel lattice was confirmed both in the case of the pure and the doped samples. Moreover, as for the powders, the low intensity of the peak located in the range 785.0-785.8 eV, related to a shake-up satellite of Co(II) sites, was compatible with a Co(II) predominance in tetrahedral sites.[132]

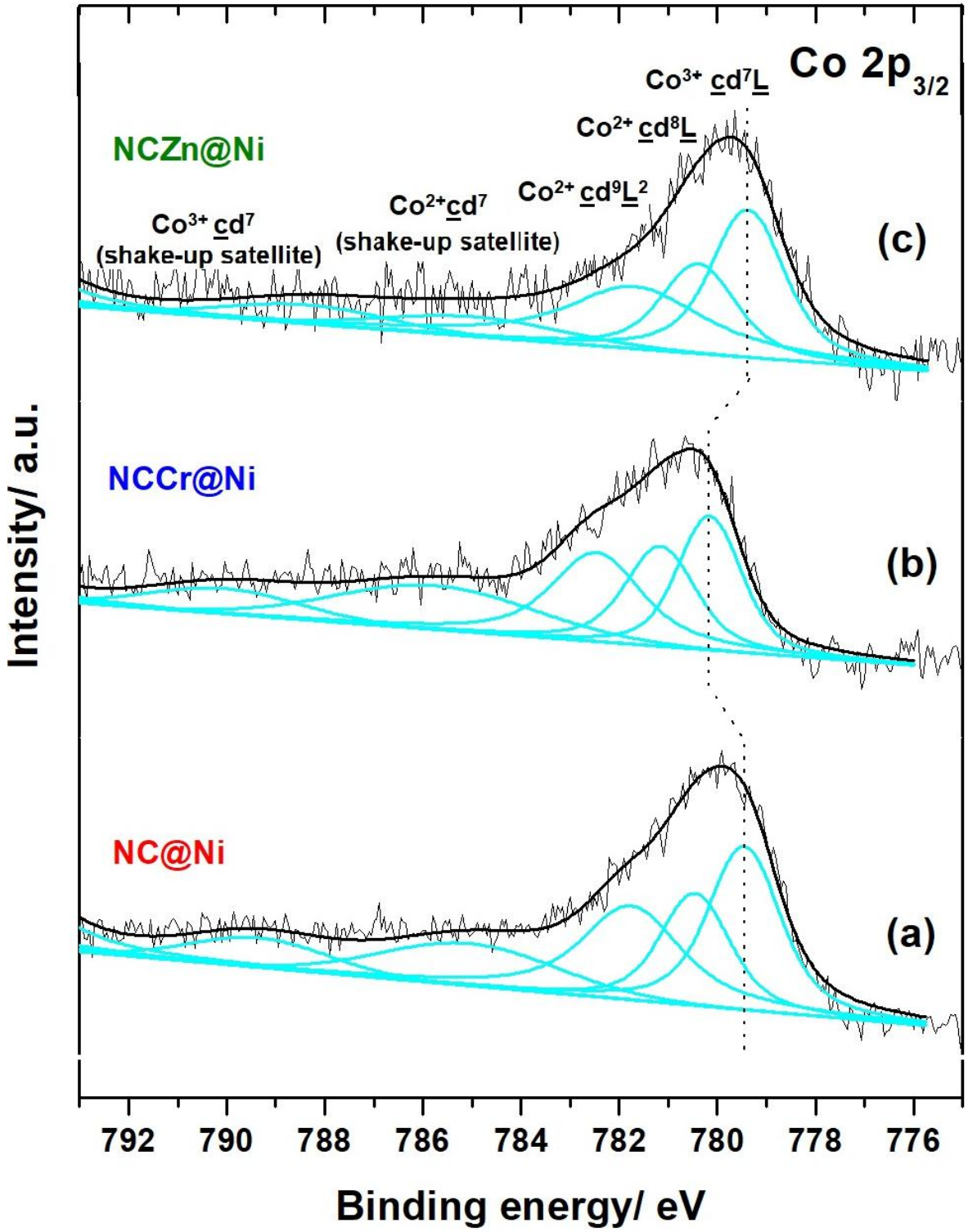

Figure 45. Co $2p_{3/2}$ XP synchrotron spectra for the (a) NC@Ni, (b) NCCr@Ni and (c) NCZn@Ni pristine electrodes addressed in this work. The BE shift is marked with a dotted line only for the first peak.

Sample	BE position (eV)	Assignments
NC@Ni	779.5	Co^{3+} $\underline{c}d^7\underline{L}$
	780.5	Co^{2+} $\underline{c}d^8\underline{L}$
	781.8	Co^{2+} $\underline{c}d^9\underline{L}^2$
	785.1	Co^{2+} $\underline{c}d^7$ (shake-up satellite)
	789.4	Co^{3+} $\underline{c}d^7$ (shake-up satellite)
NCCr@Ni	780.2	Co^{3+} $\underline{c}d^7\underline{L}$
	781.2	Co^{2+} $\underline{c}d^8\underline{L}$
	782.5	Co^{2+} $\underline{c}d^9\underline{L}^2$
	785.8	Co^{2+} $\underline{c}d^7$ (shake-up satellite)
	790.1	Co^{3+} $\underline{c}d^7$ (shake-up satellite)
NCZn@Ni	779.4	Co^{3+} $\underline{c}d^7\underline{L}$
	780.4	Co^{2+} $\underline{c}d^8\underline{L}$
	781.7	Co^{2+} $\underline{c}d^9\underline{L}^2$
	785.0	Co^{2+} $\underline{c}d^7$ (shake-up satellite)
	788.4	Co^{3+} $\underline{c}d^7$ (shake-up satellite)

Table 11. BE positions and assignments for the peaks determined after curve fitting of the experimental Co $2p_{3/2}$ synchrotron spectra for the NC@Ni, NCCr@Ni and NCZn@Ni pristine electrodes.

The reconstruction of the Ni 2p and Co 2p synchrotron spectra confirmed that the pure and doped cobaltites deposited on Ni foam had the same electronic structure of the corresponding powders (see the laboratory and synchrotron spectra of the powders in chapter 5 and Figures 46 and 47, respectively).

Moreover, the data acquired at Materials Science confirmed the existence of a peaks shift towards the high B.E both in the Ni 2p and the Co 2p regions for the doped samples respect to the pure one, particularly in the case of chromium doping. In the synchrotron spectra this shift was quite larger than in the laboratory ones (i.e. minimum shift 0.7 eV, maximum shift 1.2 eV, see chapter 5 for comparison).

As reported in chapter 5, these observations suggested a moderate alteration in the $NiCo_2O_4$ electronic structure due to doping with possible influence on its activity as ORR/OER electrocatalyst. However, a deeper investigation on this effect goes beyond the PhD activity described in this work.

6.3.2. Powders

C 1s, Ni 2p and Co 2p photoemission regions were acquired for the NC, NCCr and NCZn powders. As for the corresponding materials supported on Ni foam, we show only the **Ni $2p_{3/2}$ and Co $2p_{3/2}$ reconstructed spectra** (Figures 46 and 47, respectively). In Tables 12 and 13 are summarized the signals positions and their attributions.

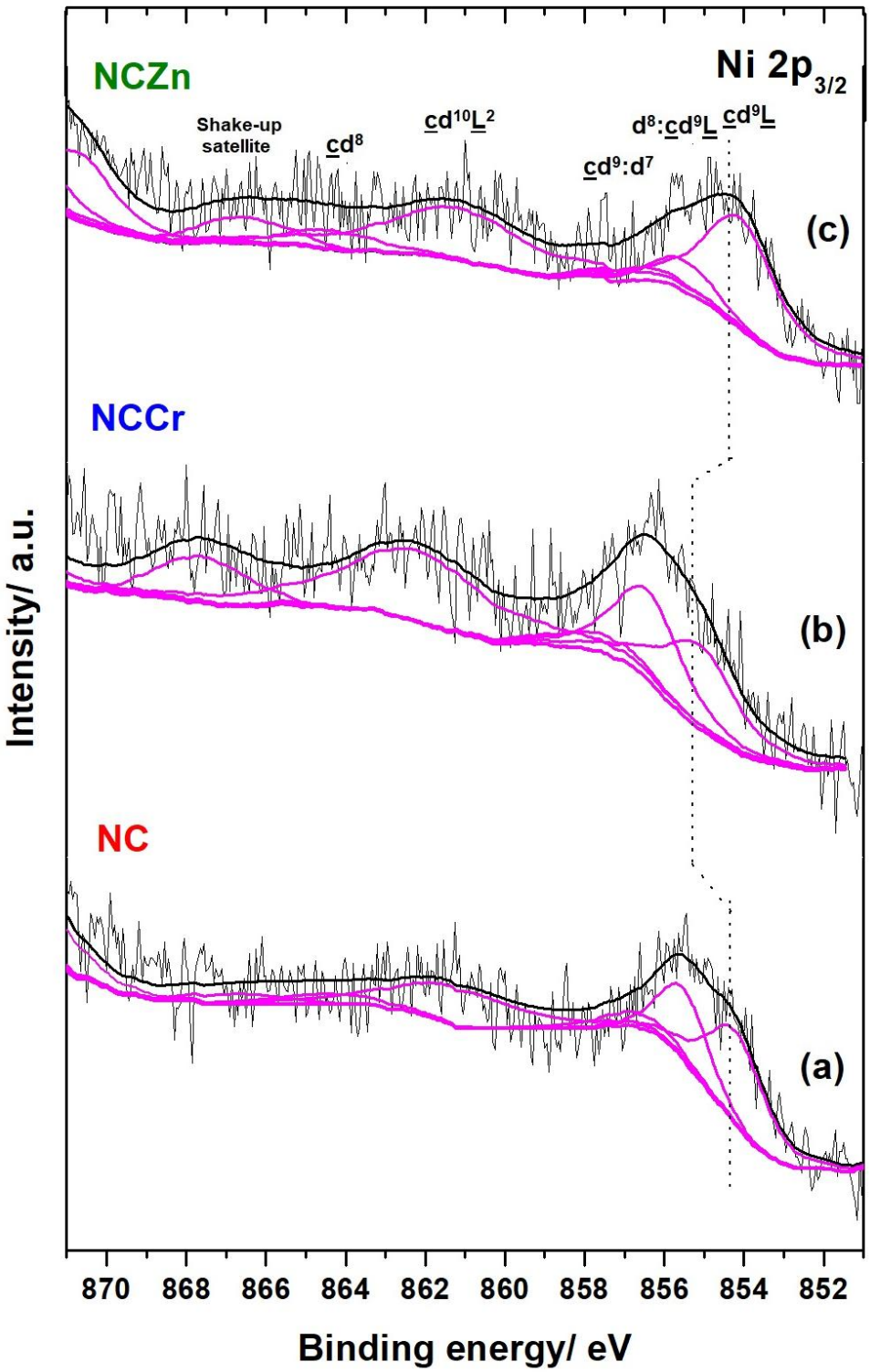

Figure 46. Ni $2p_{3/2}$ XP synchrotron spectra for the (a) NC, (b) NCCr and (c) NCZn powders addressed in this work. The BE shift is marked with a dotted line only for the first peak.

Sample	BE position (eV)	Assignments
NC	854.2	$\underline{c}d^9\underline{L}$
	855.5	d^8:$\underline{c}d^9\underline{L}$
	856.7	$\underline{c}d^9$:d^7 non-local screening
	861.3	$\underline{c}d^{10}\underline{L}^2$
	864.5	$\underline{c}d^8$
	866.7	shake-up satellite
NCCr	855.1	$\underline{c}d^9\underline{L}$
	856.4	d^8:$\underline{c}d^9\underline{L}$
	857.6	$\underline{c}d^9$:d^7 non-local screening
	862.2	$\underline{c}d^{10}\underline{L}^2$
	865.4	$\underline{c}d^8$
	867.7	shake-up satellite
NCZn	854.3	$\underline{c}d^9\underline{L}$
	855.7	d^8:$\underline{c}d^9\underline{L}$
	856.8	$\underline{c}d^9$:d^7 non-local screening
	861.4	$\underline{c}d^{10}\underline{L}^2$
	864.6	$\underline{c}d^8$
	866.8	shake-up satellite

Table 12. BE positions and assignments for the peaks determined after curve fitting of the experimental Ni $2p_{3/2}$ synchrotron spectra for the NC, NCCr and NCZn powders.

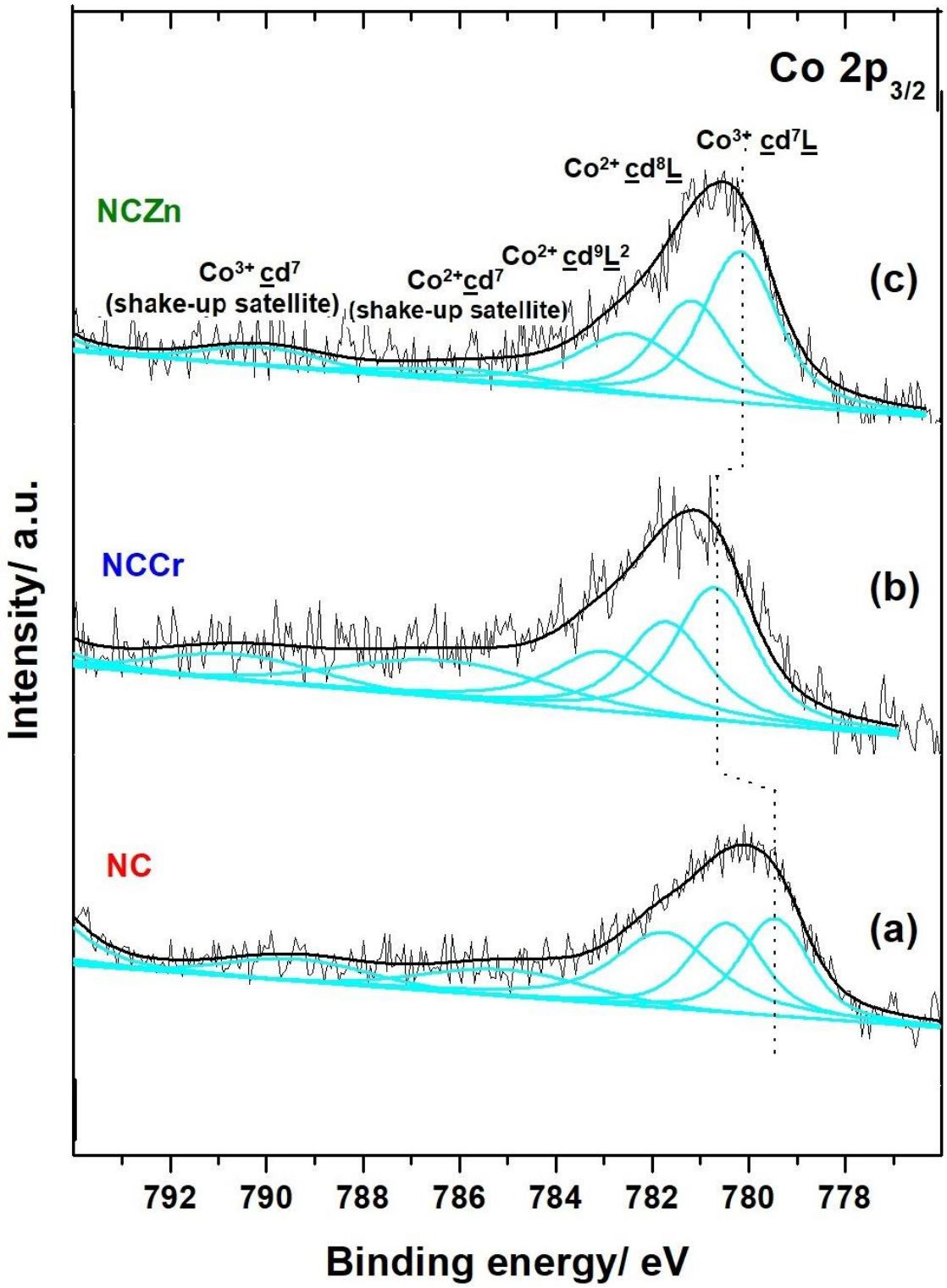

Figure 47. Co $2p_{3/2}$ XP synchrotron spectra for the (a) NC, (b) NCCr and (c) NCZn powders addressed in this work. The BE shift is marked with a dotted line only for the first peak.

Sample	BE position (eV)	Assignments
NC	779.5	Co^{3+} $\underline{c}d^7\underline{L}$
	780.5	Co^{2+} $\underline{c}d^8\underline{L}$
	781.8	$Co^{2+}\underline{c}d^9\underline{L}^2$
	785.1	Co^{2+} $\underline{c}d^7$ (shake-up satellite)
	789.4	Co^{3+} $\underline{c}d^7$ (shake-up satellite)
NCCr	780.7	Co^{3+} $\underline{c}d^7\underline{L}$
	781.7	Co^{2+} $\underline{c}d^8\underline{L}$
	783.0	Co^{2+} $\underline{c}d^9\underline{L}^2$
	786.3	Co^{2+} $\underline{c}d^7$ (shake-up satellite)
	790.6	Co^{3+} $\underline{c}d^7$ (shake-up satellite)
NCZn	780.2	Co^{3+} $\underline{c}d^7\underline{L}$
	781.2	Co^{2+} $\underline{c}d^8\underline{L}$
	782.5	Co^{2+} $\underline{c}d^9\underline{L}^2$
	785.8	Co^{2+} $\underline{c}d^7$ (shake-up satellite)
	790.1	Co^{3+} $\underline{c}d^7$ (shake-up satellite)

Table 13. BE positions and assignments for the peaks determined after curve fitting of the experimental Co $2p_{3/2}$ synchrotron spectra for the NC, NCCr and NCZn powders.

No significant differences in terms of number of peaks, relative positions and shifts due to doping were revealed respect to those observed for the same samples measured in our laboratory (see Figures 42 and 43) and for the pristine electrodes analyzed at Materials Science (see Figures 44 and 45).

As performed previously working on our laboratory XPS data (see chapter 5, paragraph 5.4.4), for the powders, in absence of spectral contributions from the Ni foam, a relative quantification between Co and Ni was attempted. The higher sensitivity at Materials Science led to different numeric values for the Co/Ni ratios respect to those shown in chapter 5. However, the registration of the same trend moving from the pure to the doped samples (see Table 8 and Table 14) confirmed a decrease of the Ni concentration at the surface due to doping.

Sample	Co/Ni atomic ratio
NC	2.27
NCCr	1.30
NCZn	1.26

Table 14. Co/Ni atomic ratios calculated for the NC,NCCr and NCZn powders with reference to their synchrotron XP spectra. The decrease of the Ni concentration at the surface due to doping, previously evaluated in our laboratory, was confirmed.

The higher resolving power available at Elettra allowed to perform also a relative quantification between Co(III) and Co(II) with reference to both their main signals and their satellites. The Co^{3+}/Co^{2+} ratios for the NC, NCCr and NCZn samples reported in Table 15 highlighted a decrease of the Co^{2+} concentration at the surface due to doping.

Sample	Co^{3+}/Co^{2+} atomic ratio
NC	0.50
NCCr	0.67
NCZn	0.81

Table 15. Co^{3+}/Co^{2+} atomic ratios for the NC, NCCr and NCZn powders. A decrease of the Co^{2+} concentration at the surface due to doping was registered.

Overall, as inferred on the basis of our laboratory measurements, combining the results reported in Tables 14 and 15, we confirmed a modification of the chemical surface composition of the $NiCo_2O_4$ material when doped with chromium or zinc. Particularly, we demonstrated that Cr(III) and Zn(II) ions substituted both Ni(III)/Ni(II) and Co(II) centers at the surface. This evidence further supported our hypothesis about the existence of a relationship between an alteration in the electrocatalyst surface composition and the O_2 and LiO_2 adsorption kinetics, leading to boosted kinetics for the ORR/OER in Li-O_2 cells (see chapter 5, paragraph 5.3.3).

6.3.3. Post-mortem cathodes

NC@Ni, NCCr@Ni and NCZn@Ni cathodes extracted from cells discharged to 2.0 V and cycled between 2.0 and 4.1 V at J = 0.025 mA cm^{-2} and from a battery set to 100 cycles at J = 0.2 mA cm^{-2} limiting the capacity at 0.1 mAh cm^{-2} (see Figures 23 a and 24 a for the electrochemical performance) were analyzed ex-situ in order to evaluate possible modification in their surface composition upon cycling and until the cell death. All the samples showed very low S/N ratio in the **Ni 2p and Co 2p spectral regions** (data not shown), so no attempts were given to their theoretical reconstruction by means of a curve fitting procedure.

One possible reason for the low intensity registered in these regions could be the attenuation of the photoelectrons from the $NiCo_2O_4$ by layers covering its surface made of discharged (i.e. lithium oxides) and degradation products (i.e. organic compounds from the solvent) and residual TEGDME/LiTFSI electrolyte solution.

Even if at Materials Science an exciting radiation of 1000 eV was adopted to record the Ni 2p (BE ~ 854 eV) and Co 2p (BE ~ 780 eV) spectra in order to increase the photoionization cross-section (thereby obtaining higher intensity than with our lab XPS), such a decrease in photon energy (1000 vs. 1486.7 eV of our lab), as shown in Figure 48, was followed by the emission of photoelectrons with correspondingly lower kinetic energy. As a consequence, due to a lower electron inelastic mean free path (λ), the surface sensitivity

of the measurement was enhanced and the signals from the cobaltite were probably attenuated, while those from the species grown over there during operation in the cell were enhanced.

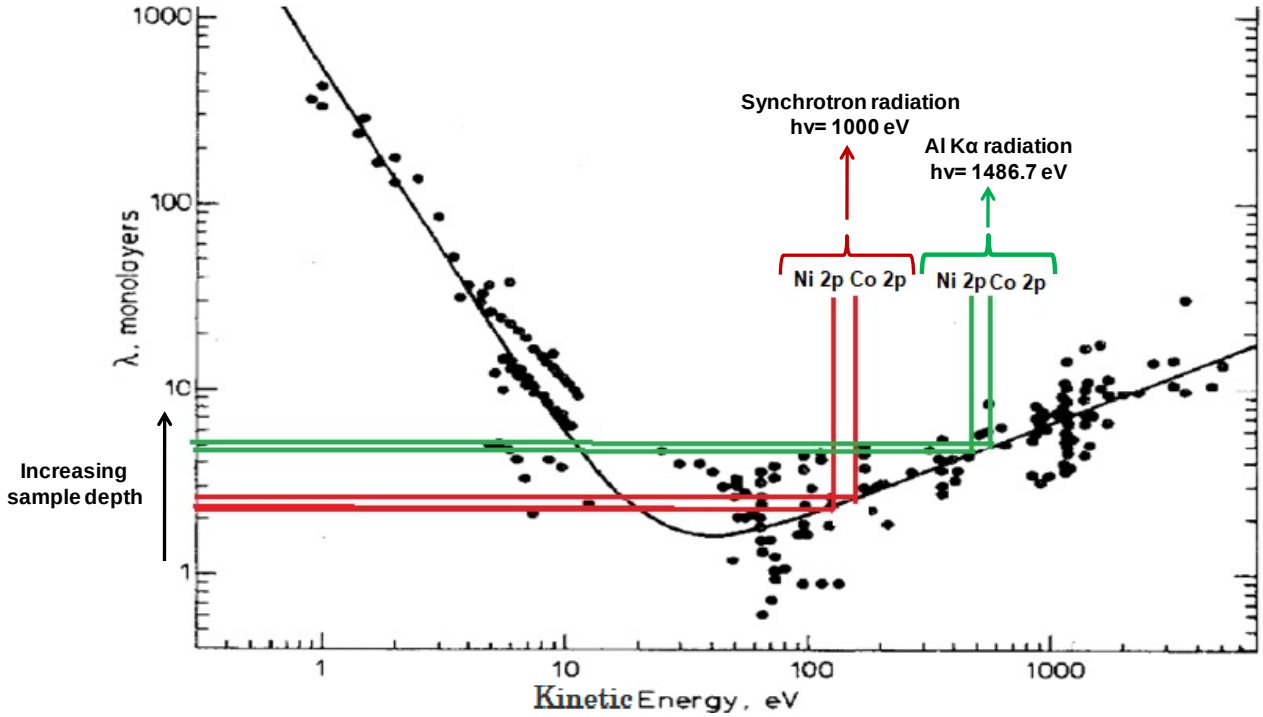

Figure 48. Photoelectrons inelastic mean free path (λ) as a function of their kinetic energy. Adopting a radiation of 1000 eV instead of an Al Kα source (i.e. 1486.7 eV), the sample thickness that can be analyzed decreases (i.e. XPS surface sensitivity increases).

The **C 1s photoemission regions** are reported in Figure 49 for all the samples. As in the case of our laboratory work (see chapter 5, paragraph 5.4.4), the BE of the first peak belonging to the $–CH_2–$ groups of the aliphatic carbon contamination was fixed at 284.8 eV and was used as an internal standard reference for the BE scale. All the pristine materials (spectra a in Figure 49 α,β,γ) show other two peaks related to oxidized functions (i.e. C-O, C-O-C etc) at the carbon surface (285.2-285.7 eV)[99] and to higher oxidized carbonaceous groups possibly grown due to the X-ray exposition[99] (288.2-289.5 eV). For all the post-mortem cathodes (spectra b,c,d in Figure 49 α,β,γ), the additional features at 286.4-286.8 and 292.5-293.0 eV are associated with ethereal C−O bonds in TEGDME[82,99] and with $−CF_3$ groups in $TFSI^-$ anion,[100,101] respectively.

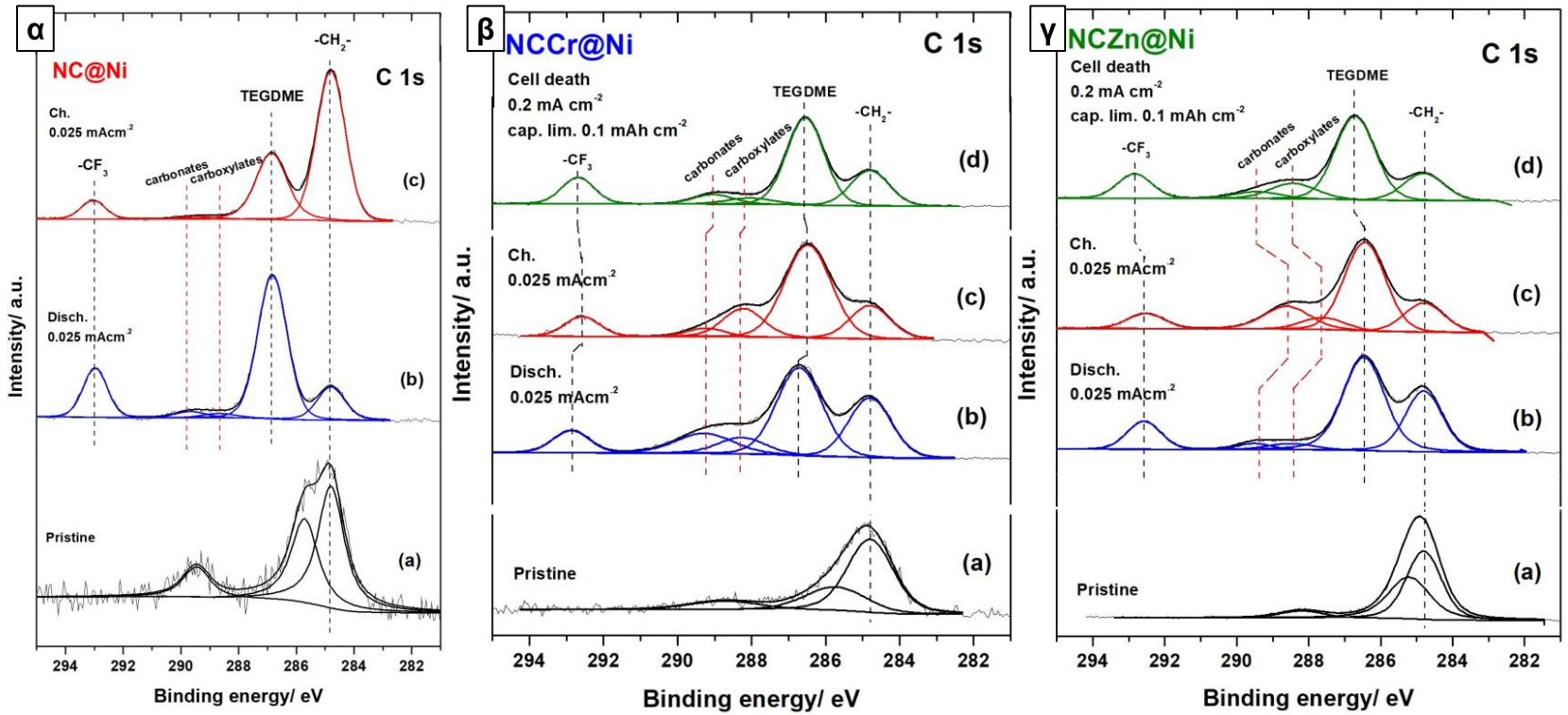

Figure 49. C 1s photoemission regions for the (α) NC@Ni, (β) NCCr@Ni and (γ) NCZn@Ni cathodes analyzed ex-situ by means of synchrotron radiation. For all the materials, (a) are the pristine, (b) the discharged and (c) the cycled samples. In the case of the NCCr@Ni and NCZn@Ni materials, (d) are the cathodes from cells set to 100 cycles extracted at the cycle of death. See text for more details.

The spectra b in Figure 49 α,β,γ show the effect of discharging the cells to 2.0V at J = 0.025 mA cm^{-2}. Two signals associated with carboxylate and carbonate groups[82,99–103] appear at 288.3-288.7 eV and 289.3-289.7 eV, respectively. Their presence calls for the occurrence of degradation phenomena related to the TEGDME solvent, possibly due to the exposition to Li_2O_2 particles.[39] So, carboxylates and carbonates mainly constituted the amorphous aggregates, surrounding the $NiCo_2O_4$ nanowires and occluding their pores, observed in SEM images of the same samples (see Figure 33 b for the NCCr@Ni cathode). These species grow on discharge due to oxidative chemical attacks to the organic solvent. So, it was not surprising that the intensity of their signals was higher in the case of the doped samples (spectra b in Figure 49 β,γ) that performed longer discharges respect to the pure one (spectrum b in Figure 49 α).

For the cathodes charged up to 4.1 V at J = 0.025 mA cm^{-2} (spectra c in Figure 49 α,β,γ), there are no differences respect to the discharged ones. In fact, both carboxylates and carbonates are still present on their surface. This is a portrait quite different from that obtained with SEM imaging where a complete reversibility was observed (see Figure 33 c for the NCCr@Ni cathode).

This apparent discrepancy can be explained with the different sampling depth of these two techniques. SEM allowed us to observe the bulk of the $NiCo_2O_4$ nanofibers while, the radiation of 400 eV adopted at Materials Science to excite the C 1s photoionization, allowed to obtain information on the chemical composition of about only 10 atomic layers (see Figure 48) and detect residual degradation compounds in the cathodes pores.

We concluded that, despite their remarkable electrochemical performance, the doped materials do not ensure a complete reversibility in terms of degradation compounds removal even at the first cycle.

Also the spectra for the NCCr@Ni and NCZn@Ni cathodes cycled within the voltage range 2.0 V and 4.1 V at J = 0.2 mA cm^{-2} with a capacity limitation of 0.1 mA h cm^{-2} until the cell death (spectra d in Figure 49 β,γ), showed carboxylates and carbonates peaks. This confirms our hypothesis, formulated on the basis of SEM observations (see Figure 34 b for the NCZn@Ni cathode), on the possible relationship between cell death and deactivation of the $NiCo_2O_4$ electrocatalyst due to occlusion of its surface and pores by insulating organic compounds derived from TEGDME oxidative decomposition.

All the **Li 1s photoemission regions** (Figure 50) show a broad and less structured signal. We speculated about the phenomena occurring on discharge, on charge and until cell death evaluating the shift of the centroid of this large peak upon the various electrochemical conditions (Table 16).

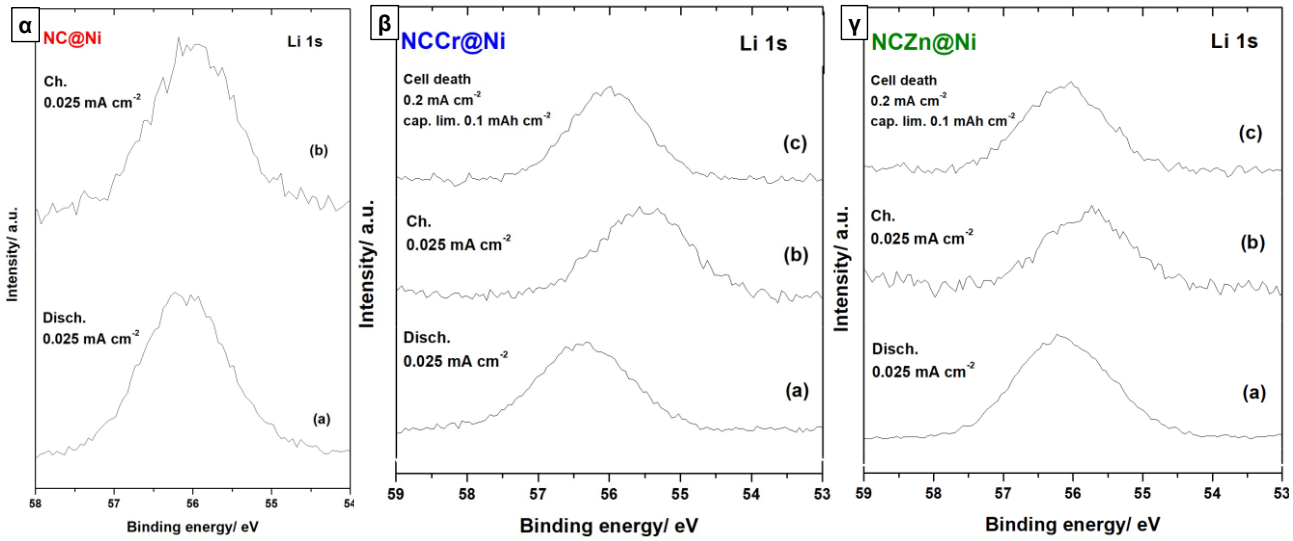

Figure 50. Li 1s photoemission regions for the (α) NC@Ni, (β) NCCr@Ni and (γ) NCZn@Ni cathodes analyzed ex-situ by means of synchrotron radiation. For all the materials, (a) are the discharged and (b) the cycled samples. In the case of the NCCr@Ni and NCZn@Ni materials, (d) are the cathodes from cells set to 100 cycles extracted at the cycle of death. See text for more details.

Material	Sample	Centroid position (eV)
NC@Ni	D. 2.0 V	56.1
	C. 4.1 V	56.0
NCCr@Ni	D. 2.0 V	56.4
	C. 4.1 V	55.5
	Cell death	56.1
NCZn@Ni	D. 2.0 V	56.1
	C. 4.1 V	55.8
	Cell death	56.1

Table 16. Centroid positions for the broad signal observed in the synchrotron Li 1s spectra for the NC@Ni, NCCr@Ni and NCZn@Ni cathodes extracted from cells that worked in various electrochemical conditions.

On discharge the centroid position is at 56.1 eV for all the samples (spectra a in Figure 50 α,β,γ). On charge we observe a shift towards the low BE for the doped samples (i.e. to 55.5 and 55.8 eV for NCCr@Ni and NCZn@Ni, respectively) but not for the pure one (spectra b in Figure 50 α,β,γ). So, we supposed a reversible formation of lithium oxides species only on the doped electrodes, for which at 4.1 V residual LiTFSI could be detectable. In fact, as observed in the C 1s regions, in the Li 1s ones, the signal for the LiTFSI salt physisorbed on cobaltite-based materials was expected to be at low BE respect to that reported on a carbon cathode (see chapter 4, paragraph 4.4.3). This speculation was supported by the reversible formation of Li_2O_2

flower-like particles observed in SEM images for the discharged and cycled NCCr@Ni cathode at J = 0.025 mA cm^{-2} (see Figure 33 b-c).

At the cell death, both for the NCCr@Ni and the NCZn@Ni materials the position of the centroid is at 56.1 eV (spectra c in Figure50 β,γ), suggesting loss of reversibility upon cycling and the accumulation of lithium oxides on the cathodes. This hypothesis accords with the occlusion of the $NiCo_2O_4$ nanowires surface and pores observed by SEM, particularly for the early dead NCZn@Ni cathode (see Figure 34).

It is worth noting that the analysis of the synchrotron Li 1s photoemission regions highlighted that not only organic degradation compounds from TEGDME but also lithium oxides deposits contributed to the deactivation of the $NiCo_2O_4$ electrocatalyst. Moreover, the effect of the current density on the lithium oxides growth mechanism and morphology was further confirmed.[23] In fact, amorphous and/or very low dimension Li_2O_2 particles occluded the cobaltite nanowires of the dead electrodes (Figure 34) cycled at J = 0.2 mA cm^{-2}, instead of the large crystalline flower-like particles formed onto the NCCr@Ni electrode discharged at J = 0.025 mA cm^{-2} (Figure 33 b).

6.4. Conclusions

By means of XPS measurements with synchrotron radiation performed at the Materials Science beamline of Elettra, we completed the characterization of the NC@Ni, NCCr@Niand the NCZn@Ni pristine electrodes started in our laboratory. Particularly, we assessed the analogy of their electronic structure, previously demonstrated only for the corresponding powders. Analyzing also the NC, NCCr and NCZn unsupported samples by means of synchrotron radiation, we confirmed a modification in the surface composition of the cobaltite due to doping. Particularly, a decrease in both the Co/Ni and Co^{3+}/Co^{2+} atomic ratios was registered, assessing the substitution of Cr(III) and Zn(II) dopants to both Ni(III)/Ni(II) and Co(II) centers at the surface. These changes could influence the electrocatalytic activity of the material due to different LiO_2 and O_2 adsorption kinetics with consequential effects on the ORR/OER process.

Taking advantage of the high resolving power and sensitivity at Material Science, we registered post-mortem XP spectra for selected NC@Ni, NCCr@Ni and NCZn@Ni cathodes extracted from cells that had worked in various electrochemical conditions.

We demonstrated the growth on discharge both on the doped and the pure electrodes of carboxylates and carbonates as degradation products from the solvent TEGDME. This process was proved to be irreversible even at the first cycle for all the samples. Instead, the formation of lithium oxides compounds appeared reversible on the doped cathodes but not on the pure one. The failure in long-term tests of the cells assembled with NCCr@Ni and NCZn@Ni as cathodes was confirmed to be related to the deactivation of the electrocatalyst due to the occlusion of its surface and pores. Interestingly, at cell death not only degradation compounds but also lithium oxides particles were detected on the electrodes, both contributing with their insulating character to the rise of the overvoltage upon cycling.

CHAPTER 7

Study on the use of Pd as co-catalyst

7.1. Aims

As described in chapter 1, paragraph 1.4, Li-O_2 cell electrochemical performance can be further enhanced taking advantage from a synergistic effect between a co-catalyst and the active material at the positive electrode.[36,71,72,73,74,75] Particularly, the co-catalytic effect of Pd nanoparticles deposited on a nanostructured $NiCo_2O_4$-based cathode has been recently reported. However, in this study the influence on the overall cell performance of the reactivity of a carbon foam used as support cannot be excluded.[76]

So, another step of the research described in this text was to investigate the possible co-catalytic activity of Pd nanoparticles (Pd NP) deposited onto the previously investigated NCCr@Ni material in a complete carbon-free context.

7.2. Samples preparation

Composite Pd/PdO@NCCr@Ni electrodes were synthesized at the University of Basilicata, in collaboration with the research team of Dr. Angela De Bonis, particularly involved in the Pd NP preparation by pulsed lased ablation in liquid acetone (PLAL).

PLAL is an emerging bottom-up approach widely used to synthesize nanomaterials with controlled structures and morphologies[140], whose properties can be easily tuned by an appropriate combination of solvents, additives and targets.[141]

A target of metallic Pd was immersed in liquid acetone and ablated with a pulsed Ti:Sapphire Spectra Physics - Spitfire laser in the fs regime (Figure 51), following a procedure optimized previously.[142,143] The laser fundamental wavelength was equal to 800 nm. The pulse duration was 120 fs with a repetition rate of 1 KHz. The spot on the Pd target was 10^{-3} cm^2, so the fluence was 3.5 J cm^{-2}. Approximately, the resulting concentration of the NP in acetone was 100 μg mL^{-1}.

NCCr@Ni samples were prepared as reported in chapter 5, paragraph 5.2, and then decorated with Pd NP by drop casting of 1 mL of their suspension on the surface. The resulting Pd/PdO@NCCr@Ni electrodes were finally calcined at 300 °C for 4 h in air. Approximately, the Pd NP loading on the cobaltite was 66 μg cm^{-2}.

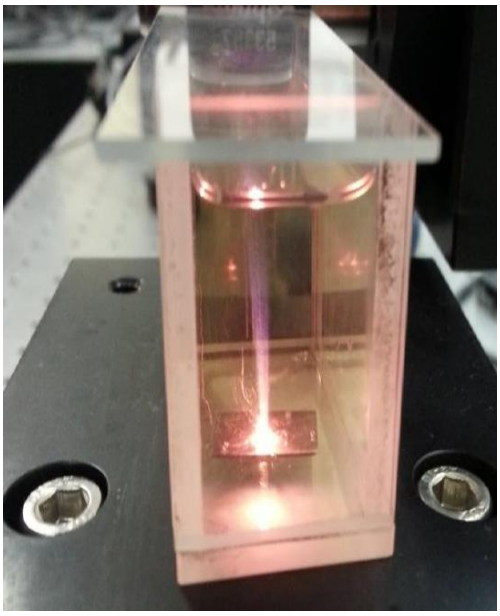

Figure 51. Pulsed laser ablation in liquid (PLAL) of a target of metallic Pd in acetone in order to prepare a suspension of Pd nanoparticles to be deposited on NCCr@Ni electrodes.

7.3. Electrochemical tests

Li-O_2 cells with Pd/PdO@NCCr@Ni materials as positive electrodes were assembled in the same configuration and adopting the same experimental equipment of the tests on the nickel cobaltite-based cathodes described in chapter 5, paragraph 5.3.

In a first set of experiments, galvanostatic cycling of the cells were carried out, imposing a current density of 0.05 mA cm^{-2} and cut-off voltages of 2.0 V and 4.1 V in discharge and charge, respectively. The measured capacity was normalized dividing by the geometrical area of electrode (1.54 cm^2). In another set of experiments, the long-term performance of the cells was tested, so they were galvanostatically discharged/charged with a capacity limit of 0.2 mAh cm^{-2} at a current density value of 0.2 mA cm^{-2}. After the electrochemical tests, the cells were disassembled in an argon-filled glovebox. The post-mortem electrodes were recuperated and washed in TEGDME and in THF to remove the excess electrolyte, and dried under vacuum at room temperature. Recuperated cathodes were characterized by XPS.

7.3.1. Voltage limited performance on one cycle

The performance on one cycle of discharge/charge between 2.0 V and 4.1 V at J = 0.05 mA cm^{-2} of the composed Pd/PdO@NCCr@Ni electrode is reported in Figure 52 in comparison with that of a NCCr@Ni bare cathode.

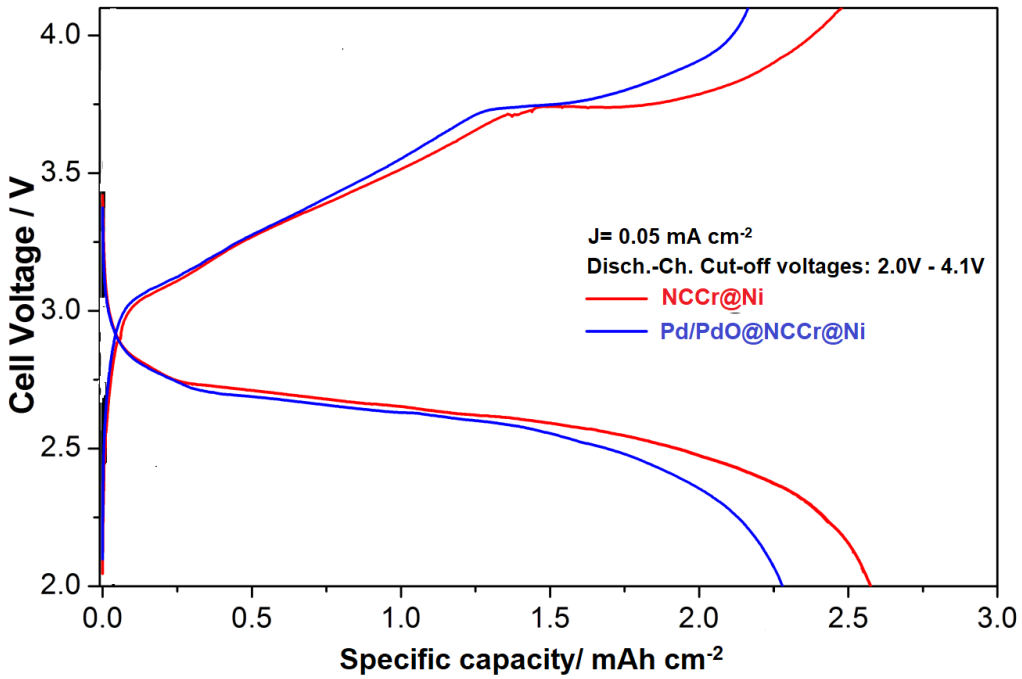

Figure 52. Comparison between the performance on one galvanostatic cycle between 2.0 and 4.1 V at J = 0.05 mA cm^{-2} of the Pd/PdO@NCCr@Ni (blue curve) and the NCCr@Ni(red curve) cathodes.

The Pd-decorated electrode almost matched the discharge capacity of the bare one (2.28 mAh cm^{-2} and 2.60 mAh cm^{-2} for the Pd/PdO@NCCr@Ni and the NCCr@Ni samples, respectively) as well as the charge capacity and the mean operating voltages.

The obtained areal capacity value for the Pd/PdO@NCCr@Ni electrode was in agreement with the findings reported in literature for composite electrodes made of Pd impregnated on $NiCo_2O_4$ deposited on a carbon support (metallic Pd loading 200 μg cm^{-2}, discharge capacity registered in a Li-O_2 cell of about 3.2 mAh cm^{-2} at a current density of about 0.16 mA cm^{-2}).[76] The larger capacity value measured by Agyeman et al. compared to ours could be due to their larger noble metal NP areal concentration and/or to their more efficient gas transport through the carbon-based gas-diffusion layer compared to the open Ni foam.

Overall, the comparison of the performance on one cycle of the Pd/PdO@NCCr@Ni respect to the NCCr@Ni suggested an essential key-role played by the mixed oxide in the electro-catalysis and an apparent marginal enhancement of the ORR/OER exerted by the Pd NP.

7.3.2. Long-term performance

The cycling performance of both the Pd/PdO@NCCr@Ni and the NCCr@Ni electrodes in galvanostatic tests at J = 0.2 mA cm^{-2} with a capacity limitation of 0.2 mAh cm^{-2} are shown in Figure 53.

The capacity limitation was successfully reached with a coulombic efficiency of 100% between charge and discharge for 40 cycles in the case of the Pd/PdO@NCCr@Ni cathode, whereas the NCCr@Ni electrode failed at cycle 16. Thus, despite their not significant influence on the first cycle, the Pd NP proved to enhance the long-term reversibility of the ORR/OER reactions.

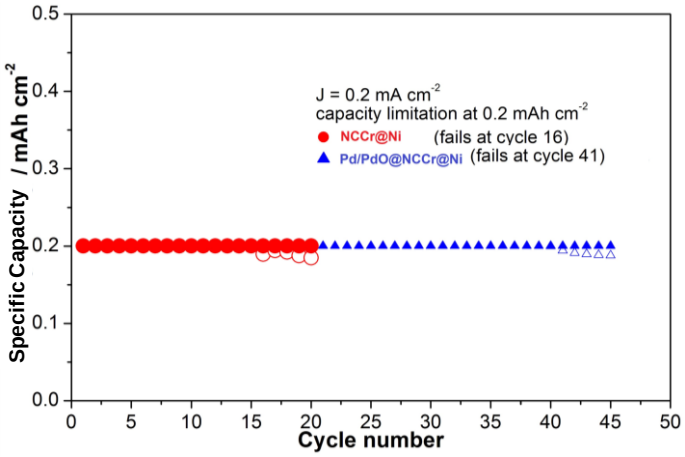

Figure 53. Comparison between the performance upon cycling of the Pd/PdO@NCCr@Ni (blue triangles) and the NCCr@Ni (red spheres) electrodes.

The Pd-decorated electrode showed smaller overvoltages upon cycling compared to the bare one. The values and trends of the discharge (ORR) and charge (OER) mean voltages for the Pd/PdO@NCCr@Ni and NCCr@Ni samples are compared in Figure 54 a and b, respectively, and the corresponding voltage hysteresis is shown in Figure 54 c. The mean cell voltage in discharge upon cycling was higher for the Pd/PdO@NCCr@Ni electrode compared to the NCCr@Ni of approximately 0.18 V due to the smaller ORR overvoltages. The same trend was observed upon charge where the mean operating voltages for the Pd/PdO@NCCr@Ni material was about 0.14 V smaller compared to the NCCr@Ni one, thanks to the smaller OER overvoltages. These combined beneficial effects provided by the Pd nanoparticles lead to a smaller voltage hysteresis of approximately 0.30-0.35 V between discharge and charge.

Turning to the cell failure, it occurred for both materials during the discharge stage due to an increase of the ORR overvoltages cycle-by-cycle. As reported in literature and demonstrated by us in our previous studies (see chapters 4, 5 and 6),[19] the increase of the overvoltages upon cycling in Li-O_2 cell is mainly due to the passivation of the electro-catalyst by the accumulation of solvent degradation by-products over the positive electrode. In this view, the longer cycling life observed for the Pd/PdO@NCCr@Ni sample in respect to the bare one was an evidence of a delayed de-activation of the electro-catalyst surface, and possibly a clue of the mitigation of the solvent degradation reactions.

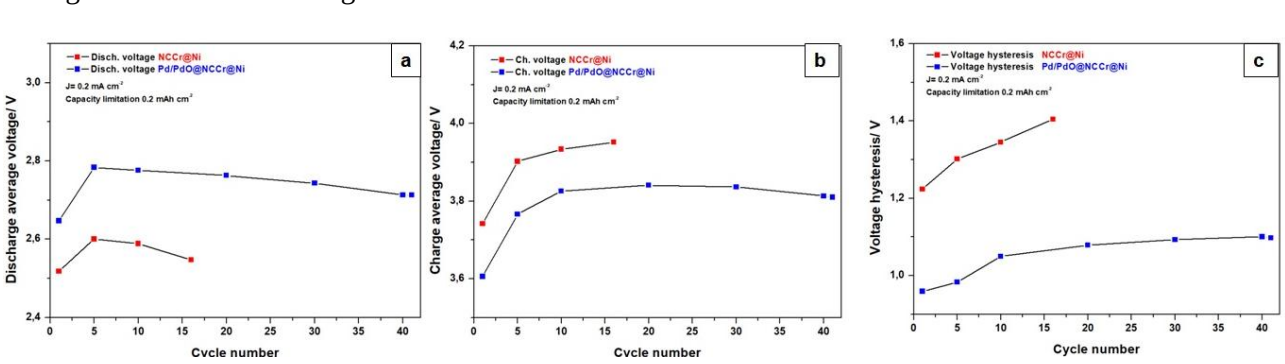

Figure 54. Performance upon cycling of the Pd/PdO@NCCr@Ni (blue) and the NCCr@Ni (red) electrodes: (a-b) mean discharge/charge voltages; (c) voltage hysteresis.

7.4. Chemical characterization

7.4.1. Pristine materials

The results of the physico-chemical characterization of the palladium nanoparticles synthesized by PLAL before the deposition onto to the mixed oxide electrodes are shown in Figure 55.

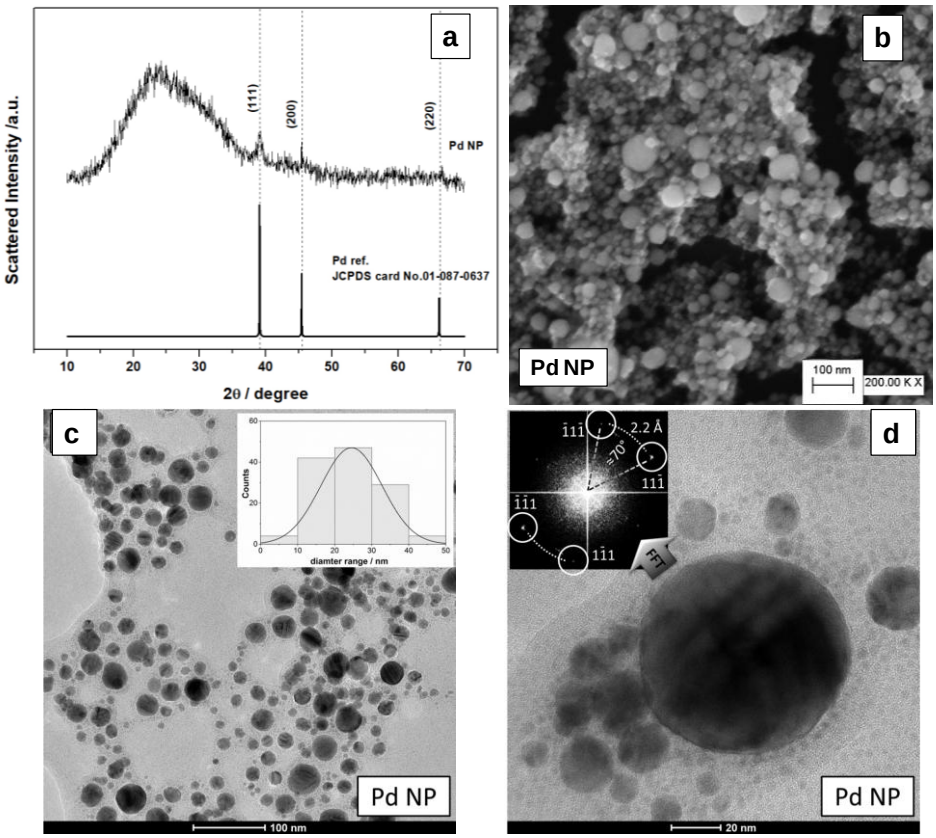

Figure 55. (a) Diffraction patterns of the Pd nanoparticles compared to the reference; (b) morphology of the Pd nanoparticles by FE-SEM; (c-d) TEM pictures at different magnifications of the Pd nanoparticles (c inset: particle size distribution; d inset: FFT analysis of the Pd NP corresponding to a diffraction pattern in [010]).

The diffraction pattern of the Pd nanoparticles accumulated onto a silicon wafer from the acetone suspension (Figure 55 a) showed the expected peaks for metallic Pd (JCPDS Card No. 01-087-0637)[144]. From the morphological point of view, FE-SEM and TEM images (Figure 55 b-d) highlighted the formation of rounded multi-sized nanoparticles. The mean NP diameter was estimated by the TEM picture analysis and fall in the range 10-30 nm. These nanoparticles appeared highly crystalline as demonstrated by the indexing of the electron diffraction pattern in the [010] zone derived by the selected area Fast-Fourier-Transform (FFT) of the Figure 55 d.[142,145]

A full characterization of the composed Pd/PdO@NCCr@Ni electrodes was performed by means of SEM, XRD and XPS.

The comparison between the morphology by SEM of the bare and Pd-decorated electrodes is shown in Figure 56.

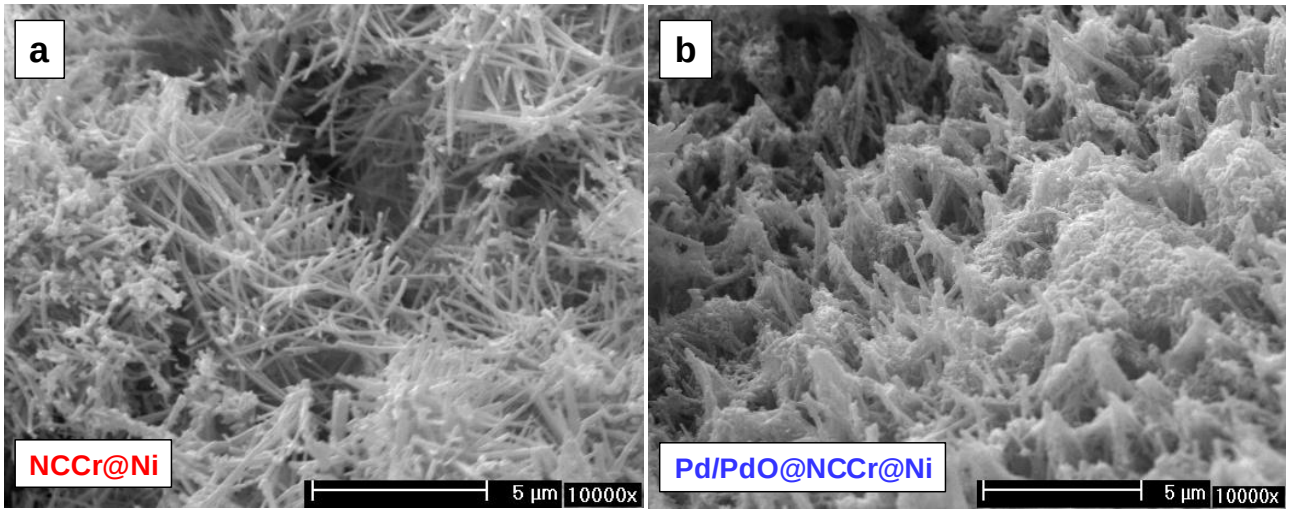

Figure 56. SEM pictures of (a) the NCCr@Ni sample compared to (b) the Pd/PdO@NCCr@Ni one.

While the NCCr@Ni surface was constituted by well separated oxide-based polycrystalline fibers, the Pd/PdO@NCCr@Ni material showed a partial aggregation of the polycrystalline oxide nanowires and accumulation of round particles among the nanostructures. Therefore, the resulting surface morphology of the Pd-decorated electrodes was qualitatively more compact with less voids compared to the bare one.

As expected, the XRD pattern for the Pd/PdO@NCCr@Ni (Figure 57) sample showed the peaks of a cubic $NiCo_2O_4$ phase (JCPDS Card No. 73-1702).[47] Additional reflections could be assigned to the Ni foam (JCPDS Card No. 04-0850),[144] to traces of NiO (JCPDS Card No. 73-1523)[127] grown from the Ni mesh due to the spontaneous corrosion in alkaline aqueous solutions[128] and to metallic Pd (JCPDS Card No. 01-087-0637).[144] The EDS analysis performed on the area of the Pd-decorated sample shown in the FE-SEM picture in Figure 58 confirmed the homogeneous distributions of both the Cr^{3+} dopant and the Pd co-catalyst on the cobaltite nanowires.

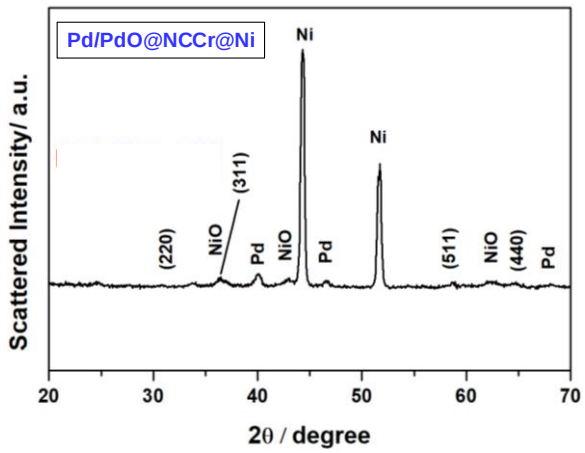

Figure 57. Diffraction pattern of the Pd/PdO@NCCr@Ni sample.

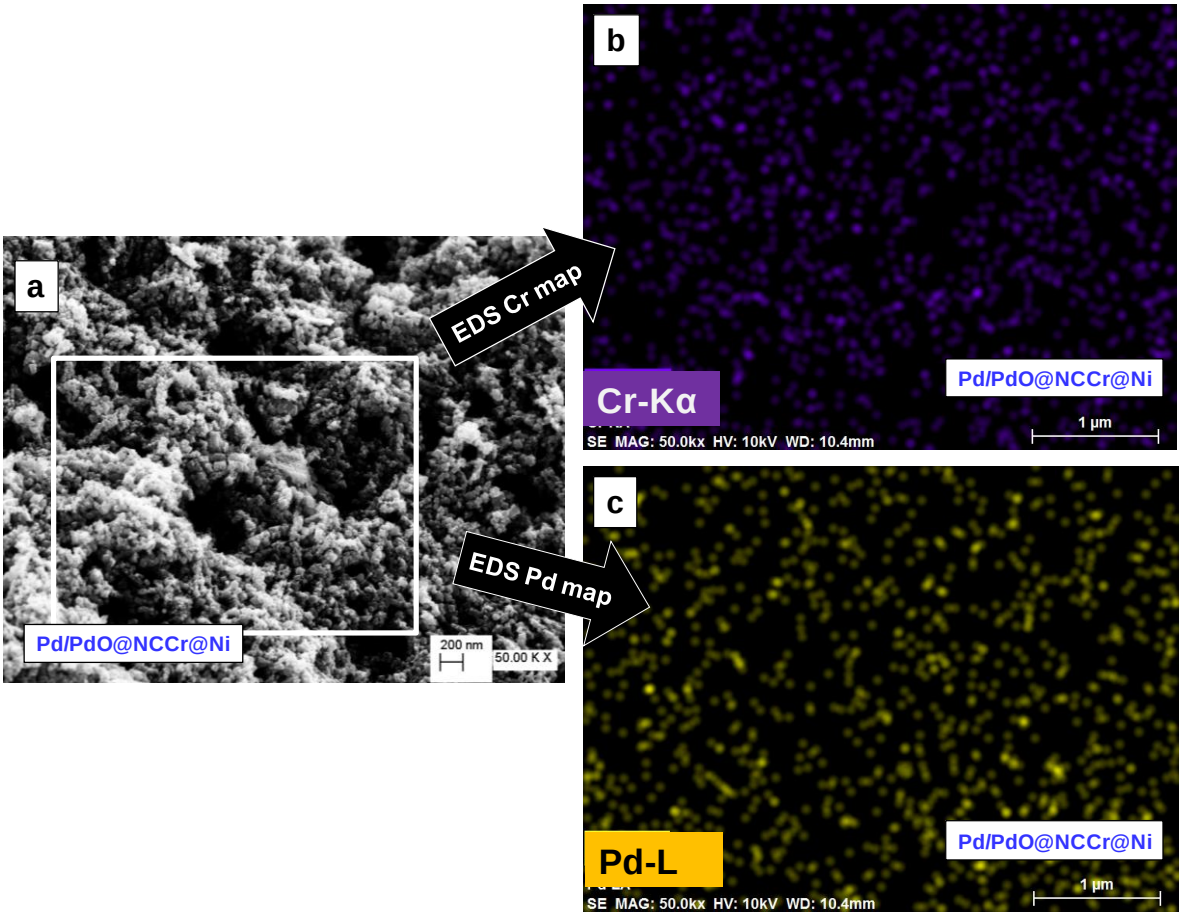

Figure 58. (a) Surface analysis by SEM and (b-c) EDS maps (Cr-Kα and the Pd-L emissions of the area highlighted) of the Pd/PdO@NCCr@Ni sample.

The XPS characterization of the Pd/PdO@NCCr@Ni pristine electrode is shown in Figure 59.

The profiles of the Ni $2p_{3/2}$ (Figure 59 a) and the Co $2p_{3/2}$ (Figure 59 b) regions were fully compatible with already reported data on cobaltite-type compounds[59,132] and with those recorded by us for the NCCr@Ni bare material (see Figures 44 b and 45 b).[124]

Moreover, both the relative distances between the six peaks introduced in the Ni $2p_{3/2}$ photoionization region and the five signals observed in the Co $2p_{3/2}$ one (Table 17) were in agreement to those reported in literature for NiO and Co_3O_4 samples[130,131,135,139] and with those registered by us for the bare sample (see Tables 10 and 11).

Overall, the analysis of the Ni 2p and Co 2p region suggested that the deposition of the Pd NP and the subsequent calcination leaved unaltered the electronic structure of the Cr(III)-doped $NiCo_2O_4$ material.

As in the case of the NCCr@Ni electrode, the low S/N ratio prevented a full reconstruction of the Cr 2p photoemission region for the Pd/PdO@NCCr@Ni one (Figure 59 c). However, the position (575–579 eV for the $2p_{3/2}$ peak) of the spin–orbit components, broadened due to multiplet splitting, was compatible with the incorporation of Cr(III) ions within the cobaltite spinel lattice.[135]

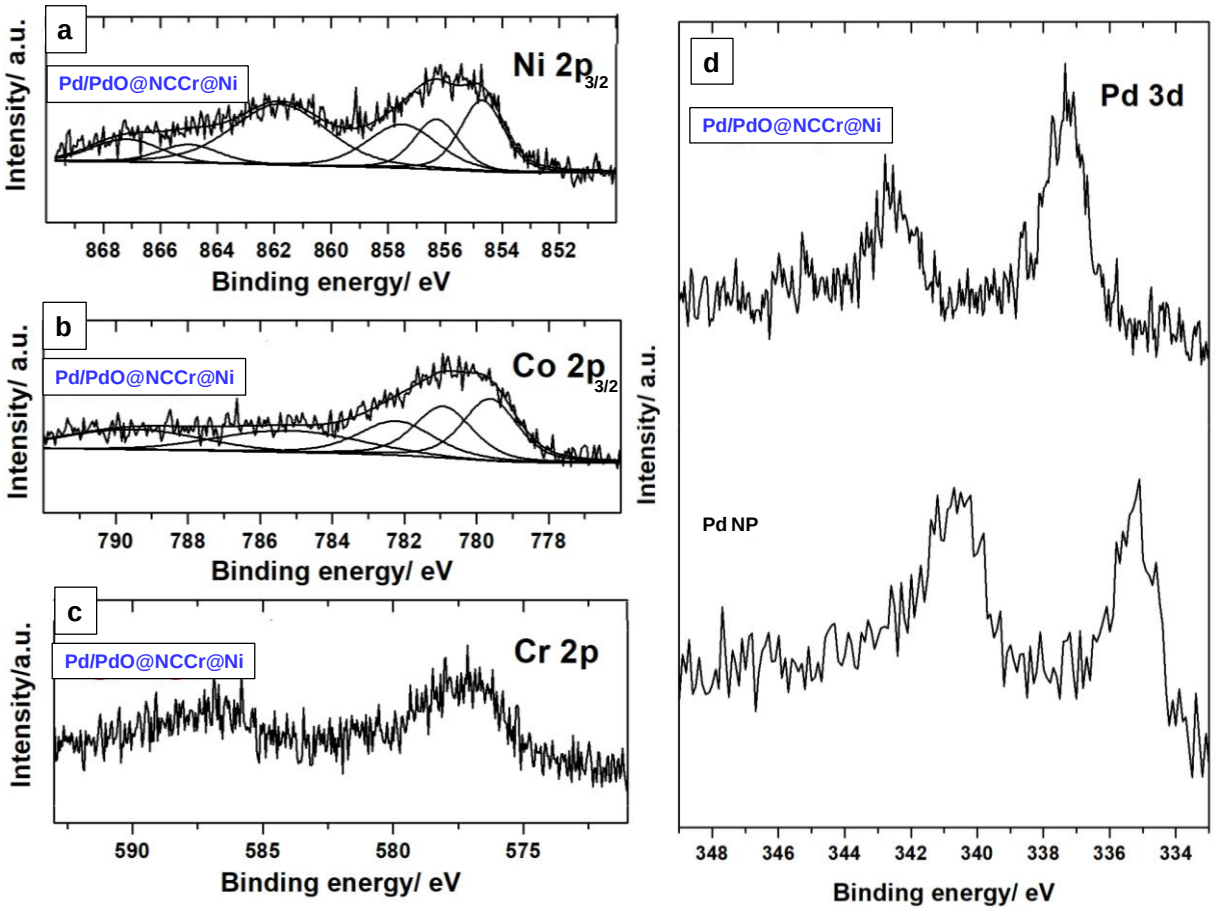

Figure 59. (a) Ni $2p_{3/2}$, (b) Co $2p_{3/2}$, (c) Cr 2p and (d) Pd 3d regions of the XP spectra for the Pd/PdO@NCCr@Ni pristine electrode. In (d) the Pd 3d region is also shown for the Pd NP.

Peak	BE position (eV)	Assignments
Ni $2p_{3/2}$	854.7	$\underline{c}d^9\underline{L}$
	856.3	d^8:$\underline{c}d^9\underline{L}$
	857.5	$\underline{c}d^9$:d^7 non-local screening
	861.8	$\underline{c}d^{10}\underline{L}^2$
	865.0	$\underline{c}d^8$
	867.2	shake-up satellite
Co $2p_{3/2}$	779.6	Co^{3+} $\underline{c}d^7\underline{L}$
	780.9	Co^{2+} $\underline{c}d^8\underline{L}$
	782.2	Co^{2+} $\underline{c}d^9\underline{L}^2$
	785.2	Co^{2+} $\underline{c}d^7$ (shake-up satellite)
	789.5	Co^{3+} $\underline{c}d^7$ (shake-up satellite)

Table 17. BE positions and assignments for the peaks determined after curve fitting of the experimental Ni $2p_{3/2}$ and Co $2p_{3/2}$ spectra of the Pd/PdO@NCCr@Ni pristine electrode.

The comparison between the Pd 3d XP spectra of the palladium nanoparticles deposited on a silicon wafer directly from the acetone suspension (lower spectrum, no calcination at 300°C) and the Pd/PdO@NCCr@Ni sample (upper spectrum) is shown in Figure 59 d. The absolute positions (i.e. about 335.4 eV and 337.4 eV for the $3d_{5/2}$ peaks, respectively) and the spin-orbit coupling separation (i.e. 5.4 eV and 5.2 eV, respectively) of the peaks were in good agreement with those reported for Pd and PdO samples for the pristine palladium nanoparticles and the Pd/PdO@NCCr@Ni sample, respectively.[146,147] Therefore XPS results highlighted the presence of a layer of metal oxide, few nanometers thick, on the Pd NP surface on the Pd/PdO@NCCr@Ni sample whereas the pristine nanoparticles surface was purely metallic. Apparently, after the dispersion onto the mixed oxide substrate, the outer layers of the Pd NP oxidized, likely during the calcination at 300 °C. Being the core structure of the nanoparticles after deposition/calcination still constituted by metallic Pd (see Figures 55 a and 57), the resulting co-catalyst dispersed onto the surface of the Pd decorated electrode was therefore constituted by Pd/PdO nanoparticles, likely with a core-shell nano-morphology. This was the reason why, from the beginning to the end of the text describing this work, we referred to this composite cathode with the name Pd/PdO@NCCr@Ni.

7.4.2. Post-mortem cathodes

Pd/PdO@NCCr@Ni and bare NCCr@Ni cathodes extracted from cells discharged to 2.0 V and cycled between 2.0 and 4.1 V at J = 0.05 mA cm^{-2} and from a battery set to 100 cycles at J = 0.2 mA cm^{-2} limiting the capacity at 0.2 mAh cm^{-2} (see Figures 52 and 53 for the electrochemical performance) were analyzed ex-situ by means of XPS in order to compare the modification in their surface composition upon cycling and until the cell death.

For all the discharge and cycled samples, the **Ni 2p and Co 2p spectral regions** (data not shown) did not show any significant difference in terms of number and relative peaks positions respect to those recorded for the pristine materials (see Figures 44 and 45 for the NCCr@Ni and Figure 59 a-b for the Pd/PdO@NCCr@Ni pristine samples, respectively). Also the **Cr 2p and Pd 3d regions** were found to be similar.

The **C 1s photoemission regions** are reported in Figure 60 for all the samples.

As in our previous works on cobaltite-based samples (see chapters 5 and 6), the BE of the first peak belonging to the $–CH_2–$ groups of the aliphatic carbon contamination was reported at 284.8 eV and was used as an internal standard reference for the BE scale. Both pristine materials (spectra a) showed another peak related to oxidized functions (i.e. C-O, C-O-C etc) at the carbon surface (286.2-286.3 eV)[99]. A third signal for higher oxidized carbonaceous groups, possibly grown due to the X-ray exposition[99] (288.5 eV), was visible only for the Pd-decorated electrode. All the post-mortem cathodes (spectra b,c,d) showed additional features at 286.1-286.7 and 292.3-293.0 eV associated with ethereal C−O bonds in TEGDME[82,99] and with $−CF_3$ groups in $TFSI^-$ anion,[100,101] respectively.

Spectra b in Figure 60 highlight the effect of discharging the cells to 2.0 V at J = 0.05 mA cm^{-2}. According to our previous findings (see chapter 6, Figure 49 β, spectrum b), for the NCCr@Ni cathode (Figure 60 α, spectrum b) two signals associated with carboxylate and carbonate groups[82,99–103] appeared at 288.7 eV and 289.7 eV, respectively. Instead, on the Pd/PdO@NCCr@Ni electrode only carboxylates functions were detected at 288.6 eV (Figure 60 β, spectrum b). Similar pictures were observed on the surface of both materials on charge up to 4.1 V at J = 0.05 mA cm^{-2} (spectra c).

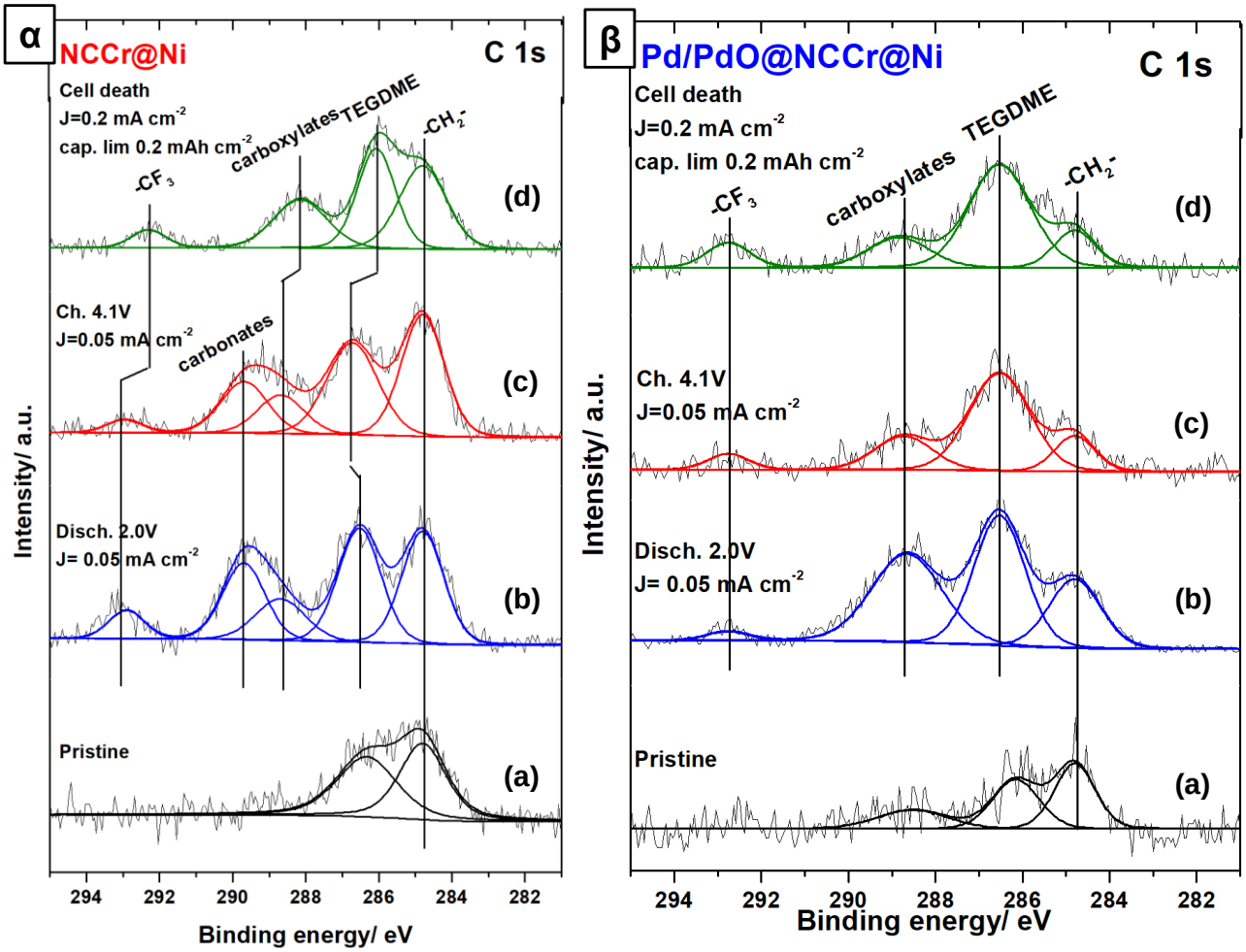

Figure 60. C 1s photoemission regions for (α) NCCr@Ni and (β) Pd/PdO@NCCr@Ni cathodes. For both materials, (a) are the pristine, (b) discharged and (c) cycled samples. (d) are cathodes extracted at the cycle of death from cells set to 100 cycles.

On the basis of literature reports[39] and our previous observations (see chapter 6), both carboxylates and carbonates were expected to grow as oxidative degradation products of the solvent TEGDME. The absence of carbonates on the Pd-decorated electrodes called for a possible solvent delayed degradation (i.e. stopped at a lower stage of oxidation) in presence of the Pd co-catalyst.

However, this difference in the composition of the deposits on the surface of the NCCr@Ni and the Pd/PdO@NCCr@Ni cathodes was not still visible at the cell death (spectra d). In fact, on both electrodes operated with the low capacity limitation of 0.2 mAh cm^{-2} solvent degradation probably did not proceed to the higher stage of oxidation of carbonates, being limited to that of carboxylates. Instead, a real spectral difference between the samples could be found in the intensification of the TEGDME peak for the Pd-decorated electrode and a slightly less intense carboxylates signal at the cell death. Generally speaking, an XPS component with a too large full-width-half-maximum can hide unresolved signals. In our case we speculated about additional components related to other less-oxidized degradation by-products (e.g. polyethers, epoxides etc.) grown onto the Pd/PdO@NCCr@Ni samples. The idea about the deactivation of both electrodes upon cycling due to the accumulation of degradation compounds was confirmed by the evolution of the signals in the metals characteristic photoemission regions (i.e. Ni 2p, Co 2p, Cr 2p and Pd 3d, data not shown) that were sensibly attenuated after cycling, particularly in the case of the NCCr@Ni one. In fact, the fitted Ni/C and Co/C atomic ratios remarkably decreased between pristine materials and those recuperated at the cell death of about 85% and 48% for the NCCr@Ni and the Pd/PdO@NCCr@Ni materials, respectively. This finding called for the formation of a thinner organic layer on the Pd/PdO decorated porous electrodes in agreement with the moderately lower intensity of the carboxylates.

Overall, on both electrodes a chemically similar organic film constituted by degradation products grew cycle-by-cycle, likely trapping LiTFSI and solvent molecules. This organic composite film passivated the metallic catalytic centers of both porous materials, thus leading to a progressive deterioration of the electro-catalytic properties and to the cell death. The improved calendar life recorded for the Pd/PdO@NCCr@Ni sample called for an enhancement of the ORR/OER selectivity. In fact, the Pd/PdO-decorated mixed oxide was apparently less active in the promotion of electro-active parasitic reactions, thus mitigating the deactivation of the electrode surface.

Li 1s spectra are shown in Figure 61 for all the samples. The occurrence of ORR/OER reactions was confirmed on both electrodes. In fact, we observed on discharge (spectra a) the appearance of a broad peak in the characteristic region for lithium oxides (55.2-55.3 eV).[82,104,107–109]

In the case of the Pd/PdO@NCCr@Ni material, after 1 full cycle (Figure 61 β, spectrum b) their complete disappearance was observed, whereas a minimal signal was possibly detected for the NCCr@Ni one. Although speculative, this finding could be a clue of an enhancement of the electro-catalysis in the OER provided by the composite electrode decorated with Pd nanoparticles in respect to that of the bare mixed oxide.

Both electrodes seemed free from lithium oxides deposits at the cell death (spectra c). Nevertheless, this finding could be dependent on the low S/N ratio in the Li 1s region due to the low orbital cross section at the working energy of the Al Kα radiation. In fact, upon acquiring the same region at the Elettra synchrotron with a radiation of hν=100 eV, from a cell cycled in similar conditions with a NCCr@Ni positive electrode we found residual signals for lithium oxides at cell death (see Figure 50 β, spectrum c).

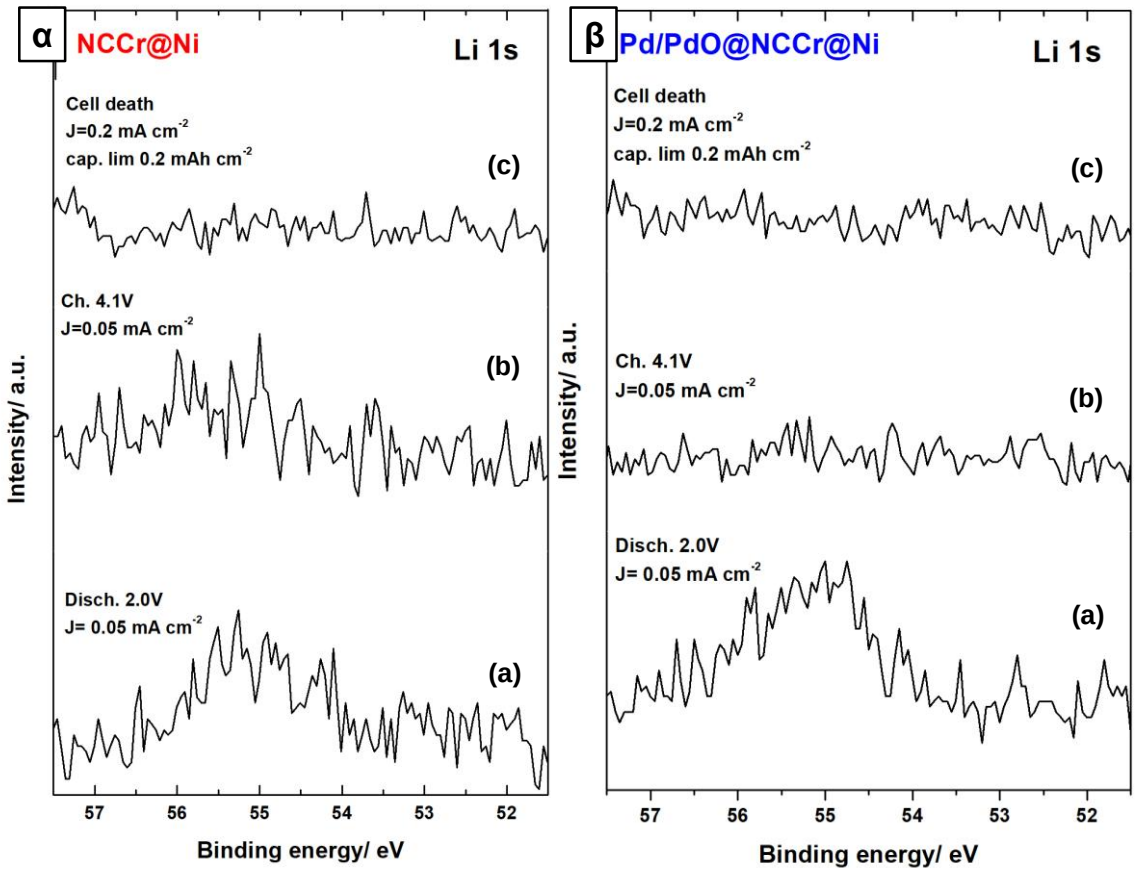

Figure 61. Li 1s photoemission regions for (α) NCCr@Ni and (β) Pd/PdO@NCCr@Ni cathodes. For both the materials, (a) the discharged and (b) cycled samples. (c) are cathodes extracted at the cycle of death from cells set to 100 cycles.

7.5. Conclusions

For the first time in the literature we synthesized palladium nanoparticles by means of pulsed laser ablation in liquid and applied them in Li-O_2 cells as co-catalyst after deposition by drop casting onto a positive electrode with a complete carbon-free configuration. In fact, we produced composed Pd/PdO@NCCr@Ni cathodes adopting a nanostructured Cr(III)-doped $NiCo_2O_4$ on Ni foam as active material.

Electrochemical tests confirmed the synergistic co-catalytic effect between the Pd NP and the doped nickel cobaltite, particularly in terms of reduced discharge and charge overvoltages and improved cell calendar life.

XPS data for the pristine Pd/PdO@NCCr@Ni cathode were compared to those for the bare NCCr@Ni one showing that these materials display analogous electronic structure and that Pd nanoparticles are constituted by a noble metal core covered by a shell of PdO.

Moreover, XPS post-mortem characterization of the electrodes recuperated from the dead cells suggested an increased selectivity towards the ORR/OER of the Pd-decorated cathode, that seemed able to mitigate the degradation of the TEGDME solvent upon cycling. Despite both Pd/PdO@NCCr@Ni and NCCr@Ni –based cells died because of deactivation of the active materials by accumulation of solvent by-products, this process appeared delayed when the Pd co-catalyst was adopted.

Final remarks

This work has been focused on aprotic Li-O_2 cells assembled with different cathode materials in combination with the ether-based LiTFSI/TEGDME electrolyte. The performance of these promising energy storage systems have been investigated and related to the electrochemical and chemical processes at the triple O_2/cathode/electrolyte interface and to the peculiar influence of each type of cathode material. These goals have been achieved by a powerful combination of techniques such as X-ray Diffraction (XRD), Fourier Transform Infrared Spectroscopy (FTIR), Scanning Electron Microscopy (SEM), Transmission Electron Microscopy (TEM) and X-ray Photoelectron Spectroscopy (XPS).

The remarkable role of the $TFSI^-$ anion in the degradation process of a carbon-based cathode has been discussed in **Chapter 4** on the basis of a *post-mortem* characterization of the positive electrode. Moreover, the fade of long-term stability of the cells has been related to the accumulation on the cathode surface of both insulating reaction products and by-products, leading to the rise of overvoltages upon discharge and charge.

A full electrochemical and chemical characterization of novel carbon-free M^{n+}-doped (M^{n+}=Cr^{3+} and Zn^{2+}) $NiCo_2O_4$ nanomaterials grown on Ni foam (NCCr@Ni and NCZn@Ni) has been reported in **Chapters 5 and 6**. For the first time in the literature these materials have been tested as cathodes in Li-O_2 cells and the beneficial effect of Cr(III)- and Zn(II)-doping of the $NiCo_2O_4$ spinel to boost the kinetics of both the ORR and the OER has been demonstrated. By means of in-house and synchrotron measurements the dopants role in the increase of the performance respect to the undoped material has been investigated.

The preparation and characterization of novel composite Pd/PdO@NCCr@Ni cathodes made of Pd nanoparticles deposited on a nanostructured Cr(III)-doped $NiCo_2O_4$ on Ni foam has been described in **Chapter 7**. The synergistic co-catalytic effect between the Pd NP and the doped nickel cobaltite has been proved to reduce both discharge and charge overvoltages and to improve the cell calendar life.

Overall, the general objectives of the PhD activity have been met, since three novel materials have been produced and demonstrated to be performing cathodes for Li-O_2 cells. Moreover, this study allowed the acquisition of skills concerning laboratory practice and widely applicable electrochemical and chemical characterization techniques.

Going beyond the temporal limits of the PhD, this work opens the door to a deeper investigation upon the dopants action in the ORR and OER electrochemical paths. To reach this goal, our research group is planning the realization of X-ray Absorption Spectroscopy (XAS), Extended X-ray Absorption Fine Structure (EXAFS) and magnetic measurements on both pristine and post-mortem nickel cobaltite-based

electrodes. Particularly, the acquisition of the XAS metal edges could give information about the pristine states of oxidation of the transition metals and their possible modification upon cycling. The analysis of the EXAFS region of the absorption spectra could outline a portrait of the metal cations environment both in the pristine and the post-mortem cathodes structure. Finally, the possible influence of the magnetic properties of the cathodes surface on the ORR/OER processes could be elucidated by means of magnetic tests.

Bibliography

1. Imanishi, N., Luntz, A. C. & Bruce, P. The lithium air battery: Fundamentals. (2014).
2. Lu, J., Li, L., Park, J.-B., Sun, Y.-K., Wu, F. & Amine, K. Aprotic and Aqueous Li-O_2 Batteries. *Chem. Rev*. **11**, 5611-5640 (2014).
3. Feng, N., He, P. & Zhou, H. Critical Challenges in Rechargeable Aprotic Li-O_2 Batteries. *Adv. Energy Mater*.**6**, 1–24 (2016).
4. Sharon, D., Hirshberg, D., Afri, M., Frimer, A. A., Noked, M. & Aurbach D. Aprotic metal-oxygen batteries: recent findings and insights. *Journal of Solid State Electrochemistry* **21**, 1861-1878 (2017).
5. Bruce, P. G., Freunberger, S. A., Hardwick, L. J. & Tarascon, J.-M. Li-O_2 and Li-S batteries with high energy storage. *Nat. Mater*.**11**, 19–29 (2012).
6. Schwenke, K. U., Metzger, M., Restle, T., Piana, M. & Gasteiger, H. A. The Influence of Water and Protons on Li_2O_2 Crystal Growth in Aprotic Li-O_2 Cells. *J. Electrochem. Soc.* **162**, A573–A584 (2015).
7. Meini, S., Piana, M., Tsiouvaras, N., Garsuch, A. & Gasteiger, H. A. The effect of water on the discharge capacity of a non-catalyzed Carbon cathode for Li-O_2 batteries. *Electrochem. Solid-State Lett.***15**, A45–A48 (2012).
8. Gowda, S. R., Brunet, A., Wallraff, G. M. & McCloskey, B. D. Implications of CO_2 Contamination in Rechargeable Nonaqueous Li–O_2 Batteries. *J. Phys. Chem. Lett.***4**, 276–279 (2013).
9. Bhatt, M. D., Geaney, H., Nolan, M. & O'Dwyer, C. Key scientific challenges in current rechargeable non-aqueous Li-O_2 batteries: experiment and theory. *Phys. Chem. Chem. Phys*.**16**, 12093–130 (2014).
10. Wood, K. N., Noked, M. & Dasgupta, N. P. Lithium Metal Anodes: Toward an Improved Understanding of Coupled Morphological, Electrochemical, and Mechanical Behavior. *ACS Energy Letters* **3**, 664-672 (2017).
11. Kazyak, E., Wood, K. N. & Dasgupta, N. P. Improved Cycle Life and Stability of Lithium Metal Anodes through Ultrathin Atomic Layer Deposition Surface Treatments. *Chem. Mater.* **18**, 6457-6462 (2015).
12. Peng, Z., Freunberger, S. A., Hardwick, L. J., Chen, Y., Giordani, V., Bardé, F., Novák, P., Graham, D., Tarascon, J.-M. & Bruce, P. G. Oxygen reactions in a non-aqueous Li^+ electrolyte. *Angew. Chemie - Int. Ed.* **50**, 6351-6355 (2011).
13. Yang, J., Zhai, D., Wang, H.-H., Lau, K. C., Schlueter, J. A., Du, P., Myers, D. J., Sun, Y.-K., Curtiss, L. A. & Amine, K. Evidence for lithium superoxide-like species in the discharge product of a Li-O_2 battery. *Phys. Chem. Chem. Phys*. **15**, 3764-3771 (2013).
14. Zhai, D.,Wang, H. H., Yang, J., Lau, K. C., Li, K., Amine, K. & Curtiss, L. A. Disproportionation in Li–O_2 Batteries Based on a Large Surface Area Carbon Cathode. *J. Am. Chem. Soc.* **41**, 15364-15372 (2013).
15. Lu, Y. C. & Shao-Horn, Y. Probing the reaction kinetics of the charge reactions of nonaqueous Li-O_2

batteries. *J. Phys. Chem. Lett*. **4**, 93–99 (2013).

16. Girishkumar, G., McCloskey, B., Luntz, A. C., Swanson, S. & Wilcke, W. Lithium-air battery: Promise and challenges. *J. Phys. Chem. Lett.***14**, 2193-2203 (2010).
17. Aravindan, V., Gnanaraj, J., Madhavi, S. & Liu, H. K. Lithium-ion conducting electrolyte salts for lithium batteries. *Chemistry - A European Journal* **17**, 14326-14346 (2011).
18. Du, P., Lu, J., Lau, K. C., Luo, X., Bareno, J., Zhang, X., Ren, Y., Zhang, Z., Curtiss, L. A., Sun, Y.-K. & Amine, K. Compatibility of lithium salts with solvent of the non-aqueous electrolyte in Li-O_2 batteries. *Phys. Chem. Chem. Phys.* **15**, 5572 (2013).
19. Giacco, D., Carboni, M., Brutti, S. & Marrani, A. G. Noticeable role of $TFSI^-$ anion in the carbon cathode degradation of Li-O_2 cells. *ACS Appl. Mater. Interfaces* **37**, 31710-31720 (2017).
20. Khetan, A., Luntz, A. & Viswanathan, V. Trade-offs in capacity and rechargeability in nonaqueous Li-O_2 batteries: Solution-driven growth versus nucleophilic stability. *J. Phys. Chem. Lett.* **7**, 1254-1259 (2015).
21. Knudsen, K. B., Vegge, T., McCloskey, B. D. & Hjelm, J. An Electrochemical Impedance Spectroscopy Study on the Effects of the Surface- and Solution-Based Mechanisms in Li-O_2 Cells. *J. Electrochem. Soc.* **163**, A2065–A2071 (2016).
22. Zhang, Y., Zhang, X., Wang, J., McKee, W. C., Xu, Y. & Peng, Z. Potential-Dependent Generation of O_2^- and LiO_2 and Their Critical Roles in O_2 Reduction to Li_2O_2 in Aprotic Li-O_2 Batteries. *J. Phys. Chem. C* **120**, 3690–3698 (2016).
23. Griffith, L. D., Sleightholme, A. E. S., Mansfield, J. F., Siegel, D. J. & Monroe, C. W. Correlating Li/O_2cell capacity and product morphology with discharge current. *ACS Appl. Mater. Interfaces* **7**, 7670–7678 (2015).
24. Lau, S. & Archer, L. A. Nucleation and Growth of Lithium Peroxide in the Li-O_2 Battery. *Nano Lett.* **15**, 5995–6002 (2015).
25. Sharon, D., Hirsberg, D., Salama, M., Afri, M., Frimer, A. A., Noked, M., Kwak, W., Sun, Y.-K. & Aurbach, D. Mechanistic Role of Li^+ Dissociation Level in Aprotic Li-O_2 Battery. *ACS Appl. Mater. Interfaces* **8**, 5300–5307 (2016).
26. Johnson, L., Li, C., Liu, Z., Chen, Y., Freunberger, S. A., Ashok, P. C., Pravee, B. B., Dholakia, K., Tarascon, J.-M. & Bruce, P. G. The role of LiO_2 solubility in O_2 reduction in aprotic solvents and its consequences for Li-O_2 batteries. *Nat. Chem.* **6**, 1091–9 (2014).
27. Xu, J.-J.,Chang, Z. W., Wang, J., Liu, D.-P., Zhang, Y. & Zhang, X.-B. Cathode Surface-Induced, Solvation-Mediated, Micrometer-Sized Li_2O_2 Cycling for Li-O_2 Batteries. *Adv. Mater.* **28**, 9620-9628 (2016).
28. Mahne, N., Fontaine, O., Ottakam Thotiyl, M. M., Wilkening, M. & Freunberger, S. A. Mechanism and performance of lithium-oxygen batteries – a perspective. *Chem. Sci.* **8**, 6716–6729 (2017).
29. Shen, X., Liu, H., Cheng, X.-B., Yan, C. & Huang, J.-Q. Beyond lithium ion batteries: Higher energy density battery systems based on lithium metal anodes. *Energy Storage Mater.* **12**, 161-175 (2018).

30. Eftekhari, A. & Ramanujam, B. In pursuit of catalytic cathodes for lithium–oxygen batteries. *J. Mater. Chem. A* **5**, 7710–7731 (2017).
31. Adams, B. D., Black, R., Williams, Z., Fernandes, R., Cuisiniere, M., Berg, E. J., Novak, P., Murphy, G. K. & Nazar, L. F. Towards a Stable Organic Electrolyte for the Lithium Oxygen Battery. *Adv. Energy Mater.* **5**, 1400867 (2015).
32. Mahne, N.,Schafzahl, B., Leypold, C., Leypold, M., Grumm, S., Leitgeb, A., Strohmeier, G. A., Wilkening, M., Fontaine, O., Kramer, D., Slugovc, C., Borisov, S. M. & Freunberger, S. A. Singlet oxygen generation as a major cause for parasitic reactions during cycling of aprotic lithium-oxygen batteries. *Nat. Energy* **2**, 17036 (2017).
33. Bruce, P. G., Freunberger, S. A., Hardwick, L. J. & Tarascon, J.-M. Li–O_2 and Li–S batteries with high energy storage. *Nat. Mater.* **11**, 19-29 (2012).
34. Tu, Y., Deng, D. & Bao, X. Nanocarbons and their hybrids as catalysts for non-aqueous lithium-oxygen batteries. *Journal of Energy Chemistry* **25**, 957-966 (2016).
35. Woo, H., Joonhyeon, K., Jaewook, K., Chunjoong, K., Seunghoon, N. & Byungwoo, P. Development of carbon-based cathodes for Li-air batteries: Present and future. *Electronic Materials Letters* **12**, 551-567 (2016).
36. Carboni, M., Marrani, A. G., Spezia, R. & Brutti, S. Degradation of LiTfO / TEGME and LiTfO / DME Electrolytes in Li-O_2 Batteries. *J. Electrochem. Soc.* **165**, 1–9 (2018).
37. Carboni, M., Brutti, S. & Marrani, A. G. Surface Reactivity of a Carbonaceous Cathode in a Lithium Triflate/Ether Electrolyte-Based Li-O_2 Cell. *ACS Appl. Mater. Interfaces* **7**, 21751–21762 (2015).
38. Younesi, R., Hahlin, M., Treskow, M., Scheers, J., Johansson P.& Edström, K. Ether Based Electrolyte, $LiB(CN)_4$ Salt and Binder Degradation in the Li-O_2 Battery Studied by Hard X-ray Photoelectron Spectroscopy. *J. Phys. Chem. C* **116**, 18597–18604 (2012).
39. Younesi, R., Hahlin, M., Björefors, F., Johansson, P. & Edström, K. Li–O_2 Battery Degradation by Lithium Peroxide (Li_2O_2): A Model Study. *Chem. Mater.* **25**, 77–84 (2013).
40. Wen, Z., Shen, C. & Lu, Y. Air electrode for the lithium-air batteries: Materials and structure designs. *ChemPlusChem* **80**, 270-287 (2015).
41. Oh, D., Virwani, K., Tadesse, L., Jurich, M., Aetukuri, N., Thompson, L. E., Kim, H.-C. & Bethune, D. S. The Effect of Transition Metal Oxide Cathodes on the Oxygen Evolution Reaction in Li-O_2 Batteries. *J. Phys. Chem. C* **3**, 1404-1411 (2017).
42. Mohamed, S. G., Tsai, Y.-Q., Chen, C.-J., Tsai, Y.-T., Hung, T.-F., Chang, W.-S. & Liu, R.-S. Ternary Spinel MCo_2O_4 (M = Mn, Fe, Ni, and Zn) Porous Nanorods as Bifunctional Cathode Materials for Lithium-O_2 Batteries. *ACS Appl Mater Interfaces* **22**, 12038-12046 (2015).
43. Cui, Y., Wen, Z. & Liu, Y. A free-standing-type design for cathodes of rechargeable Li-O_2 batteries. *Energy Environ. Sci*. **4**, 4727-4734 (2011).
44. Cui, Y., Wen, Z., Sun, S., Lu, Y. & Jin, J. Mesoporous Co_3O_4 with different porosities as catalysts for the lithium-oxygen cell.*Solid State Ionics* **225**, 598-603 (2012).

45. Liu, Q. C., Xu, J. J., Chang, Z. W. & Zhang, X. B. Direct electrodeposition of cobalt oxide nanosheets on carbon paper as free-standing cathode for Li-O_2 battery. *J. Mater. Chem. A* **2**, 6081-6085 (2014).

46. Li, L., Shen, L., Nie, P., Pang, G., Wang, J., Li, H., Dong, S. & Zhang, X. Porous $NiCo_2O_4$ nanotubes as a noble-metal-free effective bifunctional catalyst for rechargeable Li–O_2 batteries. *J. Mater. Chem. A* **3**, 24309–24314 (2015).

47. Zhao, Q., Yan, Z., Chen, C. & Chen, J. Spinels: Controlled Preparation, Oxygen Reduction/Evolution Reaction Application, and beyond. *Chemical Reviews* **15**, 10121-10211 (2017).

48. Sun, B., Zhang, J., Munroe, P., Ahn, H.-J. & Wang, G. Hierarchical $NiCo_2O_4$ nanorods as an efficient cathode catalyst for rechargeable non-aqueous Li–O_2 batteries. *Electrochem. commun*. **31**, 88–91 (2013).

49. Liu, L., Wang, J., Hou, Y., Chen, J., Liu, H.-K., Wang, J. & Wu, Y. Self-Assembled 3D Foam-Like $NiCo_2O_4$ as Efficient Catalyst for Lithium Oxygen Batteries. *Small* **5**, 602-611 (2016).

50. Lin, X., Su, J., Li, L. & Yu, A. Hierarchical porous $NiCo_2O_4$@Ni as carbon-free electrodes for Lithium–oxygen batteries. *Electrochim. Acta* **168**, 292–299 (2015).

51. Jadhav, H. S., Kalubarme, R. S., Roh, J.-W., Jung, K.-N., Shin, K.-H., Park, C.-N. & Park C.-J. Facile and Cost Effective Synthesized Mesoporous Spinel $NiCo_2O_4$ as Catalyst for Non-Aqueous Lithium-Oxygen Batteries. *J. Electrochem. Soc.* **161**, A2188–A2196 (2014).

52. Zheng, Z. Bin, Chan, D. S. & Wu, M. S. Highly porous nickel cobaltite film composed of nanosheets with attached nanowires as an electrode material for electrochemical capacitors. *Mater. Lett*. **169**, 46-49 (2016).

53. Ezeigwe, E. R., Khiew, P. S., Siong, C. W. & Tan, M. T. T. Solvothermal synthesis of $NiCo_2O_4$ nanocomposites on liquid-phase exfoliated graphene as an electrode material for electrochemical capacitors. *J. Alloys Compd*. **693**, 1133-1142 (2017).

54. Li, Y., Hasin, P. & Wu, Y. $Ni_xCo_{3-x}O_4$ nanowire arrays for electrocatalytic oxygen evolution. *Adv. Mater.* **22**, 1926-1929 (2010).

55. Lu, B., Cao, D., Wang, P., Wang, G. & Gao, Y. Oxygen evolution reaction on Ni-substituted Co_3O_4 nanowire array electrodes. *Int. J. Hydrogen Energy* **36**, 72-78 (2011).

56. Sadighi, Z., Huang, J., Qin, L., Yao, S., Cui, J. & Kim, J.-K. Positive role of oxygen vacancy in electrochemical performance of $CoMn_2O_4$ cathodes for Li-O_2 batteries. *J. Power Sources* **365**, 134–147 (2017).

57. Marco, J. F., Gancedo, J. R., Gracia, M., Gautier, J. L., Ríos E. &Berry, E. F. Characterization of the nickel cobaltite, $NiCo_2O_4$, prepared by several methods: An XRD, XANES, EXAFS, and XPS study. *J. Solid State Chem*. **153**, 74-81 (2000).

58. Lenglet, M., Guillamet, R., Dürr, J., Gryffroy, D. & Vandenberghe, R. E. Electronic structure of $NiCo_2O_4$ by XANES, EXAFS and ^{61}Ni Mössbauer studies. *Solid State Commun*. **74**, 1035-1039 (1990).

59. Marco, J. F., Gancedo, J. R., Gracia, M., Gautier, J. L., Ríos, E. I., Palmer, H. M., Greaves, C. & Berry, F. J. Cation distribution and magnetic structure of the ferrimagnetic spinel $NiCo_2O_4$. *J. Mater. Chem.* **11**, 3087-3093 (2001).

60. Wang, Q., Liu, B., Wang, X., Ran, S., Wang, L., Chen, D. & Shen, G. Morphology evolution of urchin-like $NiCo_2O_4$ nanostructures and their applications as pseudocapacitors and photoelectrochemical cells. *J. Mater. Chem.* **22**, 21647-21653 (2012).

61. Li, L., Peng, S., Cheah, Y., Teh, P., Wang, J., Wee, G., Ko, Y., Wong, C. & Srinivasan, M. Electrospun porous $NiCo_2O_4$ nanotubes as advanced electrodes for electrochemical capacitors. *Chem. - A Eur. J.***19**, 5892-5898 (2013).

62. Nguyen, V. H. & Shim, J. J. Microwave-assisted synthesis of porous nickel cobaltite with different morphologies in ionic liquid and their application in supercapacitors. *Mater. Chem. Phys.* **176**, 6-11 (2016).

63. Silambarasan, M., Ramesh, P. S. & Geetha, D. Facile one-step synthesis, structural, optical and electrochemical properties of $NiCo_2O_4$ nanostructures. *J. Mater. Sci. Mater. Electron.* **28**, 323-336 (2016).

64. Lapham, D. P. & Tseung, A. C. C. The effect of firing temperature, preparation technique and composition on the electrical properties of the nickel cobalt oxide series $Ni_xCo_{1-x}O_y$. *J. Mater. Sci.* **39**, 251-264 (2004).

65. Bai, Y., Wang, R., Lu, X., Sun, J. & Gao, L. Template method to controllable synthesis 3D porous $NiCo_2O_4$ with enhanced capacitance and stability for supercapacitors. *J. Colloid Interface Sci.* **468**, 1-9 (2016).

66. Zhang, L., Zheng, W., Jiu, H., Ni, C., Chang, J. & Qi, G. The synthesis of NiO and $NiCo_2O_4$ nanosheets by a new method and their excellent capacitive performance for asymmetric supercapacitor. *Electrochim. Acta* **215**, 212-222 (2016).

67. Gupta, V., Gupta, S. & Miura, N. Electrochemically synthesized nanocrystalline spinel thin film for high performance supercapacitor. *J. Power Sources* **195**, 3757-3760 (2010).

68. Lu, B., Cao, D., Wang, P., Wang, G. & Gao, Y. Oxygen evolution reaction on Ni-substituted Co_3O_4 nanowire array electrodes. *Int. J. Hydrogen Energy* **36**, 72-78 (2011).

69. Shen, C., Wen, Z., Wang, F., Rui, K., Lu, Y. & Wu, X. Wave-like free-standing $NiCo_2O_4$ cathode for lithium-oxygen battery with high discharge capacity. *J. Power Sources* **294**, 593-601 (2015).

70. Liu, X., Wang, D. & Shi, S. Exploration on the possibility of Ni foam as current collector in rechargeable lithium-air batteries. *Electrochim. Acta* **87**, 865-871 (2013).

71. Lu, Y. C., Xu, Z., Gasteiger, H. A., Chen, S., Schifferli, K. H. & Shao-Horn, Y. Platinum-gold nanoparticles: A highly active bifunctional electrocatalyst for rechargeable lithium-air batteries. *J. Am. Chem. Soc.* **132**, 12170-12171 (2010).

72. Gittleson, F. S., Sekol, R. C., Doubek, G., Linardi, M. & Taylor, A. D. Catalyst and electrolyte synergy in Li-O_2 batteries. *Phys. Chem. Chem. Phys.***16**, 3230-3237 (2014).

73. Kumar, S., Selvaraj, C., Scanlon, L. G. & Munichandraiah, N. Ag nanoparticles-anchored reduced graphene oxide catalyst for oxygen electrode reaction in aqueous electrolytes and also a non-aqueous electrolyte for Li-O_2 cells. *Phys. Chem. Chem. Phys.***16**, 22830-22840 (2014).

74. Yadegari, H., Banis, M. N., Lushington, A., Sun, Q., Li, R., Sham, T.-K. & Sun, X. A bifunctional solid state catalyst with enhanced cycling stability for Na and Li-O_2 cells: Revealing the role of solid state catalysts. *Energy Environ. Sci*. **10**, 286-295 (2017).

75. Yang, H., Xia, J., Bromberg, L., Dimitrov, N. & Whittingham, M. S. Electrochemically synthesized nanoporous gold as a cathode material for Li-O_2 batteries. J. *Solid State Electrochem.* **21**, 463-468 (2017).

76. Agyeman, D. A., Park, M. & Kang, Y. M. Pd-Impregnated $NiCo_2O_4$ nanosheets/porous carbon composites as a free-standing and binder-free catalyst for a high energy lithium-oxygen battery. *J. Mater. Chem. A* **5**, 22234-22241 (2017).

77. Abràmoff, M. D., Magalhães, P. J. & Ram, S. J. Image processing with imageJ. *Biophotonics International* **11**, 36-42 (2004).

78. Soavi, F., Ruggeri, I. & Arbizzani, C. Design study of a novel, semi-solid Li/O_2 redox flow battery. *ECS Transactions* **72**, 1-9 (2016).

79. Zhang, Z. & Wang, Q. The New Method of XRD Measurement of the Degree of Disorder for Anode Coke Material. *Crystals* **7**, 5 (2017).

80. Schwenke, K. U., Meini, S., Wu, X., Gasteiger, H. A. & Piana, M. Stability of superoxide radicals in glyme solvents for non-aqueous Li-O_2 battery electrolytes. *Phys. Chem. Chem. Phys.* **15**, 11830-11839 (2013).

81. Freunberger, S. A., Chen, Y., Drewett, N. E., Hardwick, L. J., Bardé, F. & Bruce, P. G. The lithium-oxygen battery with ether-based electrolytes. *Angew. Chemie - Int. Ed.* **50**, 8609–8613 (2011).

82. Verma, P., Maire, P. & Novák, P. A review of the features and analyses of the solid electrolyte interphase in Li-ion batteries. *Electrochim. Acta* **55**, 6332–6341 (2010).

83. Sharon, D., Hirsberg, D., Afri, M., Garsuch, A., Frimer, A. A. & Aurbach, D. Reactivity of amide based solutions in lithium-oxygen cells. *J. Phys. Chem. C* **118**, 15207–15213 (2014).

84. Cheng, H., Zhu, C., Lu, M. & Yang, Y. Spectroscopic and electrochemical characterization of the passive layer formed on lithium in gel polymer electrolytes containing propylene carbonate. *J. Power Sources* **173**, 531–537 (2007).

85. Mizuno, F., Nakanishi, S., Kotani, Y., Yokoishi, S. & Iba, H. Rechargeable Li-Air Batteries with Carbonate-Based Liquid Electrolytes. *Electrochemistry* **78**, 403–405 (2010).

86. Xiao, J., Hu, J., Wang, D., Hu, D., Xu, W., Graff, G. L., Nie, Z., Liu, J. & Zhang, J.-G. Investigation of the rechargeability of Li-O_2 batteries in non-aqueous electrolyte. *J. Power Sources* **196**, 5674–5678 (2011).

87. Veith, G. M., Dudney, N. J., Howe, J. & Nanda, J. Spectroscopic characterization of solid discharge products in li-air cells with aprotic carbonate electrolytes. *J. Phys. Chem. C* **115**, 14325–14333

(2011).

88. Brooker, M. H. & Bates, J. B. Raman and Infrared spectral studies of anhydrous Li_2CO_3 and Na_2CO_3. *J. Chem. Physics.* **54**, 4788–4796 (1971).

89. Li, L. F., Xi, B., Lee, H. S., Li, H., Yang, X. Q., McBreen, J. & Huang, X. J. Studies on the enhancement of solid electrolyte interphase formation on graphitized anodes in LiX-carbonate based electrolytes using Lewis acid additives for lithium-ion batteries. *J. Power Sources* **189**, 539–542 (2009).

90. Robledo, C. B., Thomas, J. E., Luque, G., Leiva, E. P. M., Cámar, O., Barraco, D. & Visintin, A. An experimental and theoretical approach on the effect of presence of oxygen in milled graphite as lithium storage material. *Electrochim. Acta* **140**, 152–159 (2014).

91. Wu, X., Xu, H., Shen, Y., Xu, P., Lu, L., Fu, J. & Zhao, H. Treatment of graphite felt by modified Hummers method for the positive electrode of vanadium redox flow battery. *Electrochim. Acta* **138**, 264–269 (2014).

92. Ulaganathan, M., Nithya, R., Rajendran, S. & Raghu, S. Li-ion conduction on nanofiller incorporated PVdF-co-HFP based composite polymer blend electrolytes for flexible battery applications. *Solid State Ionics* **218**, 7–12 (2012).

93. Bormashenko, Y., Pogreb, R., Stanevsky, O. & Bormashenko, E. Vibrational spectrum of PVDF and its interpretation. *Polym. Test.* **23**, 791–796 (2004).

94. Matsuta, S., Asada, T. & Kitaura, K. Vibrational assignments of lithium alkyl carbonate and lithium alkoxide in the infrared spectra, an Ab Initio MO study. *J. Electrochem. Soc*. **147**, 1695–1702 (2000).

95. Nansé, G., Papirer, E., Fioux, P., Moguet, F. & Tressaud, A. Fluorination of carbon blacks: An X-ray photoelectron spectroscopy study: I. A literature review of XPS studies of fluorinated carbons. XPS investigation of some reference compounds. *Carbon N. Y.* **35**, 175–194 (1997).

96. Speranza, G. & Minati, L. The surface and bulk core lines in crystalline and disordered polycrystalline graphite.*Surf. Sci.* **600**, 4438–4444 (2006).

97. Hunt, M. R. C. Surface and bulk components in angle-resolved core-level photoemission spectroscopy of graphite. *Phys. Rev. B - Condens. Matter Mater. Phys.***78**, 1–4 (2008).

98. Estrade-Szwarckopf, H. XPS photoemission in carbonaceous materials: A 'defect' peak beside the graphitic asymmetric peak. *Carbon N. Y.***42**, 1713–1721 (2004).

99. Briggs, D. & Seah, M. P. Practical surface analysis. (1990).

100. Ensling, D., Stjerndahl, M., Nytén, A., Gustafsson, T. & Thomas, J. O. A comparative XPS surface study of Li_2FeSiO_4/C cycled with LiTFSI- and $LiPF_6$ -based electrolytes. *J. Mater. Chem.* **19**, 82–88 (2009).

101. Veith, G. M., Nanda, J., Delmau, L. H. & Dudney, N. J. Influence of Lithium Salts on the Discharge Chemistry of Li − Air Cells. *J. Phys. Chem. Lett*. **3**, 1242–1247 (2012).

102. Lu, Y.-C., Crumlin, E. J., Carney, T. J., Baggetto, L., Veith, G. M., Dudney, N. J., Liu, Z. & Shao-Horn, Y. Influence of Hydrocarbon and CO_2 on the Reversibility of Li–O_2 Chemistry Using In Situ

Ambient Pressure X-ray Photoelectron Spectroscopy. *J. Phys. Chem. C* **117**, 25948–25954 (2013).

103. Younesi, R., Urbonaite, S., Edström, K. & Hahlin, M. The cathode surface composition of a cycled Li-O_2 battery: A Photoelectron spectroscopy study. *J. Phys. Chem. C* **116**, 20673–20680 (2012).
104. Martin, L., Martinez, H., Poinot, D., Pecquenard, B. & Le Cras, F. Comprehensive X-ray photoelectron spectroscopy study of the conversion reaction mechanism of CuO in lithiated thin film electrodes.*J. Phys. Chem. C* **117**, 4421–4430 (2013).
105. Maibach, J., Lindgren, F., Eriksson, H., Edström, K. & Hahlin, M. Electric Potential Gradient at the Buried Interface between Lithium-Ion Battery Electrodes and the SEI Observed Using Photoelectron Spectroscopy. *J. Phys. Chem. Lett.***7**, 1775–1780 (2016).
106. Sun, B., Rehnlund, D., Lacey, M. J. & Brandell, D. Electrodeposition of thin poly(propylene glycol) acrylate electrolytes on 3D-nanopillar electrodes. *Electrochim. Acta* **137**, 320–327 (2014).
107. Zhai, D.,Wang, H.-H., Lau, K. C., Gao, J., Redfern, P. C., Kang, F., Li, B., Indacochea, E., Das, U., Sun, H.-H., Sun, H.-J., Amine, K. & Curtiss, L. A. Raman Evidence for Late Stage Disproportionation in a Li−O_2 Battery. *J. Phys. Chem. Lett.* **5**, 2705–2710 (2014).
108. Wu, Q. H., Thissen, A. & Jaegermann, W. Photoelectron spectroscopic study of Li oxides on Li over-deposited V_2O_5 thin film surfaces. *Appl. Surf. Sci.***250**, 57–62 (2005).
109. Kataev, E. Y., Itkis, D. M., Fedorov, A. V., Senkovsky, B. V., Usachov, D. Y., Verbitskiy, N. Y., Grüneis, A., Barinov, A., Tsukanova, D. Y., Volykhov, A. A., Mironovich, K. V., Krivchenko, V. A., Rybin, M. G., Obraztsova, E. D., Laubschat, C., Vyalikh, D. V. & Yashina, L. V. Oxygen reduction by lithiated graphene and graphene-based materials. *ACS Nano* **9**, 320-326 (2015).
110. Williams, M. The Direct Evaluation of Electronic Band Structures of Layered Solids Using Angle-Resolved Photoemission. *Il Nuovo Cimento B* **38**, 216–225 (1977).
111. Law, A. R., Barry, J. J. & Hughes, H. P. Angle-resolved photoemission and secondary electron emission from single-crystal graphite. *Phys. Rev. B* **28**, 5332–5335 (1983).
112. Kurisaki, T.,Tanaka, D., Inoue, Y., Wakita, H., Minofar, B., Fukuda, S., Ishiguro, S. & Umebayashi, Y. Surface Analysis of Ionic Liquids with and without Lithium Salt Using. *J. Phys. Chem. B* **116**, 10870–10875 (2012).
113. Krischok, S., Eremtchenko, M., Himmerlich, M., Lorenz, P., Uhlig, J., Neumann, A., Öttking, R., Beenken, W. J. D., Höfft, O., Bahr, S., Kempter, V. & Schaefer, J. A. Temperature-Dependent Electronic and Vibrational Structure of the 1-Ethyl-3-methylimidazolium Bis(trifluoromethylsulfonyl)amide Room-Temperature Ionic Liquid Surface: A Study with XPS, UPS, MIES and HREELS. *J. Phys. Chem. B* **111**, 4801–4806 (2007).
114. Iwahashi, T., Nishi, T., Yamane, H., Miyamae, T., Kanai, K., Seki, K., Kim, D. & Ouchi, Y. Surface Structural Study on Ionic Liquids Using Metastable Atom Electron Spectroscopy. *J. Phys. Chem. C* **113**, 19237–19243 (2009).
115. Dedryvère, R., Leroy, S., Martinez, H., Blanchard, F., Lemordant, D. & Gonbeau, D. XPS valence characterization of lithium salts as a tool to study electrode/electrolyte interfaces of Li-ion batteries. *J.*

Phys. Chem. B **110**, 12986–12992 (2006).

116. Leroy, S., Martinez, H., Dedryvère, R., Lemordant, D. & Gonbeau, D. Influence of the lithium salt nature over the surface film formation on a graphite electrode in Li-ion batteries: An XPS study. *Appl. Surf. Sci*. **253**, 4895–4905 (2007).
117. Thomas, S. & Sherwood, P. M. A. Valence band X-ray photoelectron spectroscopic studies of carbonate, bicarbonate and formate interpreted by Xα calculations. *Surf. Interface Anal*. **20**, 595–599 (1993).
118. Connor, J. A., Considine, M. & Hillier, I. H. Low energy photoelectron spectroscopy of solids. Photoelectron spectra of carbonate, phosphate, sulphate, triborate and ethanoate ions. *J. Chem. Soc., Faraday Trans*. **7**, 1285–1291 (1978).
119. Contarini, S. & Rabalais, J. W. Ion bombardment-induced decomposition of Li and Ba sulfates and carbonates studied by X-ray photoelectron spectroscopy. *J. Electron Spectros. Relat. Phenomena* **35**, 191-201 (1985).
120. Ensling, D., Thissen, A. & Jaegermann, W. On the formation of lithium oxides and carbonates on Li metal electrodes in comparison to $LiCoO_2$ surface phases investigated by photoelectron spectroscopy. *Appl. Surf. Sci.* **255**, 2517–2523 (2008).
121. Hasan, M., Newcomb, S. B., Rohan, J. F. & Razeeb, K. M. Ni nanowire supported 3D flower-like Pd nanostructures as an efficient electrocatalyst for electrooxidation of ethanol in alkaline media. *J. Power Sources* **218**, 148-156 (2012).
122. Arjona, N., Guerra-Balcázar, M., Cuevas-Muñiz, F. M., Álvarez-Contreras, L., Ledesma-García, J. & Arriaga, L. G. Electrochemical synthesis of flower-like Pd nanoparticles with high tolerance toward formic acid electrooxidation. *RSC Adv.* **3**, 15727-15733 (2013).
123. Shannon, R. D. Revised effective ionic radii and systematic studies of interatomic distances in halides and chalcogenides. *Acta Crystallogr. Sect. A* A32, 751 (1976).
124. Giacco, D., Marrani, A. G. & Brutti, S. Enhancement of the performance in Li-O_2 cells of a $NiCo_2O_4$ based porous positive electrode by Cr(III) doping. *Mater. Lett.* **224**,113-117 (2018).
125. Viswanathan, V., Nørskov, J. K., Speidel, A., Scheffler, R., Gowda, S. & Luntz, A. C. Li-O_2 kinetic overpotentials: Tafel plots from experiment and first-principles theory. *J. Phys. Chem. Lett.* **4**, 556-560 (2013).
126. Cui, Z. H., Guo, X. X. & Li, H. Equilibrium voltage and overpotential variation of nonaqueous Li-O_2 batteries using the galvanostatic intermittent titration technique. *Energy Environ. Sci.* **8**, 182-187 (2015).
127. Toussaint, C. J. A high-temperature X-ray diffraction study of the NiO-Li_2O system. *J. Appl. Crystallogr.* **4**, 293–297 (1971).
128. Beverskog, B. & Puigdomenech, I. Revised Pourbaix diagrams for nickel at 25-300 °C. *Corros. Sci.* **39**, 969-980 (1997).
129. Moore, R. J. & White, J. Equilibrium relationships in the system NiO-CoO-O_2. *J. Mater. Sci*. **9**, 1393-

1400 (1974).

130. Grosvenor, A. P., Biesinger, M. C., Smart, R. S. C. & McIntyre, N. S. New interpretations of XPS spectra of nickel metal and oxides. *Surf. Sci*. **600**, 1771-1779 (2006).

131. Biesinger, M. C., Payne, B. P., Lau, L. W. M., Gerson, A. & Smart, R. S. C. X-ray photoelectron spectroscopic chemical state Quantification of mixed nickel metal, oxide and hydroxide systems. *Surf. Interface Anal.* **41**, 324-332 (2009).

132. Kim, J.-G., Pugmire, D. L., Battaglia, D. & Langell, M. A. Analysis of the $NiCo_2O_4$ spinel surface with Auger and X-ray photoelectron spectroscopy. *Appl. Surf. Sci.***165**, 70-84 (2000).

133. Soriano, L., Preda, I., Gutiérrez, A., Palacín, S., Abbate, M. & Vollmer A. Surface effects in the Ni 2p X-ray photoemission spectra of NiO. *Phys. Rev. B - Condens. Matter Mater. Phys.* **75**, 233417 (2007).

134. Mossanek, R. J. O., Preda, I., Abbate, M., Rubio-Zuazo, J.,Castro, J. R.,Vollmer, A., Gutiérrez, A. & Soriano, L. Investigation of surface and non-local screening effects in the Ni 2p core level photoemission spectra of NiO. *Chem. Phys. Lett.* **501**, 437-501 (2011).

135. Biesinger, M. C., Payne, B. P., Grosvenor, A. P., Lau, L. W. M., Gerson, A. R. & Smart, R. S. C. Resolving surface chemical states in XPS analysis of first row transition metals, oxides and hydroxides: Cr, Mn, Fe, Co and Ni. *Appl. Surf. Sci.* **257**, 2717-2730 (2011).

136. Dupin, J.-C., Gonbeau, D., Vinatier, P. & Levasseur, A. Systematic XPS studies of metal oxides, hydroxides and peroxides. *Phys. Chem. Chem. Phys*. **2**, 1319-1324 (2000).

137. Uhlenbrock, S., Scharfschwerdt, C., Neumann, M., Illing, G. & Freund, H. J. The influence of defects on the Ni 2p and O 1s XPS of NiO. *J. Phys. Condens. Matter* **4**, 7973-7978(1992).

138. McKay, J. M. & Henrich, V. E. Surface electronic structure of NiO: Defect states, O_2 and H_2O interactions. *Phys. Rev. B* **32**, 6774 (1985).

139. Van Elp, J., Eskes, H., Kuiper, P. & Sawatzky, G. A. Electronic structure of Li-doped NiO. *Phys. Rev. B* **45**, 16-12 (1992).

140. Zhang, D., Gökce, B. & Barcikowski, S. Laser Synthesis and Processing of Colloids: Fundamentals and Applications. *Chem. Rev.* **5**, 3990-4103 (2017).

141. De Bonis, A., Santagata, A., Galasso, A., Laurita, A. & Teghil, R. Formation of Titanium Carbide (TiC) and TiC@C core-shell nanostructures by ultra-short laser ablation of titanium carbide and metallic titanium in liquid. *J. Colloid Interface Sci.***489**,76-84 (2017).

142. De Bonis, A., Sansone, M., Galasso, A., Santagata, A. & Teghil, R. The role of the solvent in the ultrashort laser ablation of palladium target in liquid. *Appl. Phys. A Mater. Sci. Process.* **117**, 211-216 (2014).

143. De Bonis, A., D'Orsi, R., Funicello, M., Lupattelli, P., Santagata, A., Teghil, R. & Chiummiento, L. First application of homogeneous Pd nanoparticles prepared by pulsed laser ablation in liquid to a Suzuki-type reaction. *Catal. Commun.* **100**,164-168 (2017).

144. Donohue, J. The structures of the elements. (1974).

145. Pikna, L., Milkovič, O., Saksl, K., Heželová, M., Smrčová, M., Puliš, P., Michalik, S. & Gamcová, J. The structure of nano-palladium deposited on carbon-based supports. *J. Solid State Chem.* **212**, 197-204 (2014).

146. Brun, M., Berthet, A. & Bertolini, J. XPS, AES and Auger parameter of Pd and PdO. *J. Electron Spectros. Relat. Phenomena* **104**, 55-60 (1999).

147. Kim, K. S., Gossmann, A. F. & Winograd, N. X-Ray Photoelectron Spectroscopic Studies of Palladium Oxides and the Palladium-Oxygen Electrode. *Anal. Chem*. **46**,197-200 (1974).